A STUDY OF STELLAR DEBRIS DYNAMICS DURING A TIDAL DISRUPTION EVENT

DISSERTATION

Aurora Clerici

Advisor: prof. dr. Andreja Gomboc

Nova Gorica, 2020

Študij dinamike zvezdne snovi med dogodkom plimskega raztrganja

DISERTACIJA

Aurora Clerici

UNIVERSITY OF NOVA GORICA
GRADUATE SCHOOL

Aurora Clerici, A study of stellar debris dynamics during a tidal disruption event, Dissertation, (2020)

Abstract

The number of observed tidal disruption events is increasing rapidly with the advent of new surveys. Thus, it is becoming increasingly important to improve TDE models using different stellar and orbital parameters.

We study the dynamical behaviour of tidal disruption events produced by a massive black hole like Sgr A* by changing different initial orbital parameters, taking into account the observed orbits of S stars. Investigating different types of orbits and penetration factors is important since their variations lead to different timescales of the tidal disruption event debris dynamics, making mechanisms such as self-crossing and pancaking act strongly or weakly, thus affecting the circularisation and accretion disk formation.

We have performed smoothed particle hydrodynamics simulations. Each simulation consists in modelling the star with 10^5 particles, and the density profile is described by a polytrope with $\gamma = 5/3$. The massive black hole is modelled with a generalised post-Newtonian potential, which takes into account relativistic effects of the Schwarzschild space-time.

Our analyses find that mass return rate distributions of solar-like stars and S-like stars with same eccentricity have similar durations, but S-like stars have higher mass return rate, as expected due to their larger mass. Regarding debris circularisation, we identify four types of evolution, related to the mechanisms and processes involved during circularisation: in type 1 the debris does not circularise efficiently, hence a disk is not formed or is formed after relatively long time; in type 2 the debris slowly circularises and eventually forms a disk with no debris falling back; in type 3 the debris relatively quickly circularises and forms a disk while there is still debris falling back; finally, in type 4 the debris quickly and efficiently circularises, mainly through self-crossings and shocks, and forms a disk with no debris falling back. Finally, we find that the standard relation of circularisation radius $r_{\mathrm{circ}} = 2r_{\mathrm{t}}$ holds only for $\beta = 1$ and eccentricities close to parabolic.

Povzetek

Število opaženih dogodkov plimskih raztrganj hitro narašča zahvaljujoč novim pregledom neba. Zato postaja vedno pomembneje, da izboljšamo modele dogodkov plimskih raztrganj in dobimo teoretične napovedi za različne zvezdne in orbitalne parametre.

V tej disertaciji smo proučevali dinamično obnašanje snovi ob plimskih raztrganjih zvezd v bližini masivne črne luknje, kakršna je Sgr A* v središču naše Galaksije, pri čemer smo spreminjali začetne orbitalne parametre in upoštevali opazovane orbite S zvezd. Proučevanje različnih vrst orbit in parametrov trka je pomembno, saj le-ti vplivajo na časovno skalo dinamike ostankov plimskih raztrganj, na jakost mehanizmov, kot sta samo-prečkanje in sploščitev, ter s tem na cirkularizacijo in nastanek akrecijskega diska.

Simulacije smo izvedli z metodo hidrodinamike zglajenih delcev. V simulacijah smo zvezdo modelirali z 10^5 delci in gostotnim profilom, kot ga opiše politropni model z $\gamma = 5/3$. Vpliv masivne črne luknje smo modelirali s posplošenim post-Newtonskim potencialom, ki upošteva relativistične efekte Schwarzschildovega prostor-časa.

Naše analize kažejo, da imajo porazdelitve hitrosti vračanja snovi za zvezde podobne Soncu in za zvezde podobne S-zvezdam pri enaki eksentričnosti podoben čas trajanja, vendar imajo S-zvezde višjo vrednost histrosti vračanja snovi, kot je pričakovano zaradi njihove večje mase. Glede cirkularizacije ostankov smo identificirali štiri tipe razvoja, ki so povezani z mehanizmi in procesi med cirkularizacijo: pri tipu 1 se ostanki zvezde ne cirkularizirajo učinkovito in posledično disk ne nastane ali pa nastane po relativno dolgem času; pri tipu 2 se ostanki zvezde cirkularizirajo počasi in sčasoma tvorijo disk, pri čemer ne ostane nič snovi, ki bi še padala proti disku; pri tipu 3 se ostanki zvezde relativno hitro cirkularizirajo in tvorijo disk, vendar ostane še nekaj snovi, ki pada na disk; pri tipu 4 pa se ostanki zvezde hitro in učinkovito cirkularizirajo, večinoma zaradi samo-prečkanja in udarnih valov, in tvorijo disk, pri čemer ne ostane nič snovi, ki bi padala proti disku. Ugotovili smo tudi, da standardna zveza, da je cirkularizacijski polmer enak dvakratniku plimskega polmera, $r_{circ} = 2r_t$, velja le za parameter trka $\beta = 1$ in eksentričnosti blizu parabolični.

Contents

Bibliography

Introduction

It is well established from both gas and stellar dynamical measurements that massive black holes (MBH) reside in the nuclei of most galaxies (e.g. Magorrian & Tremaine, 1999, and references therein). These extreme astrophysical objects have masses between $10^5 M_\odot$ and $10^{10} M_\odot$, and are embedded in dense stellar environments, as it can be observed from the nearest MBH we can study, i.e. Sgr A* in our Galactic center. While nearby MBHs can be studied dynamically, distant ones can only be observed if they are undergoing luminous accretion. This is the case for active galactic nuclei (AGN), which are providing the most valuable information about MBHs; however, they represent a small fraction of the MBH population. In order to have a more complete picture of the astrophysical properties of MBHs, it is necessary to probe also those that are in quiescent state.

A variety of dynamical processes are capable of feeding stars to MBHs, which can result in tidal disruption events (TDEs) which can temporarily turn on a dormant MBH. Among these feeding mechanisms, the two-body relaxation is the most understood. Calculations of TDE rates based on this mechanism in realistic galaxies find that they are rare events, with a rate of $\gtrsim 10^{-4}$ yr^{-1} per galaxy (Wang & Merritt, 2004; Stone & Metzger, 2016; Stone & van Velzen, 2016). In comparison, observational estimates for the TDE rate are typically $\sim 10^{-5}$ yr^{-1} per galaxy (Donley et al., 2002; Khabibullin & Sazonov, 2014), which is discrepant by an order of magnitude (or more) with theoretical estimates (Stone & Metzger, 2016). Other processes can in principle enhance the TDE rate above the order set by two-body relaxation, such as non-conservation of angular momentum in axisymmetric or triaxial potentials (Magorrian & Tremaine, 1999; Merritt & Poon, 2004), interactions with massive perturbers ($M_p > 10^2 M_\odot$) such as molecular clouds, globular stellar clusters, intermediate MBHs (Perets et al., 2007) and large-scale accretion disks (Karas & Šubr, 2007), or gravitational wave recoil of the central SMBH (Stone & Loeb, 2011). The impact of these more exotic mechanisms is more difficult to quantify observationally.

The general picture of a TDE (Lacy et al., 1982; Carter & Luminet, 1983; Rees, 1988; Phinney, 1989; Evans & Kochanek, 1989) considers a star approaching a MBH on a nearly parabolic orbit from large separation ($\sim$ pc). After the star gets squeezed and disrupted by the MBH, approximately half of the stellar debris loses orbital energy inside the tidal disruption radius and becomes gravitationally bound to the MBH. The bound debris falls back, circularizes due to self-crossings and collisional shocks between gas streams, and eventually accretes on to the MBH. The properties of this accretion disk have been investigated by many authors (e.g Cannizzo et al., 1990; Loeb & Ulmer, 1997; Strubbe & Quataert, 2009; Lodato & Rossi, 2011; Shen & Matzner, 2014). The power emitted during the accretion process is enough to generate a highly luminous event; several of these

events have been observed (Bade et al., 1996; Komossa & Bade, 1999; Halpern et al., 2004; Bloom et al., 2011; Cenko et al., 2012; Bogdanović et al., 2014; Komossa, 2015). The catalogue of TDE candidates is steadily growing as more of them are detected at optical, UV and soft X-ray wavelengths (e.g. Bade et al., 1996; Komossa & Greiner, 1999; Gezari et al., 2006), and thanks to high-cadence surveys, a larger fraction of these observed events have well-sampled lightcurves that include the early rise to peak (e.g. Gezari et al., 2012; Arcavi et al., 2014; Chornock et al., 2014; Blagorodnova et al., 2019). A few of them are thought to produce a relativistic jet launched from the inner region of the accretion flow, to which is attributed the observed hard X-ray emission (Bloom et al., 2011; Cenko et al., 2012; Brown et al., 2015a).

It was analytically shown (Rees, 1988; Phinney, 1989) that the rate at which debris returns to the MBH is $dm/dt \propto t^{-5/3}$. This feature is considered to be the observational signature of a TDE. Indeed, many of the observed TDE candidates show a lightcurve that follows this power-law. However, this feature is expected for the bolometric lightcurve and for the X-ray band, while the optical/UV bands is expected to follow a flatter dependence $\propto t^{-5/12}$ (Lodato & Rossi, 2011). Observationally, on one hand TDEs are found to follow the $t^{-5/3}$ feature in the first few months (e.g. Gezari et al., 2008), on the other hand there are TDEs which are best approximated by the $t^{-5/12}$ (Holoien et al., 2019), and lastly TDEs like ASASSN-14li and ASASSN-14ae are found to be best fitted with an exponential law e^{-t} (e.g. Holoien et al., 2014, 2016b).

The dynamics of stellar tidal disruption have been modelled by several authors, starting with simple analytical considerations (Rees, 1988; Phinney, 1989; Lodato et al., 2009; Kesden, 2012a), going to more complex dynamical models (e.g. Luminet & Marck, 1985; Kosovichev & Novikov, 1992; Ivanov & Novikov, 2001; Gomboc & Čadež, 2005), and hydrodynamical simulations (e.g. Nolthenius & Katz, 1982; Evans & Kochanek, 1989; Laguna et al., 1993; Kobayashi et al., 2004; Guillochon et al., 2009; Rosswog et al., 2009a; Antonini et al., 2011; Shiokawa et al., 2015; Bonnerot & Lu, 2019).

As the number of observed TDEs increases, it becomes more important to improve models of dm/dt for disruptions with different stellar and orbital parameters. Early smoothed particle hydrodynamics (SPH) calculations (Evans & Kochanek, 1989) supported the initial analytic estimates, showing that the distribution of specific energies, calculated not long after the time of disruption, produces a fallback rate $\propto t^{-5/3}$. Lodato et al. (2009) investigated the effects of the structure of the star during the disruption process, demonstrating that the early stages of the fallback depend on the properties of the star. Guillochon & Ramirez-Ruiz (2013) found that shallower impact parameters affects the nature of the event, often resulting in the survival of a bound stellar core (partial disruption). Hayasaki et al. (2013); Bonnerot et al. (2016); Hayasaki et al. (2016) and Shiokawa et al. (2015) studied stars on elliptical orbits and the effects of general relativity on the stream, showing how apsidal and Lense-Thirring precession can alter the formation of the disk which forms when the tidally-disrupted debris returns to pericenter.

The Galactic center (GC) is a unique laboratory to study physical processes and phenomena that may be occurring in many other galactic nuclei, where they are not observationally accessible. The general picture of the GC, in particular

that of the central parsecs, is rapidly changing (e.g. Yusef-Zadeh et al., 2000; Alexander, 2005; Yusef-Zadeh & Wardle, 2012). In order to understand the stellar environment in the inner parsecs, it is relevant to study the stars well outside the dynamical sphere of influence of Sgr A* and within the $\leq$ 100 pc scale. The Galactic bulge stellar population is composed of old stars ($\sim$ 10 Gyr), while the inner $\leq$ 100 pc stellar population seems to have been forming throughout the life of the Galaxy. In particular, the discovery of the so called "S stars" provided a new way to study Sgr A*, around which they are orbiting ($<$ 0.04 pc). However, their great proximity to the MBH was soon called the "paradox of youth" (Ghez et al., 2003). Those S stars which have been analysed are young, main sequence massive stars, and their existence was unexpected as it is not clear how they could form in such a violent environment. A current idea is that these stars have formed far away from the central region, to which they migrated through the Hills mechanism (Hills, 1988; Brown, 2015). In this scenario, we start with binary stars, which get scattered under certain dynamical conditions toward the MBH. Due to the interaction with the latter, one of the binary components gets ejected at high velocity (high velocity star), while the other gets on a bound orbit to the MBH. In these regards, there is an interesting mechanism outlined by Hamers & Perets (2017), which involves nuclear spiral arms in the enhancement of TDEs, S stars and high velocity stars' rates. On $\sim$ 100 pc scale, gas can be perturbed by torques from nuclear bars (e.g. Shlosman et al., 1989; Englmaier & Shlosman, 2004), which drive inflows to the nuclear regions, giving rise to nuclear spiral arms. These structures can perturb orbits of stars, making them an additional channel that can drive stars onto orbits which bring them very close to the MBH. As a consequence, strong interactions such as stellar TDEs and stellar binary TDEs can be triggered.

From TDE observations we can infer not only the mass and spin of the MBH responsible of disrupting the star (e.g. Leloudas et al., 2016; Gomez et al., 2020; Mummery & Balbus, 2020), but also the mass of the star being disrupted (Guillochon & Ramirez-Ruiz, 2013; Blagorodnova et al., 2017) and information related to its composition (e.g. Arcavi et al., 2014; Blagorodnova et al., 2019). To be noted that the estimate of these parameters depends on our current understanding of TDEs and the deriving models. Considering this, TDEs have the potential to be a tool to study not only quiescent MBHs, but also the innermost galactic environment surrounding the MBH itself. TDEs are already proving to be a useful source of information regarding the host galaxy. For example, Graur et al. (2018) suggest the possibility of the existence of a relation between the TDE rate, which depends on the properties of the stars near the MBH (which are on sub-pc scales and so rarely measurable), and global galaxy properties. Even though it is difficult to resolve galactic nuclei down to sub-pc scales, studies found, for example, that many galaxies harbour young stellar populations in the central few parsecs, like our Galaxy, M31 and nearby galaxies (e.g. Krabbe et al., 1991, 1995; Seth et al., 2006; Chang et al., 2007; Lockhart et al., 2018), and this discovery has implications on the nuclear environment and the role of the MBH (e.g. Ghez et al., 2003).

Our work proposes to test the feasibility of TDEs to be used as a (complementary) source of information of the stellar population residing in the innermost parts of a galactic nucleus. The idea is to investigate whether there are any char-

acteristic features in the dynamics of TDEs that depend on the particular type of stars and on their orbital parameters, that can reflect in the mass fallback rate and, in turn, possibly in the lightcurves.

To do this, we have performed SPH simulations. Each simulation consists in modelling the star with 10^5 particles, and the density profile is described by a polytrope with $\gamma = 5/3$. The MBH is modelled with a generalised post-Newtonian potential, which takes into account relativistic effects of the Schwarzschild space-time. We study the TDE dynamical behaviour produced by a MBH like Sgr A* by changing different orbital parameters and taking into account the observed orbits of S stars. In particular, we explore the evolution of the debris and of its fallback depending on different values of eccentricities and penetration factors, since this affects the timescale of the resulting lightcurves. We perform analyses on the evolution of specific energy over time for different values of eccentricities or penetration factors to obtain insight on the circularization processes responsible for disc formation. We also analyse the evolution of accreted matter and its energy, and the distribution of eccentricities and angular momentum as these also add more information about the circularization processes and disc formation.

In Chapter 1, we give an overview of the state of the art in the TDE field. In Chapter 2, we describe the TDE theory, going through the characteristic stages, i.e. scattering into the loss cone, first passage to pericenter, debris stream evolution and fallback, circularization and disc formation. In Chapter 3, we give an overview of the SPH code used for this work and a description of the simulation setup. In Chapter 4, we discuss results, and finally we give our Conclusions.

CHAPTER 1

Overview

1.1 Massive black holes

In the year 1783, a paper for the *Philosophical Transactions of the Royal Society of London* presented the idea that there could exist objects called dark stars in the universe. Its author, the natural philosopher John Michell, started his reasoning in the context of Newton's corpuscular theory of light, which states that light consists of particles with finite velocity. It was noted that the escape velocity from the surface of a body of mass M and radius R exceeds the velocity c, if $R < R_{crit}$, where

$$R_{crit} = \frac{2GM}{c^2} \tag{1.1}$$

The particles emanated from a star would be slowed down by the stellar gravitational pull. According to Michell's calculations, a star with more than 500 times the Sun's size would have a gravitational pull strong enough to not let light particles escape. It was the first conceptualization of a black hole (BH). In 1799, also Jean-Pierre Laplace forms his own idea of a BH (Montgomery et al., 2009).

In 1915 Albert Einstein developed the theory of general relativity (Einstein, 1915c,d,e,a,b), which was published in 1916 (Einstein, 1916). In the same year, Karl Schwarzschild provided the first exact solution to the Einstein field equations, for the case of a single spherical non-rotating mass (Schwarzschild, 1916, 1999). This solution becomes singular at the Schwarzschild radius, however the physical nature of this surface was not quite understood at the time. Later in 1931, Subrahmanyan Chandrasekhar used special relativity to find that a non-rotating body of electron-degenerate matter has no stable solutions above some limiting mass (Chandrasekhar, 1931), which is now known as the Chandrasekhar limit at 1.4 $M_\odot$, and it would collapse. In 1939, Robert Oppenheimer and collegues predicted that neutron stars above the Tolman-Oppenheimer-Volkoff limit would collapse further, and no law of physics could stop it (Oppenheimer & Volkoff, 1939; Tolman, 1939). In 1958, David Finkelstein was the first to figure out that Schwarzschilds solution had an event horizon separating the interior from the exterior region of a BH (Finkelstein, 1958). It was only some years later, in 1963, when Roy Kerr found the exact solution for a rotating black hole (Kerr, 1963), and two years later the no-hair theorem came to light, stating that a stationary black hole solution can be completely described by just three parameters, i.e. mass, angular momentum and electric charge (Misner et al., 1973).

However, the astrophysical existence of a BH was still not taken very seriously, as people were inclined to believe that there was still some unknown mechanism which could prevent the complete collapse of a massive body. In 1964, Yakov Zeldovich and Edwin Salpeter proposed that the quasar 3C273 (Schmidt, 1963) and others could be explained by matter falling onto a massive compact object, with an estimated mass of $10^8 M_\odot$ (Salpeter, 1964; Zel'dovich, 1964). In the 1970s, the first clear association of X-ray astronomy and BHs was made by Giacconi and colleagues on Cygnus X-1 (Bowyer et al., 1965; Tananbaum et al., 1972). It was soon identified as a BH candidate by Thomas Bolton, Louise Webster and Paul Murdin (Bolton, 1972; Webster & Murdin, 1972). In the same years, more phenomena appeared to require the presence of a very massive object at the center of galaxies. For example, Arthur M. Wolfe and Geoffrey Burbidge invoked a massive object to explain the large velocity dispersion of stars in the nuclear region of elliptical galaxies (Wolfe & Burbidge, 1970). In 1978, a dynamical evidence for a massive dark object was found in the nucleus of Messier 87 (Sargent et al., 1978).

Now BHs present a big challenge to the current foundations of physics, being at the heart of fundamental questions unifying general relativity with quantum physics (Hawking, 1976; Giddings, 2017). We are also in a new era of astronomy where gravitational wave observations, for example the recent LIGO detections (Abbott et al., 2016, 2017), and very long baseline interferometry, can provide important hints about new principles of physics from BHs.

From the theory of general relativity, there are virtually no constraints on the mass of a BH. They can be arbitrarily small or large. However, from observations it is known that BHs have a (wide) range of masses, which can be roughly divided into stellar-mass BHs and massive BHs.

Stars which cannot maintain anymore their thermal pressure generated by burning their nuclear fuel can collapse into a BH, provided the original star had enough mass (Fig. 1.1). If the mass of the remnant exceeds $\sim 3 - 4 M_\odot$, the pressure of degernate neutrons is insufficient to stop the collapse, and the object will inevitably collapse and form a stellar-mass BH (Shapiro et al., 1985; Camenzind, 2007). Evidence for stellar-mass BHs come from X-ray observations (Webster & Murdin, 1972; Remillard & McClintock, 2006) and from the more recent gravitational wave measurements.

BHs with masses from 10^6 to 10^9 solar masses were speculated to exist in the centers of nearly all galaxies (Lynden-Bell, 1969; Kormendy & Richstone, 1995; Miyoshi et al., 1995), the Galactic Center (GC) included (Eckart & Genzel, 1997; Ghez et al., 1998). Now it is well established from both gas and stellar dynamical measurements that massive black holes (MBH) do reside in the nuclei of most galaxies (e.g. Young et al., 1978; Kormendy & Richstone, 1995; Ferrarese & Ford, 2005, and references therein). How do these massive objects form is still an open research field, with different proposed mechanisms.

There are also claims about the existence of intermediate MBHs - those with mass range $10^2 - 10^5 M_\odot$. Intermediate MBHs are yet an elusive class, theorized to be potential seeds of super MBHs and to reside in globular clusters, but no observation has confirmed their presence up to date. Recently there have been speculations about a new class of MBHs dubbed ultra MBHs (Mezcua et al., 2018), which should have $M_{BH} > 10^{10} M_\odot$. In order to keep the discussion general,
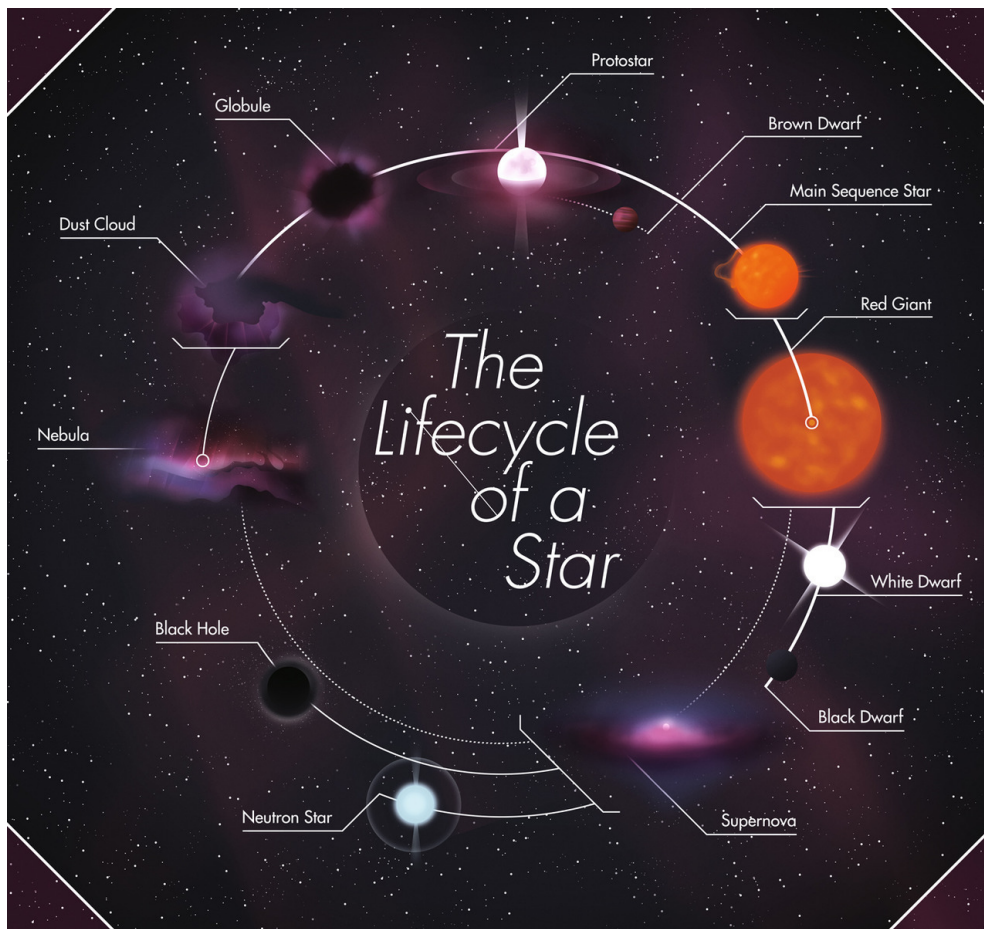
Figure 1.1: Formation of a BH. A BH is the result of the lifecycle of a massive star. The cycle starts from the nebula and goes clockwise. Image: Jack Hughes /Twitter: @jackmrhughes
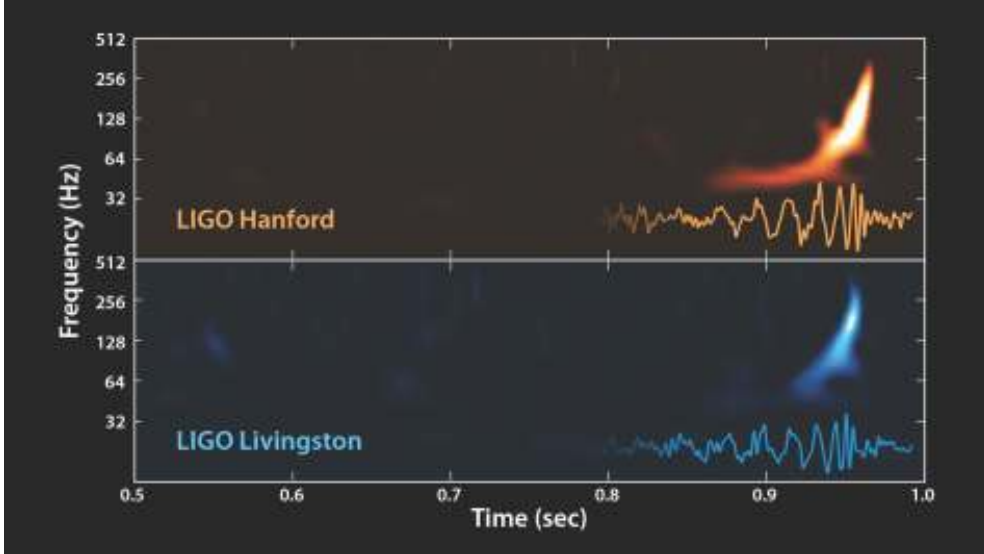
Figure 1.2: Gravitational wave signal of BH formation resulting from the merger of a BH binary. The signal was detected in 2015 by LIGO (Abbott et al., 2016, 2017). Image: ©LIGO.

in this thesis we choose to refer to black holes with masses larger than $\sim 10^5 M_\odot$ up to $10^{10} M_\odot$ (McConnell et al., 2011; Mehrgan et al., 2019) simply as MBHs.

According to general relativity, any information related to the BH matter stays inside its event horizon, making it not accessible to external observers (the "no hair" theorem, Misner et al., 1973). The electrical charge is usually neglected (Zajacek & Tursunov, 2019) and implicitly set to zero. This is a good approximation when dealing with neutral particles and photons, while care must be taken when dealing with charged particles, such as cosmic rays, as even a small charge is significantly sufficient in affecting their motion. Electromagnetic and multimessenger experiments focus at determining mainly the BHs mass, and spin, assuming that the charge is negligible, also often backed up by the assumption that the presence of plasmas around astrophysical BHs leads to prompt discharging. In order to detect MBHs and infer properties such as their mass, there are different methods, which can be direct and indirect. In general, they can be observed through luminous accretion of gas or via gravitational interactions with the surrounding stellar environment. In the following, we illustrate few of these methods in order to give a general idea of how MBHs are studied.

Most galaxies host within their bulge a MBH and various correlations have been observed between the MBH itself and the properties of the galactic bulge hosting it. The first correlation called Magorrian relation (Magorrian et al., 1998) relates the mass of the MBH to the mass of the galactic bulge M_{bulge} as $M_{BH} \sim 0.001 M_{bulge}$. Ferrarese & Merritt (2000) and Gebhardt et al. (2000a) discovered the scaling relation between the mass of the MBH and the velocity dispersion of the stellar population of the spheroid bulge of galaxies, written as $M_{BH} - \sigma_*$ (Fig. 1.3). This relation has been confirmed several times in the following years (Gebhardt et al., 2000b; Merritt & Ferrarese, 2001; Tremaine et al., 2002; Ferrarese & Ford, 2005; Graham, 2008; Hu, 2008) and demonstrated that there is a high likelihood of a co-evolution between the MBH and its host

galaxy, and interest followed in studying more relations between the MBH and the galaxy properties. The strong correlation found between the MBH mass and the velocity dispersion of the galactic bulge suggests a mechanical feedback between the MBH and the host galaxy, which extends beyond the sphere of gravitational influence and the merging/accretion history of the MBH. However, this relation is observationally constrained and is not well calibrated for low-mass galaxies, since the galactic samples suffer from luminosity bias and large uncertainties.

Other relations between the MBH and the host galaxy include a correlation between the mass of the MBH and the light profile of the galactic bulge quantified by the galactic Sérsic index (Sérsic, 1963; Graham et al., 2001, e.g.): the Sérsic index n appears in the Sérsic model $R^{1/n}$, which is most commonly expressed as a parametrization of the galactic intensity as a function of the projected galactic radius R (Graham & Driver, 2005). Another correlation discovered by Seigar et al. (2008) involves the mass of the MBH and the tightness of the spiral arms in disc galaxies.

The origin and nature of the link between the MBH mass and the host galaxy properties are not yet clear. Thus, it is important to obtain an unbiased knowledge of the BHs demographics in galactic centers as a function of cosmic time. The issue is the detection of MBHs in quiescent galaxies via direct methods, such as stellar and gas dynamics, as they are limited by the current ability to resolve spatially the sphere of influence of the MBH. This is why direct mass measurement of MBHs are restricted to nearby galaxies and active galaxies. Regarding this issue, tidal disruption events are an additional tool to study MBH because they temporarily turn on a quiescent state MBH.

Another interesting method to measure mass of a MBH in an AGN involves using reverberation mapping. In particular, this technique is used to study the structure and kinematics of the broad emission-line region by observing the response of the broad emission lines to changes in the continuum. The mass of the MBH is then measured directly considering that the motion of gas is induced by the MBH gravitational force. However, also this technique presents restrictions in that it requires multi epoch observations in order to measure the spectral time lag.

A different approach relies on the established relation between the X-ray emission, the radio emission and the mass of the MBH, which form the so-called fundamental plane of BH activity (Merloni et al., 2003; Plotkin et al., 2012). This relation, which is shown in Fig. 1.4 originates from the following considerations. When studying BH-powered activity, there are some distinctive signatures which are usually regarded as a proxy of the BH existence: relativistic jets emitting synchrotron radiation in the radio band are one such signature, the second being the presence of a strong, compact power-law X-ray emission, which is usually associated with the inner part of an accretion flow (aside stellar-mass objects, in which case these signature are common also for neutron stars, and dynamical studies are needed to provide distinction between a neutron star and a BH). An increasing number of studies suggest that accretion physics scales globally across the entire BH mass scale, from stellar-mass BH to MBHs. The discovery of the fundamental plane of BH activity for low-accretion rate BHs supports this unification: once normalised by the BH mass, the process that regulates the fraction of energy accreted onto a BH, which is eventually converted into radiation, could
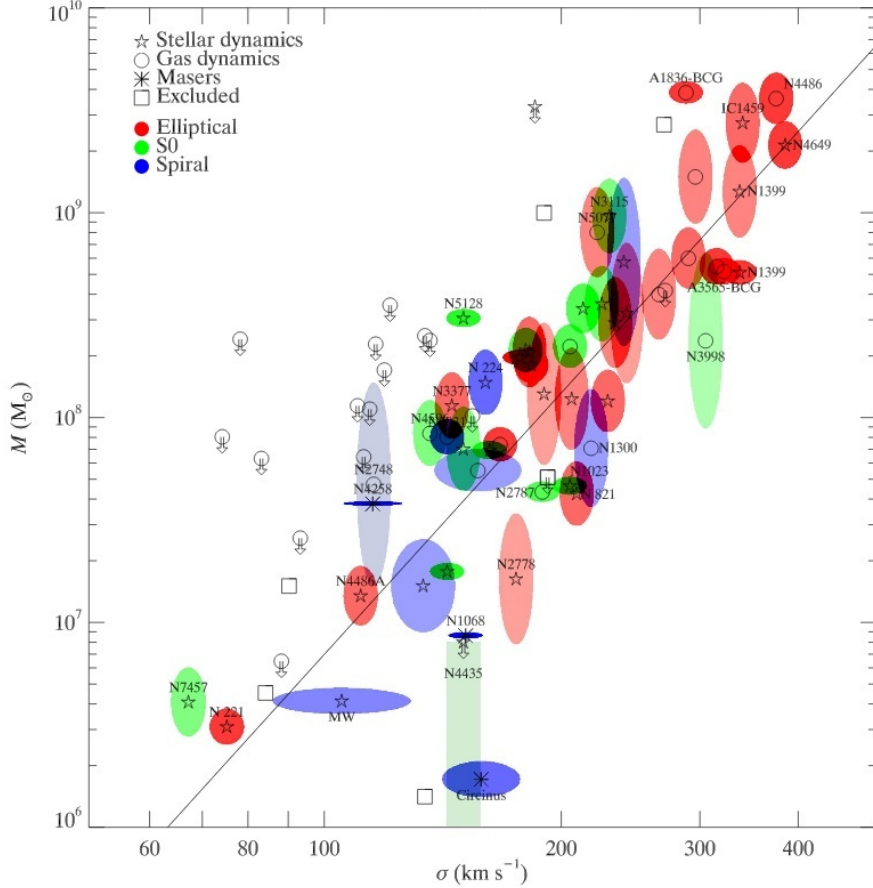
Figure 1.3: The $M - \sigma_*$ relation for galaxies with dynamical measurements. Symbols denote the method used to measure mass of the BH. Arrows denote the 3σ upper limits. For clarity only error boxes for upper limits close to or below the best-fit relation are shown. Colors denote the type of galaxy. Squares are galaxies not included in the fit. From Gültekin et al. (2009).

be universal for weakly accreting BHs. Fig. 1.4 shows the fundamental plane of BH activity for stellar-mass BHs (GBH, i.e. galactic BH in the figure), L+T objects, where L stands for LINER (low-ionisation nuclear emission-line regions) and T stands for Transition object (LINER/H II), Seyfert galaxies (a group of active galaxies), and quasars.

This short review of methods tells us that to study MBHs at large distances the only efficient approach to measure mass is through luminous accretion flows, which are present only for a small fraction of the entire MBH population. This introduces also a potential bias into mass measurements, which becomes more sever for spin measurements. While the existence of MBHs in active galactic nuclei has been demonstrated, a similar confirmation of dormant or quiescent state MBHs in distant non-active galaxies is difficult to obtain. But in order to have a complete picture of the astrophysical properties of MBHs, it is of interest to probe also those that are in quiescent state. For very nearby galaxies, for which telescopes can resolve the MBH sphere of influence, the stellar motion around the MBH can be studied and used to measure the mass. For distant galaxies, stellar disruptions which occur when the tidal forces of the MBH shred a star passing too close to it, can be used as probes to determine the MBH mass. The stellar debris
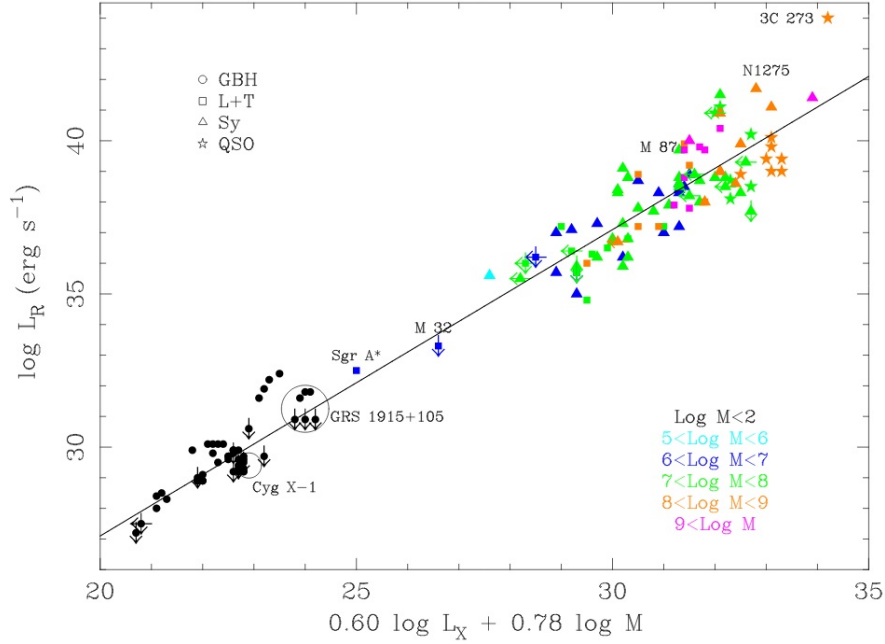
Figure 1.4: Fundamental plane of BH activity. Symbols denote the type of object, where GBH stands for galactic BHs, that is stellar-mass BHs, L+T stand for LINER and Transition object (LINER/H II), Sy stands for Seyfert galaxies and QSO stands for quasar. Colors denote the magnitude of the object. From Merloni et al. (2003).

will temporarily ($\sim$ months to years) fuel the otherwise quiescent MBH. These events were theorized in the 1970s-1980s and are referred to as tidal disruption events (TDE) (e.g. Hills, 1975; Frank, 1978, 1979; Carter & Luminet, 1982; Lacy et al., 1982; Luminet & Marck, 1985; Rees, 1988). Although also AGN can host tidal disruption events, the most unambiguous cases for a stellar disruption come from host galaxies with no or faint permanent activity.

1.2   The importance of massive black holes

The most important motivation to study MBHs is that they offer a unique laboratory to probe general relativity. For example, observations of Sgr A*, the MBH in the center of our Galaxy and nearest MBH we can observe, have provided some of the first most important evidence for the existence of event horizons (Broderick et al., 2009), before the recent direct imaging of the disc surrounding the MBH in M87 with the Event Horizon Telescope (Doeleman et al., 2009; Event Horizon Telescope Collaboration et al., 2019).

It is evident, but yet not fully understood, the fact that MBHs play also an important role in the growth and evolution of galaxies. MBHs and their bulges also formed at about the same epoch with respect to the age of the Universe. These observations suggest that BH formation and bulges formation are closely related.

In more detail, it is seen that MBH with masses of the order $10^9 M_\odot$ are observed up to redshifts $z \simeq 7.5$, when the Universe was only about 0.7 Gyr old (Yang et al., 2020). However no mechanism is known, which could create

and grow such a MBH in a relatively short lapse of time (e.g. Volonteri & Rees, 2005; Lodato & Natarajan, 2006, 2007; Volonteri et al., 2008; Volonteri, 2010b,a; Volonteri & Bellovary, 2012; Latif & Ferrara, 2016). It is unclear what role the environment plays in the existence of such objects at early times, nor it is yet understood which is the role of the first primordial stellar population (population III; e.g. Latif & Ferrara (2016) and references therein). There is an ongoing debate on whether the origin of MBH should be associated to BH seeds of stellar origin, that is BH with masses $\sim 1 - 10^2 M_\odot$ or to heavier BH seeds, that is BH with masses $\sim 10^4 - 10^6 M_\odot$ (Volonteri & Natarajan, 2009; Volonteri, 2010b). MBHs with masses of $\sim 10^5 M_\odot$ are thought to be found in Seyfert galaxies, for example POX 52 and NGC 4395 (Barth et al., 2004; Woo et al., 2019). Even lower mass BHs are expected to exist in dwarf galaxies, and, if the existence will be proved, they could give further insight in the process that formed the seeds of MBH detected in larger galaxies (Greene et al., 2019, and references therein).

The remnants of quasar phases at early times are possibly the MBHs found at the centers of galaxies in the local Universe. As discussed in the previous Section, the properties of these MBHs are tightly related to the mass and velocity dispersion of the host galaxies. In addition, the BH mass is correlated with the concentration or Sérsic index (Graham & Driver, 2007). All this observational evidences, which span from local galaxies to high-redshift quasars, suggest that there is a close connection between the formation and evolution of galaxies and their MBHs, which is yet to be fully understood (see Sesana, 2012, for a review).

Pulling together all the strings, we get a picture in which quiescent MBHs that populate galaxies in the present are relics of past luminous quasars. The MBHs we see are expected to be the final product of a complex evolutionary path, where black holes seeds in protogalaxies at high redshifts grow via MBH-MBH mergers and accretion episodes (Kauffmann & Haehnelt, 2000; Volonteri et al., 2003; Hopkins et al., 2006). In addition, a better understanding of the relation between the MBH and its host galaxy may also help in other aspects of astrophysics: demographics and growth history of MBHs could tell something more about black hole accretion and star formation.

BHs more massive than stellar-mass BHs are expected to be widespread in stellar systems, however only a small fraction of these BHs are active at levels of an AGN. In fact, most MBHs are in a quiescent state at the present. Nevertheless, since these objects are not completely isolated, but instead are embedded in stellar environments, they are unlikely to become fully inactive. Possible accreting sources can be material stripped by stars or stellar winds coming from mass loss of evolved stars. Indeed, the luminosity of Sgr A* could be explained by inefficient accretion of gas from stellar winds (Quataert, 2004), which can be also a significant fuel source in elliptical galaxies.

1.2.1   Sgr A*

The nearest observable MBH is Sgr A*, with mass $M_{BH} \simeq 4.3 \cdot 10^6 M_\odot$ and distance $R_0 \simeq 8.3$ kpc (1 pc $\simeq 3.26$ ly) from the Solar system (Gillessen et al., 2009). Its existence was first proposed its existence in 1971 by Lynden-Bell & Rees (1971). The first radio signal coming from the GC, which was later called
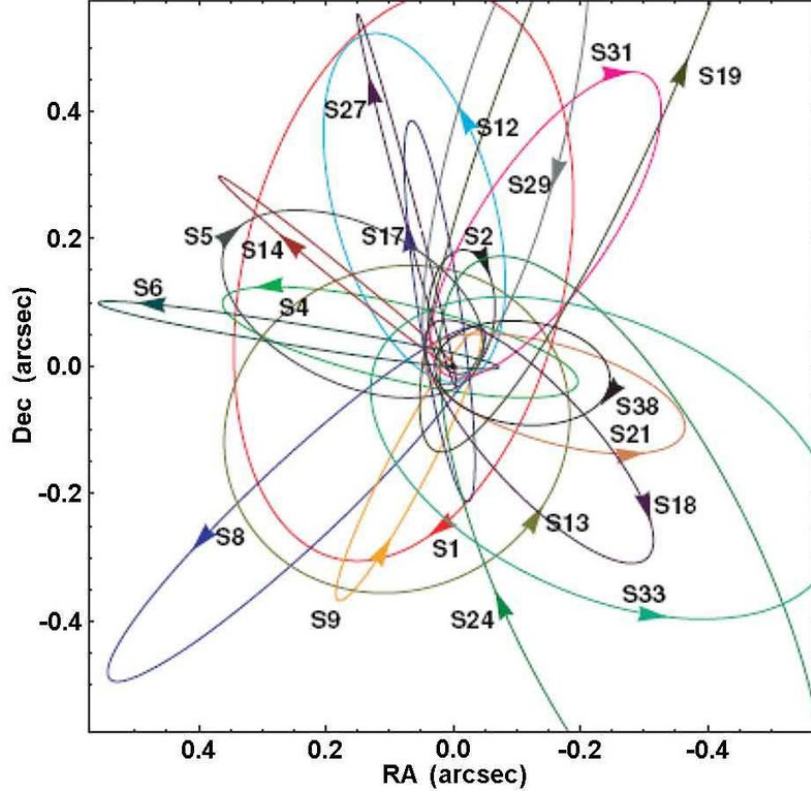
Figure 1.5: Orbits of individual stars near the Galactic center. Results from the Ghez group using the Keck telescope and from the Genzel group using the Europen Very Large Telescope (VLT) are combined. From Kormendy & Ho (2013).

Sagittarius A, was discovered by Karl Jansky in the '30s (Jansky, 1933). Observations in the following decades found that Sagittarius A consists of several components (Becklin & Neugebauer, 1968; Balick & Brown, 1974; Lacy, 1980; Ekers et al., 1983). One of those was brighter and very compact, and was discovered by Balick & Brown (1974). Later in 1982, Brown named this source Sgr A* (Brown, 1982).

A firm evidence for the existence of a MBH coincident with the radio source Sgr A* came in '90s (Genzel et al., 1997; Ghez et al., 1998). The tracking of the motions of these stars (since 1992) in the immediate vicinity of Sgr A* (Eckart & Genzel, 1996; Ghez et al., 1998; Gillessen et al., 2009), allowed the detection of accelerations and the determination of stellar orbits (Fig. 1.5), giving an observational evidence of a MBH in the GC.

Given its under luminosity, Sgr A* was not the first MBH to be detected (Baganoff et al., 2003), but despite the strong dust extinction along the line of sight through the Galactic disc (Schödel et al., 2007), it is the most accessible to high resolution observations. In the last decades, observations in the infrared and X-ray bands allowed us to detect the faint accretion emitted from Sgr A*, as well as to accurately track stars and gas clumps orbiting around it (Genzel et al., 2010).

The GC offers the unique opportunity to detect phenomena, which cannot
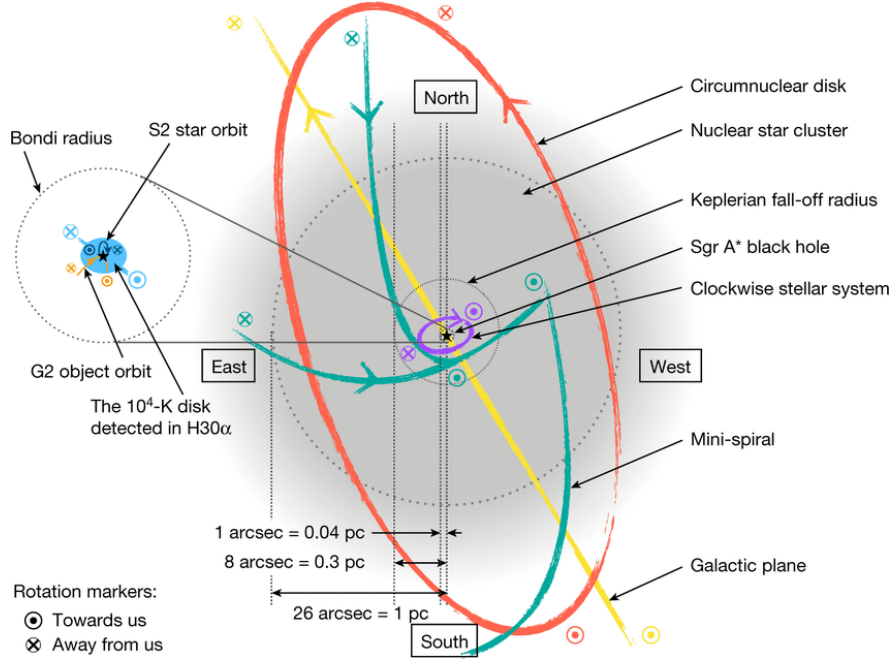
Figure 1.6: The inner two parsecs of the Galactic Centre region schematic plot, to scale. The main structures are indicated by different colours. The black star represents the Galactic Centre black hole Sagittarius A*. The red oval is the molecular ring or circumnuclear disk (torus), containing molecular gas. The structure in cyan is the mini-spiral, consisting of three streams of ionized gas rotating counterclockwise, orbiting the black hole and/or inflowing. The grey circle represents the nuclear star cluster. The yellow line marks the galactic plane (viewed edge-on). The dark-blue oval is the orbit of star S2 as projected on the sky and the orange line is the observed track of the G2 object as projected on the sky. The light-blue oval in the centre around Sgr A* is the ionized gas disk detected in the H30α line. The direction of rotation of the structures, where relevant, are shown with arrows, the circled cross indicates recession from Earth, and the circled dot indicates approach to Earth. The colours of the rotation markers match the colours of the rotating structures. The projected distances in parsecs were calculated for a distance to the Galactic Centre $D_{SgrA*} = 8.0$ kpc. At this distance 1 arcsec corresponds to 0.04 pc. From Murchikova et al. (2019).

currently be observed in more distant nuclei, considering its proximity (distance to GC is $\sim$ 100 times closer than the MBH in Andromeda, the nearest large galaxy, and $\sim$ 2000 times closer than galaxies in Virgo, the nearest cluster of galaxies; Alexander (2005)). High resolution observations of the GC get a lot more detailed and specific information than it is possible for any other galactic nucleus. As such, the GC allows us to study not only the MBH, but also to explore the impact of the MBH on its stellar and interstellar surrounding environment. It must be noted, however, that due to the nucleus being highly obscured by interstellar dust along the Galactic disc plane, observations in the optical band are not possible (Rieke et al., 1989; Alexander, 2005). Observations can be done in the infrared and microwave bands or X-rays and γ-rays.

The young stars paradox

Due to large interstellar extinction, the GC was not well studied until the 1990s, but now we know that the environment in the GC is varied. As other galactic nuclei, also the GC presents a rich molecular gas region, the so-called circumnuclear disc or ring (Fig. 1.6; Christopher et al. (2005)), orbiting around Sgr A*and extending $\sim 2 - 7$ pc. Observations in the innermost regions nearby Sgr A* show that it is surrounded by a parsec-scale star cluster, which consists of different components: an old spheroidal stellar population (Genzel et al., 2003), a population of early type stars of unknown origins (possibly confined within two discs; Paumard et al. (2006); Lu et al. (2009)), several dozen Wolf-Rayet stars (extremely hot, white stars with a high mass loss rate; Abbott & Conti (1987); Najarro et al. (1997)), a cluster of few luminous blue supergiants (Genzel et al., 2003), and a complex of ionized gas clouds called Sgr A West (Yusef-Zadeh et al., 1998). The study of these components can help in better understanding of star formation and accretion processes in this kind of extreme environments. In more detail, within the 0.04 inner parsecs, there are blue stars knowns as S-stars, orbiting in the immediate vicinity of Sgr A*, while between 0.04 and 0.4 pc there are few tens of OB supergiants, giants, and main-sequence stars mixed in faint red stars (Krabbe et al., 1995; Oh et al., 2009).

The discovery of the existence of a population of young stars (Krabbe et al., 1991, 1995), that is with ages < 6 Myr, which are bright enough to be tracked around the GC and reside in the hostile tidal environment close to Sgr A*, raised questions on star formation and stellar dynamics theories (Genzel et al., 2003; Ghez et al., 2003). There is no unique explanation to how these stars can exist so close to the MBH, which poses the so-called "young stars paradox", a problem that constitutes one of the major issues in GC research field. It has been proposed that a star cluster could have formed in a region far outside the central parsec, which then migrated inwards, or in situ star formation occurred, where a model requires a gravitationally unstable gaseous disc around the MBH for the young stars to form (Nayakshin et al., 2007).

The gaseous material which formed the young stars most probably came from farther regions. According to a well studied scenario, the circumnuclear gas may form from the tidal disruption of giant molecular clouds and could create the circumnuclear disc and the young stellar disc (Wardle & Yusef-Zadeh, 2008; Trani et al., 2018). It is also worth noting that there is evidence of ongoing (episodic) star formation in the GC (Yusef-Zadeh et al., 2008) and in the circumnuclear

Figure 1.7: Illustration showing a stream of stellar material as it is being devoured by a MBH in a tidal disruption flare. Image credit: NASA/JPL-Caltech.

disc itself. Similar episodes of star formation in the innermost central parsecs are expected in other nearby galaxies, and could be detected with the advent of 30-meter telescopes (Gullieuszik et al., 2014). Furthermore, young luminous stars such as the ones observed in the GC are good candidates for kinematic measurements to determine the mass of the MBH. These facts highlight even more the importance to study the stellar populations and environments surrounding MBH residing at the center of galaxies, and the reason we decided to focus on this kind of environment for this thesis.

1.3 Observations of tidal disruption events

A TDE occurs when a star approaches a MBH close enough to be disrupted by its tidal forces (Fig. 1.7). Part of the disrupted star then forms an accretion disc around the MBH. TDEs produce large amplitude flares, which last from months to years and occur at the center of a galaxy. In the following, we will resume the status of observations of TDEs (see also a review by Komossa, 2015). An exhaustive list of detected TDEs up to date can be found online[1] or in Auchettl et al. (2017).

It is not fully clear what observational features define a TDE as opposed to an AGN or a supernova (SN), for example. Most TDEs do not have multiwavelength coverage (see Table 1.1). For example, many TDE candidates are observed in X-rays, as expected, while others are detected in the optical/UV but show no sign of X-ray emission. Also, it is not clear if all the objects dubbed as TDE candidates do belong to the same class. For this reasons and for convenience of describing a general status of observations of TDEs, we are going to resume the observed TDEs according to their emission:

- TDEs with emission in the X-ray band;

---

[1]https://tde.space

Table 1.1: Simple representation of TDE status of observations. From I. Arcavi, TDE school in Jerusalem, 2015.

TDE	Swift J1644, Swift J2058	PS1-10jh, PTF09ge, PTF09axc, PTF09djl, ASASSN-14ae, ASASSN-15oi	ASASSN-14li
X-rays	×		×
Optical/UV		×	×
Radio	×		×

- TDEs with emission in the optical and UV bands;

- TDEs with luminous and energetic emission in the hard X-ray and γ-ray bands, along with radio emission.

The early TDE discoveries were made in the 1990s by the *ROSAT* satellite, which was well suited to detect such events with its high sensitivity, long lifetime, all-sky coverage in the first year of operation and soft X-ray response (0.1-2.4 keV). The first TDEs were discovered during the *ROSAT* X-ray all-sky survey (Bade et al., 1996; Komossa & Bade, 1999; Komossa & Greiner, 1999; Brandt et al., 1995; Grupe et al., 1995). Their X-ray lightcurves are plotted in Fig. 1.8 and they follow a $t^{-5/3}$ power law. The best covered events in terms of X-ray lightcurves, spanning more than a decade are NGC 5905 and RXJ1242-1119, which also show decline amplitudes larger than a factor 1000.

Later TDEs were observed in X-rays also by *XMM-Newton*, *Chandra* and *Swift* satellites. The *XMM-Newton* survey data has been compared to the *ROSAT* database and few events have been found (Esquej et al., 2007, 2008; Saxton et al., 2012, 2014). Instead of a normal galaxy, that is nn-active galaxy, some TDEs were also identified in clusters of galaxies. One of these was found in the field of the moderately rich cluster Abell 1795, at redshift $z = 0.062476$ (Donato et al., 2014), with an estimated MBH mass $< 10^6 M_\odot$. Other TDEs discovered by *XMM-Newton* and *ROSAT* occurred in relatively nearby galaxies at redshifts $z = 0.03 - 0.2$, which are optically quiescent. Finally, the *Swift* satellite gave an important contribution by providing rapid follow-ups, thus confirming fading X-rays and providing tight constraints on the luminosity evolution.

These events have mostly lightcurves with peak luminosity up to $\sim 10^{44}$ erg s^{-1}, which is followed by a temporal decay $\propto t^{-5/3}$. They have an effective temperature $T \approx 10^5$ K, which is slowly increasing with time. Their total energy is typically less than few 10^{51} erg.

TDEs were also observed in the optical and UV bands. TDEs were detected first by the GALEX satellite (Gezari et al., 2006, 2008, 2009), and later by surveys like *SDSS*, PTF, Pan-STARRS and ASAS-SN (Komossa et al., 2008; van Velzen et al., 2011; Gezari et al., 2012; Arcavi et al., 2014; Chornock et al., 2014; Holoien et al., 2016b,a; Leloudas et al., 2016). Starting from GALEX, which performed the first sky survey in the UV from space, three TDEs were detected. Data from SDSS together with spectroscopic followup found seven events, which show extreme coronal line emitters (ECLEs) (Komossa et al., 2009; Wang et al.,
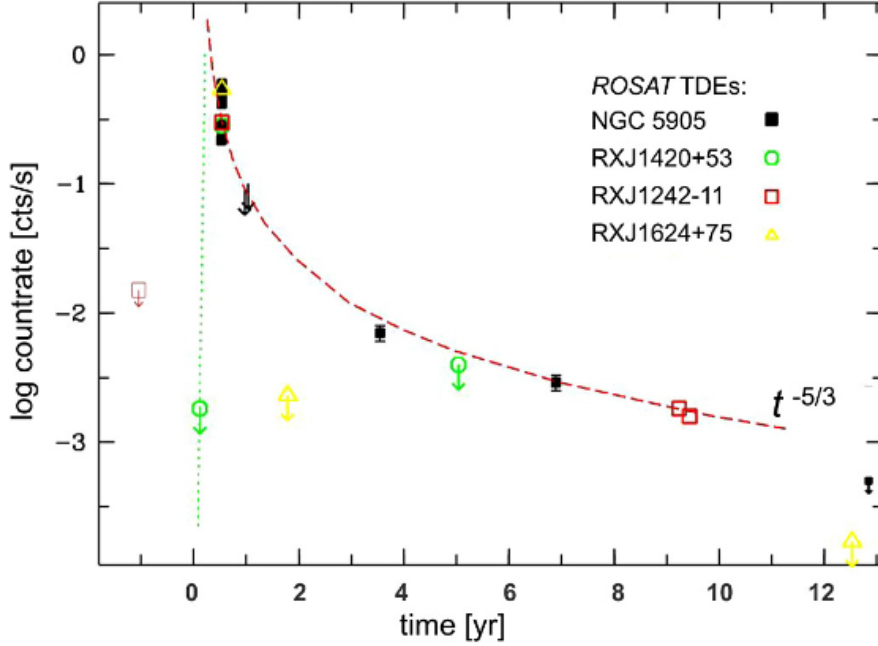
Figure 1.8: Joint X-ray lightcurve of TDEs detected by *ROSAT* (given by different symbols and colours), shifted to the same peak time. The decline is consistent with a $t^{-5/3}$ power law, given by the dashed line. From Komossa (2015).

2011, 2012; Palaversa et al., 2016). The class of ECLE is interesting because they exhibit distinct features, in particular strong coronal lines such as [FeX] λ 6376, [FeIX] λ 7894, [FeXIV] λ 5304, which require a high energy photoionizing continuum, and strong variability of their intensities over time. TDE powered flares are interpreted as the source of the high photoionizing continuum, which powers the Fe-lines. One of these events is ECLE SDSSJ095209.56+214313.3, which is characterized by a strong, fading, high ionization lines, and was long under discussion on whether it is a TDE or a SNe before finally setting down on the TDE origin. In fact, ruling out between these two astrophysical types is quite often the case when looking for TDEs. Time domain optical astronomy gives the possible advantage to have a large and high cadence TDE sample, but optical TDE flares can be more easily confused with nuclear Type II SNe, which are intrinsically more common.

A special TDE observed in the optical/UV is PS1-10jh. It was observed in 2010 by Pan-STARRS and GALEX (Gezari et al., 2012). Fig. 1.9 shows its lightcurve in the optical/UV (g, r, i, z bands from Pan-STARRS, near-UV from GALEX), and one point in the UV as measured by *Hubble Space Telescope*. The data is fitted with models by Lodato et al. (2009) and Guillochon & Ramirez-Ruiz (2013) and is consistent with a continued decline close to the canonical $t^{-5/3}$ power law. PS1-10jh is important because it is the first event whose lightcurve follows the rise to peak brightness and not just the later-time decline; it is the second optically-selected event to be followed up in real time after PTF10iya; it is the first event whose optical spectrum shows lines at all and, in particular, its spectrum shows He II emission lines but no hydrogen, which suggests that the event was the disruption of the core of a red giant star rather than the disruption of a main sequence star. As a consequence of the type of star being

disrupted, the host galaxy (at $z = 0.1696$) of this TDE may contain a low-mass MBH ($M_{BH} \sim 2 \times 10^5 M_\odot$), which are difficult to find because of the small radius of influence. Furthermore, UV observations indicate a relatively cool effective temperature $T \sim 3 \times 10^4$ K, which remained constant for almost a year, while the luminosity declined by a factor ~ 50 (Strubbe & Murray, 2015).

As another example, more recently the *intermediate Palomar Transient Factory* (iPTF) discovered an optical TDE candidate (Blagorodnova et al., 2017). This event, dubbed iPTF16fnl, was discovered in 2016 and is localized in the center of a post-starburst E+A galaxy (Mrk 950) lying at a distance of 66.6 Mpc ($z = 0.016328$), making this TDE the closest in optical/UV wavelengths. The multi-band *Swift* and optical lightcurve is shown in Fig. 1.10. A best fit is also shown with a green line using the model by Guillochon & Ramirez-Ruiz (2013). iPTF16fnl is the faintest and fastest event among the optical TDEs. From Blagorodnova et al. (2017), its luminosity at peak is one order of magnitude lower than any other optical/UV TDE so far, and it has one of the shortest exponential decay timescales (~ 15 days). In addition, the host of iPTF16fnl is another example of a post-starburst galaxy, giving another suggestion that TDEs occur more often in E+A galaxies (Arcavi et al., 2014; French et al., 2016). Blagorodnova et al. (2017) estimate the MBH mass from the model, which gives $M_{BH} \sim 2 \times 10^6 M_\odot$. As a consequence, the mass of the disrupted star should be $M_* \sim 0.03 M_\odot$, which argues a low mass star or a partial disruption.

A more recent collection of 17 optically discovered TDEs by ZTF can be found in van Velzen et al. (2020).

In general, optical/UV TDEs present lightcurves with peak luminosity up to $\sim 10^{43}$ erg s^{-1}, which is followed by a temporal decay broadly consistent with $t^{-5/3}$. They present an effective temperature $T \approx 10^4$ K, which remains constant over time, and are lower than the X-ray events for which $T \approx 10^5$ K. Their total energy is also typically less than few 10^{51} erg. The majority of the low-temperature events did not have detectable X-ray emission.

There has been a recent discovery of a TDE with a particularly rich dataset. ASASS-14li includes spectra and lightcurves in soft X-rays (Miller et al., 2015), optical and near-UV (Cenko et al., 2016; Holoien et al., 2016b), and radio (Alexander et al., 2016; van Velzen et al., 2016). It was discovered in an optical monitoring survey by ASASSN in 2014 and its host galaxy lies at redshift $z = 0.0206$, making ASSAN-14li one of the closest TDE found. Its optical lightcurve has been described as exponential with a decay time of $\simeq 60$ days. The spectra indicate that it mantained a nearly constant color temperature at $\simeq 3.5 \times 10^4$ K over a period of several months. The first X-ray observations were less than a week after discovery and the flux reached a peak 20-30 days after discovery. Fig. 1.11 shows the flux decay of ASASSN-14li as observed by *Swift*. The gray band denotes the $t^{-5/3}$ flux decay as predicted by fundamental theory. The V-band light is consistent with a shallower $t^{-5/12}$ decay, indicating that there is direct thermal emission from the disc or reprocessed emission. Two different groups monitored the flare's radio flux and give different explanations. Alexander et al. (2016) attribute much of the low-frequency flux to a pre-existing, time-steady and optically thin synchrotron source. On the other hand, van Velzen et al. (2016) argue that the pre-existing source is suppressed and then replaced by a jet. ASASSN-14li, with such a complete dataset and different interpretations, invites to further analyses
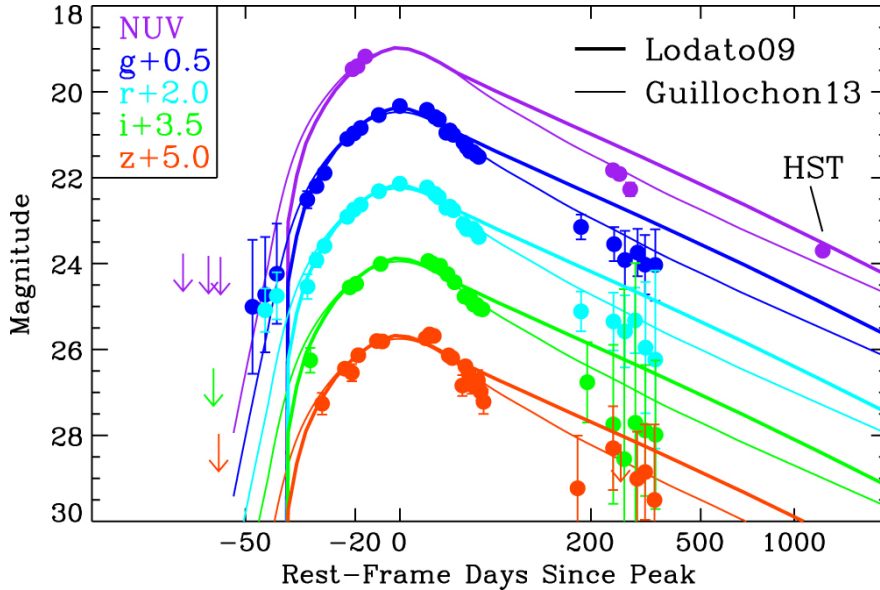
Figure 1.9: Optical/UV lightcurve of TDE PS1-10jh, observed in the g, r, i, z bands by *PanSTARRS* and near-UV by *GALEX*. One point in the UV was measured by *Hubble Space Telescope*. The data is fitted with models by Lodato et al. (2009) (thick lines) and Guillochon & Ramirez-Ruiz (2013) (thin lines). From Gezari et al. (2015).

(e.g. Krolik et al., 2016).

There are few TDEs which have been found to be particularly energetic and present a relativistic jet. In fact, a new chapter in the study of TDEs started when *Swift* J1644+57 (Bloom et al., 2011; Levan et al., 2011; Burrows et al., 2011; Zauderer et al., 2011) was detected by the *Swift* satellite, and at first seemed to share similarities to GRBs. This event was characterized by a rapid rise, long duration, luminous and energetic emission in the hard X-ray and γ-ray bands, as well as a compact and variable associated emission in the radio band, and an optically inactive galaxy ($z = 0.353$). This TDE high luminosity can be explained considering a relativistic jet beamed towards our line of sight. In addition, in the first few days after discoveries the X-ray lightcurve features large amplitude variations, with possible quasi-periodicity of 200 s (Reis et al., 2012), then it decays $\propto t^{-5/3}$, and suddenly drops after ~ 500 days (Zauderer et al., 2013). The discovery of this TDE triggered a number of theoretical studies, addressing the trajectory and type of the disrupted star and mass and spin of the MBH, and the nature of the radio emission and jets (Shao et al., 2011; Krolik & Piran, 2011; Metzger et al., 2012; Krolik & Piran, 2012). Interesting questions were also raised regarding the role of the magnetic fields in jet formation models and whether they are generated in situ in the disc. These questions stem from the fact that the estimated magnetic field strength is much higher than that of a main-sequence star, so it should be generated by the disc.

Swift also detected a second jetted TDE, *Swift* J2058+05 (Cenko et al., 2012). It is characterized by a luminous, long-lived X-ray outburst with peak isotropic X-ray luminosity $\approx 3 \times 10^{47}$ erg s^{-1}, a X-ray lightcurve with rapid variability, strong radio emission, and an optically inactive host galaxy ($z = 1.185$). Like
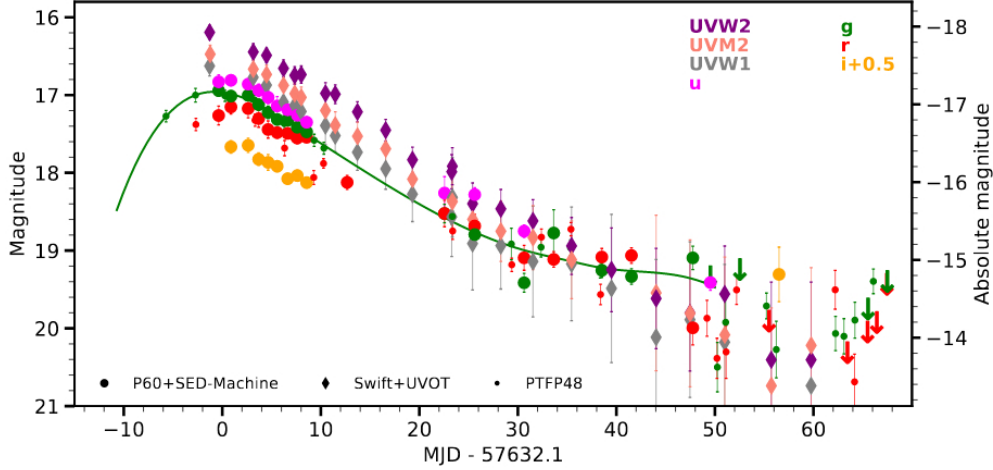
Figure 1.10: Observed lightcurve for TDE iPTF16fnl. The green line shows the best fit to the *g*-band data corrected for Galactic extinction. The peak time (MJD 57632.1) in *g*-band is taken as the reference epoch. From Blagorodnova et al. (2017).

Swift J1644+57, this event also shows an sudden drop after 200-300 days.

These two TDEs posed some questions on whether and when a TDE can launch a powerful radio jet. Jets similar to *Swift* J1644+57 were expected to be detected by deep radio follow-ups, which is not the case. Thus, the discovery of jetted TDEs influenced the study of jets formation, re-exploring the parameters which allow such phenomena.

Multiwavelength observations of TDE candidates allow to improve our understanding of the mechanisms undergoing in these events. More observational data is available from wide-field optical surveys as *ZTF* and *Gaia*, and the TDE sample will be significantly increased with up to thousands of candidates with the upcoming surveys such as *LSST* in the optical band and *eROSITA* in the X-ray band. In addition, the combination of radio and X-ray data from *SKA* and *ATHENA* is expected to increase the detection of jetted TDEs.

1.4 State of the art in tidal disruption events theory

A TDE occurs when a star passes too close to the MBH, that the tidal field is able to overcome the stellar self-gravity, and as a consequence the star is torn apart. The TDE process was initially studied by Hills (1975) as a mechanism to fuel AGN. The basic theory concerning TDEs as a mean to identify the presence of quiescent MBHs in nearby galaxies has been developed in the late 70s and 80s (Lacy et al., 1982; Rees, 1988; Phinney, 1989; Evans & Kochanek, 1989). The discovery of the first jetted TDEs by *Swift* started a new effort in understanding the physics governing these events, and now, relatively to the '80s, there are available many more detailed hydrodynamical models (see e.g. Rossi et al., 2020, for a review), which can be compared to observational data. There is still work to do regarding the models, since there are none that can describe accurately all
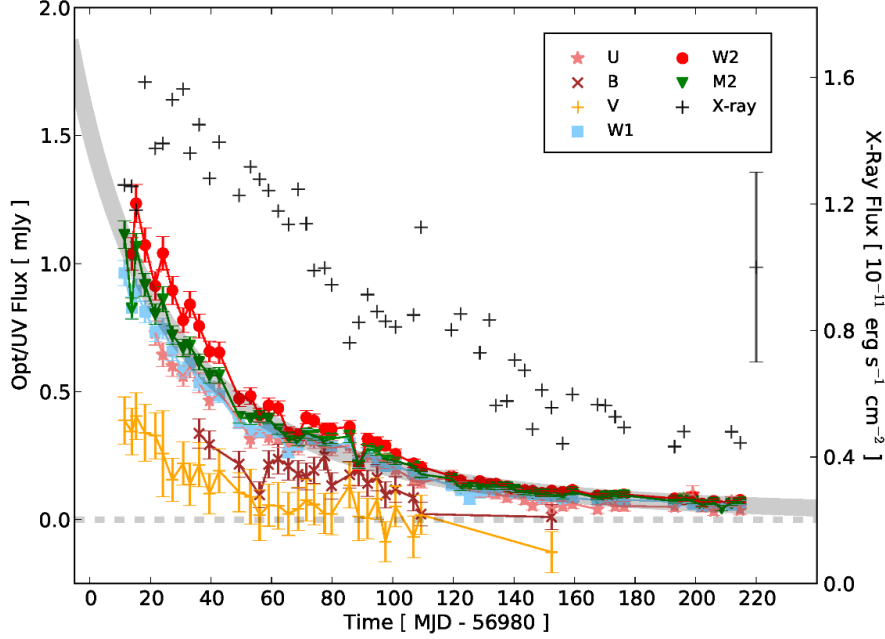
Figure 1.11: Multiwavelength lightcurve of ASASSN-14li, based on observations from *Swift* satellite. Colors denote different bands. The errors shown are the 1σ confidence limits on the flux in each band. The gray band depicts the $t^{-5/3}$ flux decay as predicted by fundamental theory. The X-ray flux points carry relatively large errors, so one representative error is shown. From Miller et al. (2015).

the observed TDEs. One example regards the selection of TDEs: this used to be done according to the shape of their optical/UV lightcurve, which is expected to be described by a $t^{-5/3}$ power law decline (Gezari et al., 2009, 2012). However, Lodato & Rossi (2011) found that this decline is actually not expected for the optical/UV. Instead, the power law should track the weaker temperature evolution of the system. As a consequence, this led to revised TDE models, which include reprocessing of the disc emission by outer debris (Guillochon et al., 2014). Numerical simulations have always played a big role in understanding the hydrodynamics of the processes governing TDEs. The dynamics of a TDE is relatively complex, indeed it involves hydrodynamics of a self-gravitating fluid (representing the star) that is subject to a relativistic force from a MBH. As such, a correct treatment of a TDE would include general relativistic (magneto)-hydrodynamics with heating and radiation (see Lodato et al., 2020, for a review on TDE simulations). Over the years a lot of work has been done to study the process of the debris fallback and the accretion disc formation, and it has been shown that relativistic effects such as relativistic precession are important to determine the self-crossing of the debris stream and lead to circularization. In addition, the resulting disc properties depend on the cooling property of the gas. Works have been carried out also to study how magnetic fields would affect the TDE evolution. Furthermore, recent models take into account Lense-Thirring precession in the presence of a Kerr MBH. More detailed reviews on the state of the art in TDE theory and simulations can be found in Lodato et al. (2015); Rossi et al. (2020); Lodato et al. (2020).

In the Chapter 2, we are going into more detailed theory.

1.5 Importance of tidal disruption events

One of the initial ideas was to use TDEs as tracers of dormant MBHs in quiescent galaxies, but with more TDEs being discovered and with more observatories and surveys being available TDEs turned to be events that can be exploited in different ways.

Since TDEs can reach distances very close to the Schwarzschild radius, they can be used to probe relativistic effects such as apsidal and nodal precession TDEs can be used to probe relativistic effects via emission line profiles (e.g. Štolc & Karas, 2019) or precession effects in the Kerr metric (e.g. Dai et al., 2013; Guillochon & Ramirez-Ruiz, 2015; Shiokawa et al., 2015; Franchini et al., 2016; Liptai et al., 2019). TDEs provide a good opportunity to study the accretion physics (e.g Strubbe & Quataert, 2009; Mageshwaran & Bhattacharyya, 2020, and references therein) during accretion at high rates and near the last stable orbit (e.g. Shen & Matzner, 2014), and can provide a new method to measure not only the MBH mass, but also its spin (e.g. Sponholz, 1994; Kesden, 2012a,b; Mummery & Balbus, 2020). The maximum mass of a MBH that can disrupt a star depends on the MBH spin (e.g. Kesden, 2012a), rising the prospect of using TDEs as probes of general relativity. An interesting example of how TDEs can be used is given by Lu et al. (2017), who demonstrate that samples of TDEs may rule out exotic alternatives to Kerr black holes, such as boson stars.

TDEs occurring in environment rich in gas will illuminate the circumnuclear material and the reprocessed emission lines give the opportunity of reverberation mapping the cores of quiescent galaxies (e.g. Komossa, 2015). They can potentially help in revealing the population of IMBHs , for which there are no firm observational evidences yet (e.g. Baumgardt et al., 2006; Fragione et al., 2018; Chen & Shen, 2018; Sakurai et al., 2019). TDEs can tell us if the MBH is a binary or if it is recoiling: this can be argued from the fact that TDE rates are enhanced under these conditions (e.g. Chen et al., 2009; Schnittman, 2010; Stone & Loeb, 2011; Coughlin et al., 2017) and they can occur off-nuclear.

Although there are only three firmly established candidates of jetted TDEs up to date (Bloom et al., 2011; Cenko et al., 2012; Brown et al., 2015b), they can potentially provide in the future new insight into the formation and early evolution of radio jets, and shed new light on issues like the cause of the radio-loud radio-quiet dichotomy[2] of AGN (e.g. Gopal-Krishna et al., 2008). Stellar dynamics in galactic nuclei is on spatial scales which cannot be resolved directly, however, since TDE rates depend on stellar dynamics, they also trace it, giving us a tool to investigate it (e.g. Stone & Metzger, 2016).

From the properties of a TDE, we can not only infer properties of the MBH that caused it, but also of the disrupted stellar object. We can find out not only the mass of the star (e.g. Blagorodnova et al., 2017), but also its type with spectroscopical data (Arcavi et al., 2014, e.g.). As a consequence we can

---

[2]The so-called radio loudness of an AGN is usually defined as the ratio of its radio and optical flux densities or luminosities at two specific frequencies. The radio-loud/radio-quiet dichotomy is a bimodality that can be encountered in the radio loudness distribution of AGN. This dichotomy is an on-going topic, whose resolution is important if one wants to fully address the accretion BH physics, jet formation and feedback (see Broderick & Fender, 2011, and references therein).

have detailed information on the stellar population of the host galaxy nucleus. Then, although depending on the models used to fit the TDE data, we could also determine if the star is fully or partially disrupted, and how near the MBH it plunged in (e.g. Blagorodnova et al., 2017).

CHAPTER 2

TDE theory

Occasionally stars in a galactic nucleus are perturbed and placed on orbits, which bring them too close to the MBH and they are tidally disrupted, losing part or all their mass in a TDE. Although the encounter between the star and the MBH is relatively close to the latter, we can still derive much of the relevant physics of a TDE in a Newtonian framework. In this chapter, we are going to describe the TDE theory following its evolutionary stages: scattering into the loss cone (Sec. 2.4), pericenter passage (Sec. 2.2), debris stream evolution and debris fallback (Sec. 2.3), disc formation (Sec. 2.4), jet formation (Sec. 2.5).
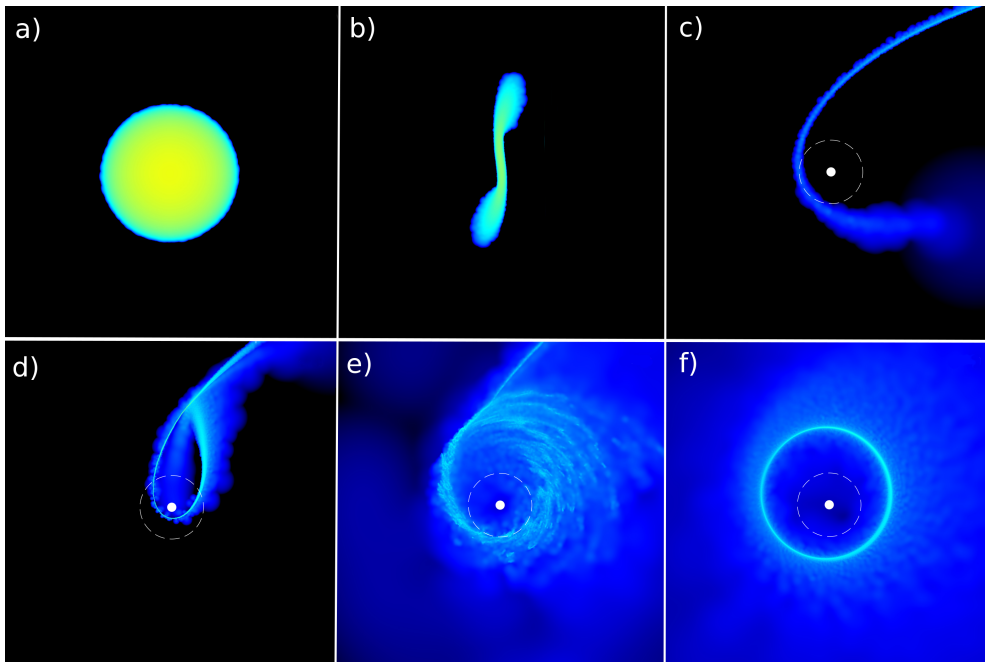
Figure 2.1: TDE stages. The MBH is shown as a white circle with radius equal to r_{ISCO}, while the dashed circle denotes the tidal radius. Panel a) shows the star when is still approaching the MBH; panel b) shows the wings formed after the first passage to pericenter of the star; panel c) shows the debris stream returning to the MBH; panel d) shows the debris self-crossing with itself; panel e) shows debris circularization and beginning of disc formation; panel f) shows the remnant disc.

2.1 Disruption conditions and loss cone

A MBH in the galactic nucleus can be thought of as a sink, which removes stars as they come sufficiently close to it. The removal of a star can occur in two ways, depending on the mass of the MBH and on the star's properties: swallowed by falling inside the event horizon, or disrupted by the tidal forces of the MBH. In the case that the star is a compact object, such as a neutron star or a BH, tidal stresses due to the MBH do not affect it, and the star is swallowed. This fate can happen also to ordinary stars, if they meet the conditions to resist being shred apart by the MBH tidal forces.
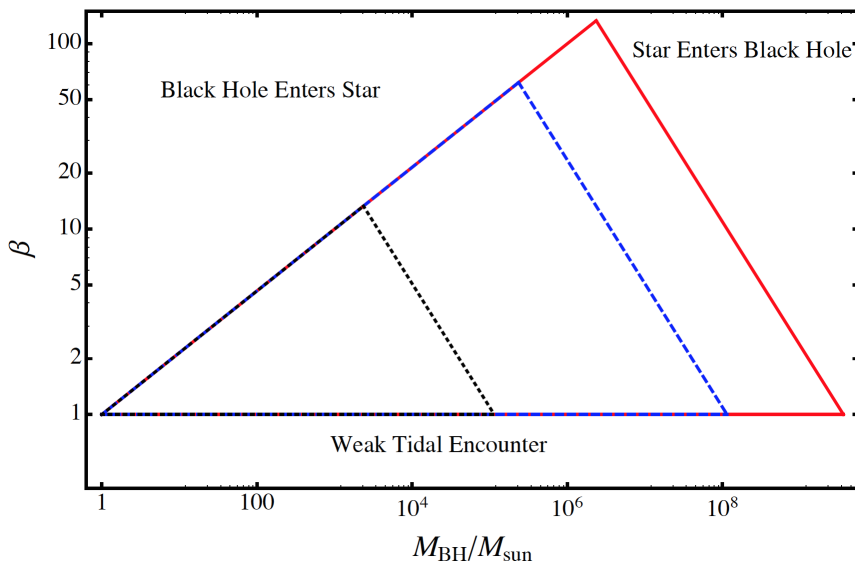
Figure 2.2: Parameter space of tidal disruption. Adapted from Stone (2013).

The critical distance from the MBH at which a star can be torn apart is called tidal radius, r_t. It can be estimated by equating the acceleration due to self-gravity $a_g \approx GM_*/R_*^2$, where M_* is the mass of the star and R_* is the radius of the star, and the tidal acceleration $a_t \approx GM_{BH}R_*/r^3$, which gives

$$r_t \simeq R_* \left(\frac{M_{\mathrm{BH}}}{M_*} \right)^{1/3}. \tag{2.1}$$

We define the depth of the encounter with penetration factor

$$\beta \equiv \frac{r_t}{r_p}, \tag{2.2}$$

where r_p is the pericenter distance of the star orbit.

In the simple case of a non-spinning MBH, the event horizon, defined by the Schwarzschild radius, r_s, grows linearly with its mass

$$r_s = \frac{2GM_{\mathrm{BH}}}{c^2}, \tag{2.3}$$

while from Eq. 2.1 it can be seen that r_t grows as $M_{BH}^{1/3}$. It follows that there is

a MBH critical mass

$$M_{\mathrm{crit}} = 1.1 \cdot 10^8 M_\odot \left(\frac{R_*}{R_\odot} \right)^{3/2} \left(\frac{M_*}{M_\odot} \right)^{-1/2} \tag{2.4}$$

above which the star is swallowed whole by falling into the horizon and tidal disruption doesn't occur. Thus, such events are not interesting from the point of view of electromagnetic flares, and Eq. 2.4 implies that for stars with $1M_\odot$ and $1R_\odot$, tidal disruption occurs for black holes with $M_{\mathrm{BH}} \lesssim 10^8 M_\odot$.

The estimate of the tidal radius r_t assumes that the gravitational field of the MBH is that of a Newtonian point particle, which is valid only at large distances, that is for $r_t >> r_s$. In the general relativistic treatment of a Kerr MBH, the tidal radius and thus the MBH critical mass can change according to the spin of the MBH (Ivanov & Chernyakova, 2006; Kesden, 2012b).
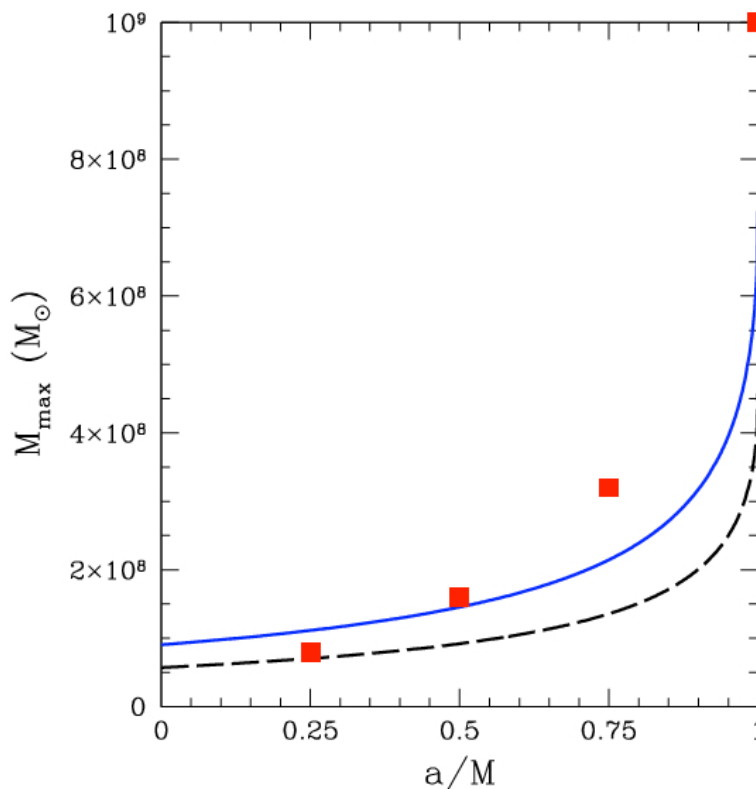
Figure 2.3: Plot shows the maximum mass M_{max} of a MBH capable of disrupting a star of $1M_\odot$ and $R_\odot$ as a function of the MBH spin a/M. The blue line shows the relativistic prediction, while the dashed black line shows the Newtonian prediction. Red squares are values of the estimation by Ivanov & Chernyakova (2006). Figure from Kesden (2012b).

Theoretical estimates of MBH spins depend on the extent to which the MBH grows by accretion or mergers. For example, a MBH accreting from a standard thin disc can attain a limiting spin $a/M \simeq 0.998$, after increasing their mass by a factor $\sim \sqrt{6}$ (Thorne, 1974; Bardeen, 1970). On the other hand, for MBHs formed in mergers the spin varies depending on whether the spins of the initial binary BHs become aligned with their orbital angular momentum prior to merger (Berti & Volonteri, 2008).

Kesden (2012b) estimated the mass of the heaviest MBH that can disrupt a star of mass $M_* = 1M_\odot$ and radius $R_* = 1R_\odot$ as a function of the MBH spin a/M. In Fig. 2.3, their relativistic and Newtonian predictions are shown in blue line and dashed black line, respectively (in the plot they compare their results with the estimate done by Ivanov & Chernyakova (2006), denoted with red squares). The relativistic estimate for tidal disruption by a Kerr MBH is given by

$$r < r_t = \left[\left(\frac{|\beta_-|}{M_{BH}/r^3} \right) \left(\frac{M_{BH}}{M_*} \right) \right]^{1/3} R_*,$$
(2.5)

where β_- is the numerical value of negative value of the tidal tensor in Eqs. 9A, 9b, 9c, and 9d from Kesden (2012b). In the Newtonian limit, the eigenvalue is equal to $\beta_- = -2M_{BH}/r^3$, giving for the Newtonian estimate

$$r < r_t = \left(\frac{2M_{BH}}{M_*} \right)^{1/3} R_*.$$
(2.6)

Using these estimates, Kesden (2012b) find that for MBHs with $M_{BH} \gtrsim 10^7 M_\odot$, a significant fraction of solar-type stars will directly plunge in the MBH horizon, thus reducing the TDE rate. Above $M_{BH} \simeq 10^8 M_\odot$, only highly spinning MBH ($a/M_{BH} \gtrsim 0.9$) will be able to produce observable TDEs.

As it will be briefly reviewed in Sec. 2.1.1, there are different scattering mechanisms from which the final orbit depends on. In general we can expect stars in a galactic nucleus to be more likely scattered onto highly eccentric orbits.

Nuclear stellar cluster with a central MBH are dense environments where interactions between stars play an important role. Although they are very dense environments, the MBH dominates their gravitational potential, resulting in stars moving on nearly stationary Keplerian orbits. The stellar gravitational potential leads to small perturbations that modifies the potential of the MBH. However, these small perturbations, together with corrections from general relativity, drive the long-term evolution of the stellar cluster.

In the classic loss cone theory, stars are supplied to the MBH via gravitational scattering onto low angular momentum orbits, while high feeding rates are achievable when the gravitational potential near the MBH is non-axisymmetric and orbits are chaotic. We now briefly explain the concept by which stars are supplied by angular momentum diffusion into the so-called loss cone of the MBH.

A schematic of the loss cone is shown in Fig. 2.4. In the context of TDEs, the loss cone radius $r_{\rm LC}$ corresponds to the tidal radius $r_{\rm t}$ for stars of a given type. An orbit that grazes the loss cone sphere at $r = r_{\rm LC}$ has angular momentum value

$$J_{\rm LC} \approx \sqrt{2GM_{\rm BH}r_{\rm t}}.$$
(2.7)

Orbits with $J \leq J_{\rm LC}$ are called loss cone orbits (sometimes the ensemble of such orbits is just called the "loss cone"). The loss cone can be also thought of a region in velocity space, that is a set of velocity vectors, which lie at a distance r from the MBH and are associated to orbits that pass within $r_{\rm LC}$. For the condition to be satisfied, a star's velocity vector must lie within a cone of opening angle $\theta_{\rm LC}$,
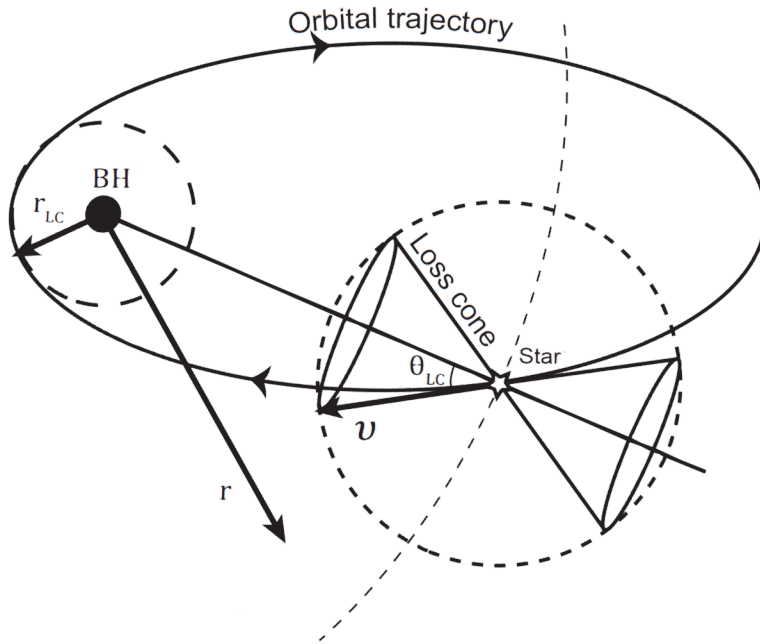
Figure 2.4: Representation of a loss cone. Stars with orbits with velocity vectors that fall within the cone defined by aperture $\theta \leq \theta_{\mathrm{LC}}$ will pass within the capture or disruption sphere at r_{LC}. Adapted from Merritt (2013).

which is given approximately by

$$
\begin{aligned}
\theta_{\mathrm{LC}} &\approx \sqrt{\frac{r_{\mathrm{LC}}}{r}}, && r \lesssim r_{\mathrm{infl}} \\
&\approx \sqrt{\frac{r_{\mathrm{LC}} r_{\mathrm{infl}}}{r^2}}, && r \gtrsim r_{\mathrm{infl}}
\end{aligned}
\tag{2.8}
$$

where

$$
r_{\mathrm{infl}} \equiv \frac{GM_{\mathrm{BH}}}{\sigma^2} \approx 10 \left(\frac{M_{\mathrm{BH}}}{10^8 M_\odot}\right)\left(\frac{\sigma}{200 \ \mathrm{km \ s^{-1}}}\right)^{-2} \mathrm{pc}
\tag{2.9}
$$

is the MBH's gravitational influence radius, and σ is the stellar velocity dispersion of the galaxy (Merritt, 2013).

In a spherical galaxy, the stars that satisfy the condition given by Eq. 2.7 are a small number, and they are removed from the loss cone at first pericenter passage. It follows that a mechanism to refill the loss cone is needed in order to have a continuous supply of stars. The efficiency of said mechanism will determine the supply rate of stars. The best-known repopulation mechanism is by gravitational encounters, which cause the stellar orbital elements to gradually evolve over time. However, if we consider non spherical galactic nuclei, that is those with an axisymmetric or triaxial potential, the feeding rates can be high even without encounters: the distributed mass will cause fixed torques that will change orbital angular momenta on a smaller timescale than that associated to gravitational encounters. Even if we were to consider a perfect spherical nucleus, the gravitational encounters timescale called the relaxation time, may be longer than the age of the Universe. The loss cone repopulation rate may occur at a rate strongly dependent on the initial conditions, and these are te main reasons why is

not possible to compute TDE rates for individual galaxies with good confidence.

The TDE rate are currently uncertain. Typically, it is estimated a rate of $\sim 10^{-5}$ yr^{-1} per galaxy from X-ray and optical/UV events. However, this rate are an order of magnitude lower than theoretical predictions of $\gtrsim 10^{-4}$ yr^{-1} per galaxy (Stone & Metzger, 2016, and references therein), which means there is a certain tension between theory and observations. Stone & Metzger (2016) calculate the rates of stellar TDEs due to two-body relaxation in galactic nuclei, and their results either kept the current discrepancy or heightened it. It must be noted that their estimates rely on conservative assumptions, that is spherical symmetry and neglect the influence of nuclear stellar clusters.

2.1.1   Scattering mechanisms

Stars in a stellar system will inevitably influence each other's trajectories due to gravitational encounters over the course of many orbits. There are different scattering mechanisms, we list some of them:

- two-body relaxation;

- resonant relaxation;

- non-spherical galactic nuclei (axisymmetric, triaxial);

- nuclear stellar disc;

- nuclear bars;

- binary MBHs.

The standard and most simple invoked scattering mechanism is two-body relaxation, which is driven by local scatterings. A star gravitationally interacts with another star and their individual angular momenta are changed, thus driving the stars into the loss cone. However, to deliver a star into the loss cone, it is necessary to reduce its orbital angular momentum to a very small value. In spherical geometry, this can be only achieved by two-body relaxation, but the time needed is typically very long. A timescale associated with this process is the relaxation time, during which stellar velocity changes by order unity and it is given by

$$t_r \sim \frac{0.34\sigma_*^3}{G^2 M_* \rho ln\Lambda}, \tag{2.10}$$

where σ_* is the stellar velocity dispersion, ρ is the density of stars, M_* is the stellar mass, and $ln\Lambda$ is the Coulomb logarithm (Λ is the ratio between the largest and smallest impact parameters possible in the system for elastic collisions) (e.g. Alexander, 2005; Merritt, 2013).

Another very well known mechanism is resonant relaxation (Rauch & Tremaine, 1996). It is an efficient mechanism to change the angular momentum of stars, which results from the coherent motion of the stars along their nearly fixed Keplerian orbits. Resonant relaxation occurs in potentials with a high degree of symmetry, like a Keplerian potential. In a nearly Keplerian potential, orbits will be fixed over many periods, leading to a coherent buildup of torques on each orbit (Rauch & Tremaine, 1996), as opposed to the uncorrelated changes from

two-body relaxation. Rauch & Ingalls (1998) suggested that the rapid changes in orbital eccentricity produced by resonant relaxation may enhance TDE rates at small scales. However, Merritt et al. (2011) found that the combination of resonant relaxation and general relativistic precession gives rise to a Schwarzschild barrier, which quenches resonant relaxation for stars with small semi-major axis.

If the galaxy cannot be considered precisely spherically symmetric, then the angular momenta of stars are not conserved and they are driven into the loss cone by collisionless torques (e.g. Norman & Silk, 1983), as opposed to two-body relaxation which is collisional. In recent studies (e.g. Merritt & Poon, 2004) it has been suggested that the non-Keplerian triaxial potential in galactic nuclei may keep the capture rate well above that of a similar spherical system. An example of four major orbits families which can be found in a triaxial nucleus in the vicinity of the MBH is shown in Fig. 2.5. A significant enhancement to the TDE rate can occur if the central distribution of stars is axisymmetric or triaxial. While in the case of non-spherical potentials the orbits generally fail to conserve all components of angular momentum, orbits in fully triaxial potentials generally conserve no components of angular momentum (Stone et al., 2013). As a consequence, over many orbital times, a stars orbit will go through pericenter of arbitrarily low value, eventually falling inside the tidal radius and the star getting disrupted. Axisymmetric potentials can lead to modest TDE rates with factors of a few enhancement (Magorrian & Tremaine, 1999; Vasiliev & Merritt, 2013). Orbits in these potentials still conserve the component of angular momentum parallel to the symmetry axis, but in a fully triaxial potential no component is conserved (Poon & Merritt, 2004), leading to a subpopulation of stars on centrophilic and chaotic orbits; in such scenario the TDE rate can be enhanced by a factor ~ 10 relatively to the rate given by the two-body relaxation (Merritt & Poon, 2004).

In the GC there is a rotating stellar disc of young stars (Bartko et al., 2010). In this case, the presence of the disc can modify the relaxation timescale. The star cluster is flattened and disc-like, thus the non-resonant relaxation timescale drops due to greater encounter rates between stars (Hayasaki et al., 2013). For instance, Kocsis & Tremaine (2011) estimated the two-body relaxation timescale as $t_r \sim 4 \times 10^8$ yr, assuming the stellars disc mass $\sim 5000 M_\odot$ (Paumard et al., 2006). Assuming a typical stellar mass of $10 M_\odot$, the disc star TDE rate of $\sim 10^{-6}$ yr^{-1}, implying that if similar discs are common in other galaxies, they could contribute to the total TDE rate (Hayasaki et al., 2013).

An interesting mechanism is given by nuclear bars (Englmaier & Shlosman, 2004; Hamers & Perets, 2017). About 1/3 of barred galaxies host a secondary (nuclear) bar in the central region, in addition to the primary large-scale stellar bar, forming a nested bar system. Double barred galaxies have been observed already in the '70s, however they were classified as having triaxial (elliptical) bulges, instead of nuclear bars. Nuclear spiral arms are observed in 50% to 80% of both active and quiescent galaxies (e.g. Laine et al., 1999; Regan & Mulchaey, 1999; Pogge & Martini, 2002), and are considered to be the small-scale variants of galactic-scale spiral arms. In a similar way as the galactic-scale spiral arms, the nuclear-scale ones can perturb the orbits of stars in certain regions of the central few hundred pc around the MBH. In particular, nuclear spiral arms can drive stars onto orbits which bring them very close to the MBH, triggering strong interactions such as stellar TDEs and stellar binary TDEs (Hills, 1988). In the latter case, one
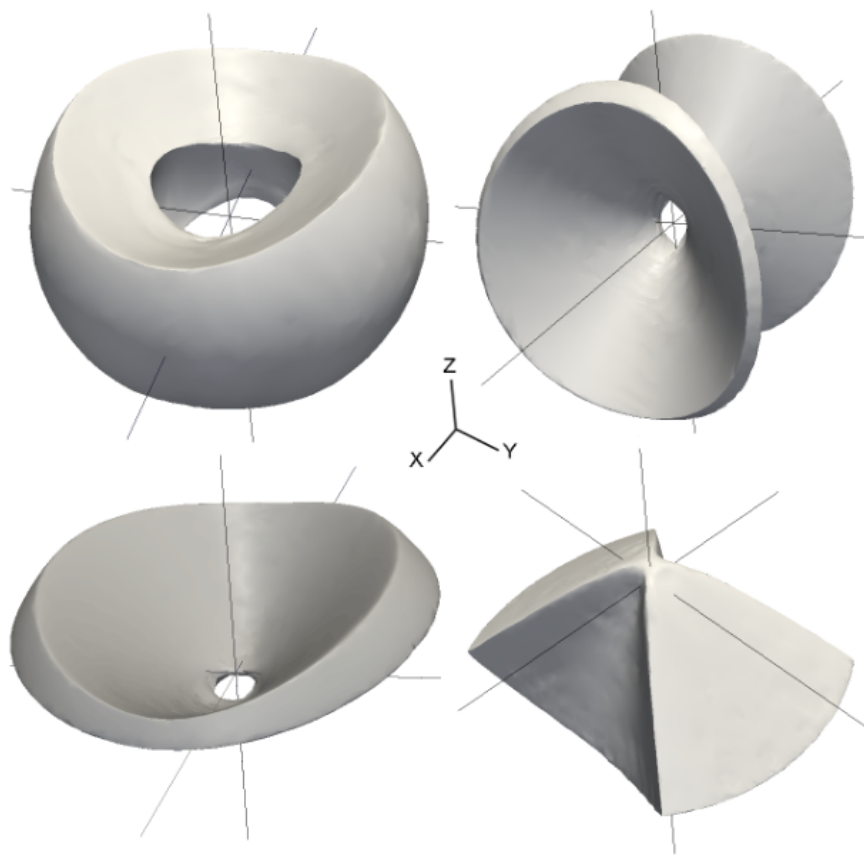
Figure 2.5: Four major orbits families which can be found in a triaxial galactic nucleus. From Vasiliev (2014).

of the binary stars remains bound to the MBH in a close eccentric orbit, while the other stars is ejected at high speeds (~ 1000 km s^{-1}). This scenario is favourable to explain both the presence of S-stars in the GC (Genzel et al., 2003; Eisenhauer et al., 2005; Gillessen et al., 2009), and the so called hypervelocity stars, which are stars moving with unusual high speeds and not bound to the Galaxy (see Brown, 2015, for a review). However, for stellar binaries the rates estimated from relaxation by stars are too low to explain the observed number of S-stars and hypervelocity stars (Yu & Tremaine, 2003). It can be considered, though, that relaxation can also be driven by massive structures such as giant molecular clouds and massive stellar clusters. As compared to relaxation by single stars only, the TDE rate can be up to 20% higher (Hamers & Perets, 2017). Even though it is not that high, the enhancement by nuclear spiral arms complements other models such as triaxial nuclei (Vasiliev & Merritt, 2013).

The presence of MBH binaries (Begelman et al., 1980) can affect the rate (as well as the appearance of a TDE, Coughlin et al. (2017)). When the MBH binary is still relatively wide, the secondary MBH acts as a perturber that increases the rate at which stars diffuse into the loss cone of the primary (Polnarev & Rees, 1994).As the binary evolves and approaches coalescence, the TDE rate from unbound stars is predicted to be suppressed, since stars are most likely ejected rather than being disrupted (Chen et al., 2008). Instead, the TDE rate from bound stars may be greatly enhanced (up to 10^{-1} yr^{-1}) due to the Kozai-Lidov effect (Kozai, 1962; Lidov, 1962), a secular mechanism that increases the eccentricities of the stars, driving them towards nearly-radial orbits (e.g. Ivanov et al., 2005; Chen et al., 2009).

2.2   Dynamics of encounter at pericenter

In this Section, we describe the general picture of a TDE. TDEs are observed when a star passes close enough to a MBH and is disrupted due to the tidal forces exceeding the star's self-gravity. In the case of a star approaching on a (nearly) parabolic orbit, it is predicted that about half of the stellar debris will remain bound to the MBH, while the other half gains enough energy to be unbound and to escape the gravitational attraction of the MBH (Rees, 1988). When the bound debris returns to pericenter, it will feed the MBH, giving rise to a flare of detectable radiation. The basic theory, which assumes a uniform mass distribution over energy, states that mass fallback rate $\dot{M}$ will follow a $t^{-5/3}$ power law. In the following, we review the theory in more detail.

The star is initially in hydrostatic equilibrium at a large distance from the MBH, which means that pressure forces and internal self-gravity of the star are in equilibrium. The unbalanced force is the gravitational pull of the MBH. In this condition, if we consider the star as formed of various fluid elements, each of these elements move in essentially Keplerian orbits around the MBH. Each of these fluid elements has its own eccentricity, which at this stage far from the MBH is very close to the one of the star's center of mass. As a consequence, the distribution of specific energy within the star is narrow around the energy corresponding to the center of mass of the star.

The situation changes as the star begins to approach the MBH. The Keplerian

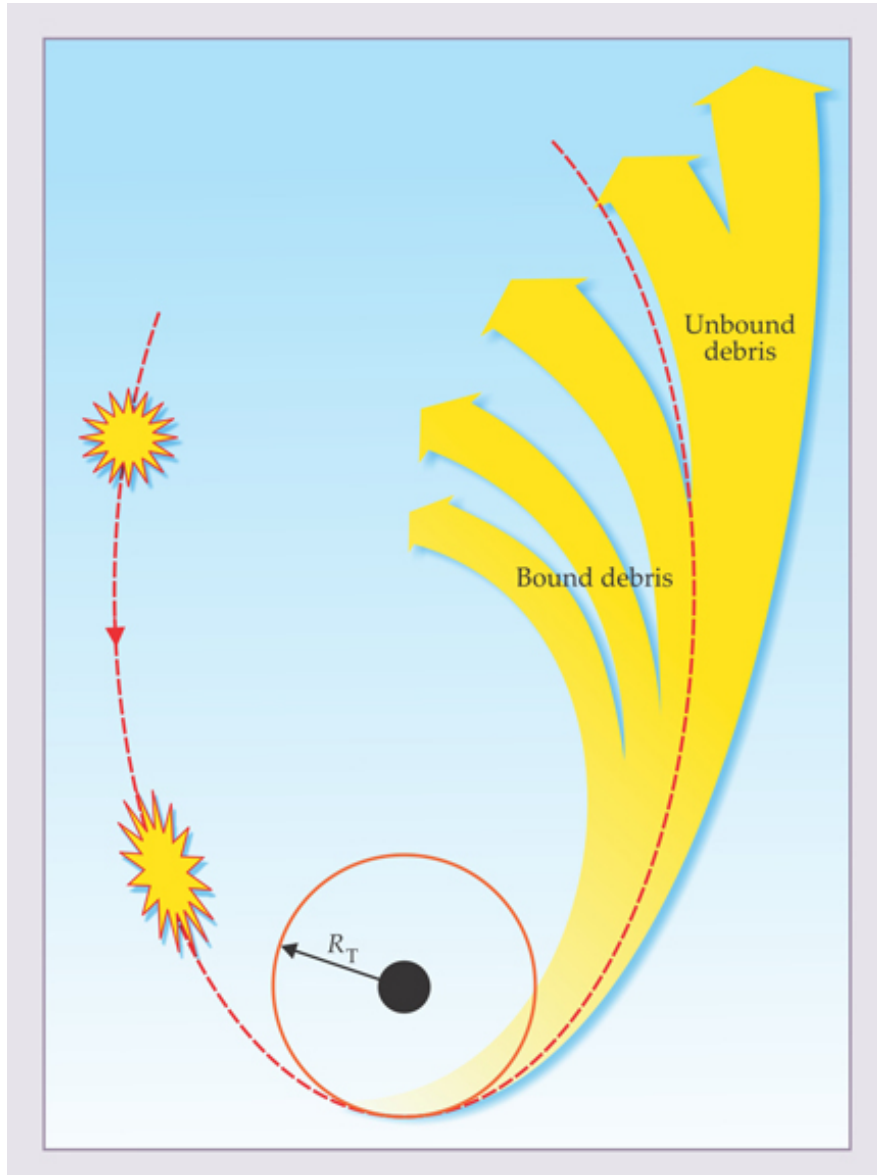Figure 2.6: Tidal disruption of a star. When the star approaches a MBH (black circle) within the tidal disruption radius r_t, it will be disrupted by the MBH's tidal forces. Roughly half of the stellar debris is gravitationally bound to the MBH and eventually forms an accretion disc. The remainder half stellar debris is gravitationally unbound and escapes the MBH's gravity. From Gezari (2014).

orbits are squeezed (this occurs in both in Newtonian dynamics and in General Relativity), hence perturbing the initial hydrostatic equilibrium. As a reaction, the star's pressure forces redistribute the internal energy, resulting in a wider specific energy distribution after the encounter of the star with the MBH at r_p. At this stage, part of the fluid elements of the star will have negative energy and part will have positive energies. Stellar debris with negative energies is bound to the MBH and will return to it, while stellar debris with positive energies is unbound and escapes the MBH's gravity. See Fig. 2.6 for a schematic representation.

What has been described above is the classical and general picture of a TDE, as it was first described by Rees (1988). In this picture, it is only the resulting redistribution of specific energies that determines the final lightcurve of the TDE. It will be explained in more detail in the next Section. In the following we now give an estimate of the spread acquired by the specific energy distribution and the final range of energies.

During the first passage to pericenter, the most important consequence is the disruption of the star, while additional effects are specific to deep disruptions, that is at high penetration factor β. From the initial hydrostatic equilibrium, the star starts to get deformed due to the MBHs tidal force influence already at a distance of few tidal radii from the MBH. In particular, the star gets stretched along an almost radial direction, due to the fact that stellar elements closer to the MBH are influenced by a larger gravitational pull. The deformation can reach order unity as the star reaches the tidal radius. The stellar debris gets a spread in orbital energy as the pressure reacts to deformation as $\Delta\epsilon$ (Eq. 2.12).

The star starts to be deformed due to the influence of the MBH tidal force at a distance of few r_t, in particular it is stretched along an almost radial direction. The deformation becomes of order unity as the stars reaches the tidal radius r_t. By the time a star passes through pericenter and is tidally disrupted, the gas moves on almost ballistic trajectories. As the star plunges into the tidal sphere (defined by r_t), the MBH tidal field overcomes internal forces, with a ratio of the tidal to self-gravitational acceleration given by

$$\frac{a_t}{a_g} \approx \left(\frac{r_t}{r}\right)^3. \tag{2.11}$$

In comparison, the work done by internal forces decreases more slowly as $\sim GM_*r/R_*^2$. However, this is a simple expression that overestimates the amount of work of internal forces, which at $r \approx r_t$ self-cancel each other to first order, with the assumption that the star is initially in hydrostatic equilibrium. As a response of pressure to the deformation the star is experiencing, the stellar debris has a spread in orbital energy, which is due to leading portions of the star sitting deeper in the MBH potential well than the trailing portions, which are in a shallower potential. The Taylor expansion of the MBH potential at the star's position gives an approximation of the debris specific energy spread (Lacy et al., 1982; Rees, 1988; Evans & Kochanek, 1989)

$$\Delta\epsilon = \pm\frac{GM_{BH}}{r_t^2}R_* \tag{2.12}$$

This expression can be understood under the impulse approximation, where the

stars is unaffected until r_t. At this point, the trajectories of the debris change instantaneously, implying the stellar elements have the same kinetic energy, which is in turn the same as the one of the star at the disruption moment. However, each debris element has a different potential energy due to their different positions within the MBH potential, resulting in an energy spread $\Delta\epsilon$. In past literature, the initial estimates of the energy spread were done with r_p instead of r_t (e.g. Lacy et al., 1982). A consequence would have been that deep encounters, which have $r_\mathrm{p} < r_\mathrm{t}$, led to large energy spreads. However, it was shown by Sari et al. (2010) and Stone et al. (2013) that Eq. 2.12 is the correct estimate. In addition, it has been found that relativistic effects produce a wider energy spread due to the stronger tidal field, which in turn leads to an early and higher peak in the mass fallback rate (Laguna et al., 1993; Kesden, 2012a).

When a star is on a parabolic orbit the orbital energy ϵ_orb of the star will be centered on zero and, due to the energy spread, stellar elements closer to the MBH have an orbital energy decrease, while those farther from the MBH have an increase in orbital energy. It follows that in general the orbital energy after disruption is distributed symmetrically around zero over a range

$$-\Delta\epsilon + \epsilon_\mathrm{orb} < \epsilon < \epsilon_\mathrm{orb} + \Delta\epsilon, \tag{2.13}$$

implying that roughly half material is bound and half is unbound (Rees, 1988). Given that the specific orbital energy is given by

$$\epsilon_\mathrm{orb} = -\frac{GM_\mathrm{BH}}{2a}, \tag{2.14}$$

where a is the semi-major axis, which is related to the pericenter r_p by $r_\mathrm{p} = (1-e)a$, we can find the new range of eccentricities of the gas elements resulting from the redistribution of energy as

$$1 - e = \pm\frac{2}{\beta}\left(\frac{M_\mathrm{BH}}{M_*}\right)^{-1/3}. \tag{2.15}$$

This forms an elongated eccentric stream (Fig. 2.6).

On the other hand, when a star is on an eccentric orbit, its specific orbital energy is given by

$$\epsilon_\mathrm{orb} = -\frac{GM_\mathrm{BH}}{2a} = -\frac{GM_\mathrm{BH}}{2r_\mathrm{t}}\beta(1-e), \tag{2.16}$$

The difference in this case is that the energy is less than zero because a is finite or, alternatively, because $e < 1$. Thus, it is possible to have a situation in which $\epsilon_\mathrm{orb} < \Delta\epsilon$, resulting in all the debris being bound to the MBH even after disruption. The condition for this to happen is $\epsilon_\mathrm{orb} = \Delta\epsilon$ from which follows a critical value for the stellar eccentricity

$$e_\mathrm{crit} \approx 1 - \frac{2}{\beta}\left(\frac{M_*}{M_\mathrm{BH}}\right)^{1/3}, \tag{2.17}$$

below which all the stellar debris should be gravitationally bound to the MBH. In

both cases of parabolic and eccentric orbits, the stellar debris energy distribution specifies the eventual fallback mass rate of the bound material.

We now discuss the effect of the penetration factor β on the approach of the star to the MBH.

The most likely encounters between star and MBH are those with $\beta \approx 1$. In this case, the star is grazing the tidal sphere, and the disruption can be partial, resulting with a surviving stellar core after passage at pericenter (Guillochon & Ramirez-Ruiz, 2013). This is a likely scenario for giant stars, since they have an external gaseous envelope which is more easily stripped by tidal forces. Then, the giant's denser core could pass around the MBH several times, losing a fraction of its mass at every encounter.

Another tidal disruption scenario is deeper encounters, given for penetration factors $\beta \gtrsim 3$. Though as not likely to occur as $\beta \approx 1$ cases, they still make about a third of TDEs (Luminet & Barbuy, 1990). Stars which undergo disruption under this condition, get compressed into a pancake (e.g. Carter & Luminet, 1982, and see also Brassart & Luminet (2008) and references therein), and suffer a vertical collapse at passage at pericenter given by

$$v_{\mathrm{c}} \approx \beta \left(\frac{GM_*}{R_*} \right)^{1/2}. \tag{2.18}$$

This strong vertical compression can cause shocks, which in turn can raise the temperature of the stellar core. Carter & Luminet (1982) thus assumed that nuclear reactions could be triggered during a deep encounter of a main sequence star. However, this possibility is under debate (e.g. Laguna et al., 1993; Kobayashi et al., 2004), and white dwarfs are more likely to produce such nuclear reactions, since they have larger initial densities (Rosswog et al., 2009a; Tanikawa et al., 2017; Tanikawa, 2018).

The pancake star was further studied with a semi-analytical affine star model, which is described in detail in Carter & Luminet (1985), both in Newtonian dynamics (Carter & Luminet, 1983; Luminet & Carter, 1986) and in General Relativity with non-spinning MBHs (Luminet & Marck, 1985). This model allowed to show that along a plunging orbit within the tidal radius r_t, the MBHs tidal field increases rapidly enough to temporarily overcome the pressure and self-gravity of the star (Carter & Luminet, 1983). Then the stellar matter is in free fall in the external gravitational field, and gets squeezed in the direction orthogonal to the orbital plane as a response to tidal effects. When it reaches the orbits pericenter, the pressure field rapidly increases within the stellar core in response to the compression. As a consequence, while the star is moving within the tidal radius, the stellar matter bounces within the core and quickly expands in an almost symmetric way to the free fall. In the relativistic case, the star is subject to multiple squeezing phases instead (Luminet & Marck, 1985).

Lastly, though statistically rare, Darbha et al. (2019) investigated the outcome of ultra-deep TDEs ($\beta \gg 1$). The stellar debris can experience extreme tidal distortion, avoiding to plunge directly into the MBH, for $\beta \gtrsim 10$ and $M_{\mathrm{BH}} \lesssim 10^6 M_\odot$. As a consequence, this type of TDEs could produce X-ray emission from either self-crossing (discussed in next Section) of stellar debris or tidal compression (as

for deep encounters). In addition, they would also produce gravitational wave emission (Kobayashi et al., 2004). A first gravitational wave signature would come from the orbital motion of the debris near pericenter, including when the debris is fully captured, while a second signature would come from the tidal deformation of the star itself. Finally, a third signature would come from unstable accretion discs (Toscani et al., 2019).

Regarding the topic of deep TDEs, we make here a final note about the importance of relativistic effects. The role of General Relativity in TDEs is discussed in Sec. 2.6. When relativistic effects are taken into account, relativistic precession plays a fundamental role in the circularisation process, which is described in Sec. 2.4. In a completely Newtonian treatment, the debris stream does not self-cross. As a consequence, kinetic energy is not removed from the debris and the specific energy remains unchanged. On the other hand, relativistic precession changes the trajectory of the debris at pericenter. An example of this comparison can be seen in Bonnerot et al. (2016). This relativistic effect has a strong impact on deep ($\beta >> 1$) TDEs, since the tidal stream self-crosses at smaller radii, steeper angles and with relatively large velocities (see e.g. Shiokawa et al., 2015; Tejeda et al., 2017). The importance of the relativistic effects is related to the ratio between pericenter distance r_p to the gravitational radius r_g (Tejeda et al., 2017).

2.3 Debris stream evolution and fallback

After disruption, the stellar debris becomes an elongated structure (Fig. 2.6). In this Section, we describe the evolution of the debris stream around the MBH.

The debris stream plays an important role in determining the evolution of circularization and following accretion, which will be discussed after this Section. It is in fact the stream cross section to determine the effectiveness of transfer of energy and angular momentum.

The stream motion is characterized by different trajectories which the debris acquired due to the energy spread during the disruption process. Both analytical and numerical studies show that the debris stream is dense enough so that its structure's hydrostatic equilibrium is kept due to interplay of self-gravity and pressure in the transverse direction Kochanek (1994). Assuming gas evolves adiabatically following $P \propto \rho^{5/3}$, it is possible to define the width H of the debris stream (Fig. 2.7) as

$$H \propto \Lambda^{-1/4} \tag{2.19}$$

where Λ is the mass per unit length, giving the linear density (Kochanek, 1994; Guillochon et al., 2014; Coughlin et al., 2016a). For gas elements close to the center of mass of the stream the linear density goes as $\Lambda \propto r^{-2}$ and as a consequence the stream's width is

$$H \propto r^{1/2}. \tag{2.20}$$

When the debris stream begin to deviate from the trajectory of the center of mass, the linear density changes to $\Lambda \propto r^{-1}$, yielding

$$H \propto r^{1/4}. \tag{2.21}$$

From these scalings we can see that the stream's width increases slowly with
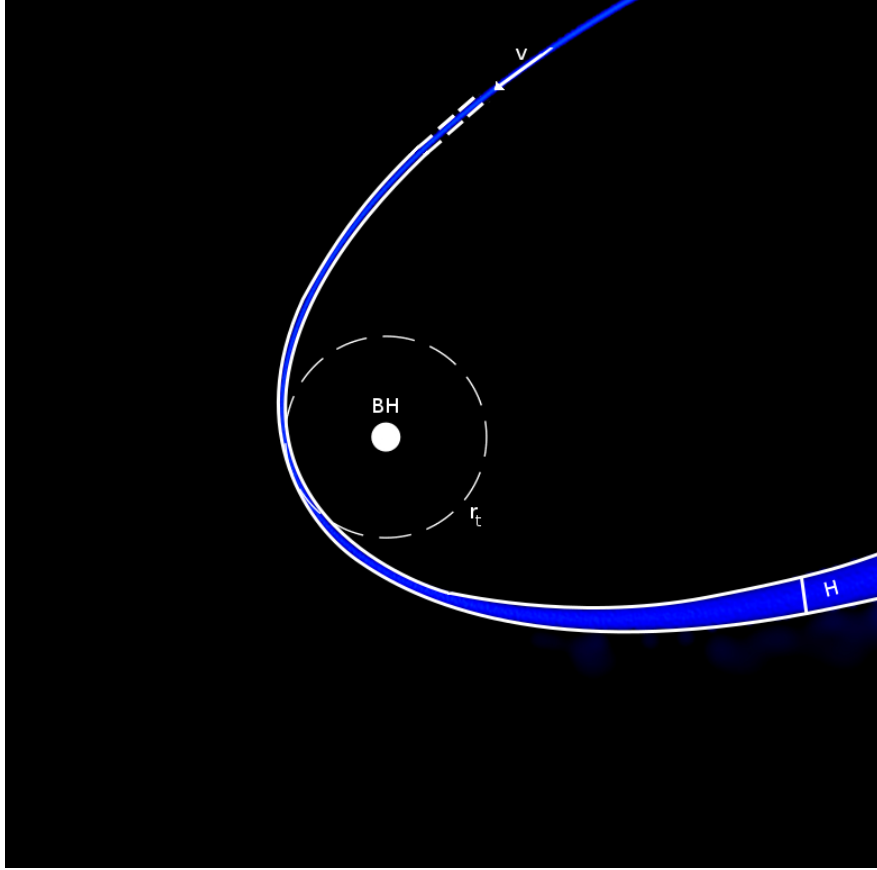
Figure 2.7: Debris stream returning to the MBH. The velocity v and width H of the stream are denoted.

distance. This is due to the effect of self-gravity, which keeps the stream into a thin shape also at distances $r \gg r_{\mathrm{t}}$. However, the role of self-gravity depends on the stream's density. If its density is too low, the gravitational force of the MBH dominates self-gravity, in which case the width scaling becomes

$$H \propto r. \tag{2.22}$$

Self-gravity of the stream can become dominant in the transverse direction (Kochanek, 1994). As a consequence it is possible to encounter a gravitational instability which may lead to fragmentation (Coughlin & Nixon, 2015; Coughlin et al., 2016a,b). It is demonstrated by Coughlin & Nixon (2015) that the stream was gravitationally unstable when the adiabatic index of the gas was set to $\gamma = 5/3$, resulting in its fragmentiation into bound clumps. These clumps, when accreted at discrete times, caused the late time fallback rate to fluctuate about the $t^{-5/3}$ average. In their following work, Coughlin et al. (2016a) found that for stiffer equations of state, that is $\gamma \gtrsim 5/3$, the collapse was induced sooner and was enhanced by a post-periapsis pancake soon after the disruption. To define whether the stream is gravitationally unstable, that is subject to fragmentation, an instability criterion for the stream can be defined with a critical density for the MBH

$$\rho_{BH} \sim \frac{M_{BH}}{r^3}. \tag{2.23}$$

It follows that the instability condition is in the form $\rho > \rho_{BH}$: the critical density falls at a rate that is steeper than the debris density with respects to radial distance from the MBH. This physically means that the rate at which the material is torn apart is slower than the rate at which aggregates, thus leading to fragmentation (Sacchi et al., 2020). Further investigation regarding what causes fragmentation was done by Sacchi et al. (2020). In particular , they explain the origin of the fragmentation in the slowing down of the stretching of the debris in the unbound portion of the stream. In addition, they find that a star modelled as a polytropic sphere with adiabatic index $\gamma = 5/3$ is in fact prone to fragmentation. However, it occurs only after more than 3 years after disruption (for standard TDE parameters), when the TDE is likely not observable any more. Sacchi et al. (2020) also describe the fragmentation process using an analytical approach, which generalizes previous results.

After passage of the star to pericenter r_{p}, the formed stellar debris moves ballistically around the MBH. In particular, the most tightly bound debris has an orbital energy $\epsilon_{\mathrm{orb}} = -\Delta\epsilon$, which correspond to orbits with the following semi-major axis and period

$$a_{min} = \frac{R_*}{2}\left(\frac{M_{\mathrm{BH}}}{M_*}\right)^{2/3}, \tag{2.24}$$

$$t_{\min} = \frac{\pi}{\sqrt{2}}\sqrt{\frac{R_*^3}{GM_*}}\sqrt{\frac{M_{\mathrm{BH}}}{M_*}}. \tag{2.25}$$

The mass fallback rate $\mathrm{d}m/\mathrm{d}t$, that is the rate at which the debris reaches the MBH, is given by

$$\frac{\mathrm{d}m}{\mathrm{d}t} = \frac{\mathrm{d}m}{\mathrm{d}\epsilon}\frac{\mathrm{d}\epsilon}{\mathrm{d}t} = \frac{1}{3}(2\pi GM_{\mathrm{BH}})^{2/3}\frac{\mathrm{d}m}{\mathrm{d}\epsilon}t^{-5/3}, \tag{2.26}$$

where $\mathrm{d}\epsilon/\mathrm{d}t$ is found from using Kepler's third law to define the energy of the most bound debris elements after a period t

$$\epsilon = -\frac{1}{2}\left(\frac{2\pi GM_{\mathrm{BH}}}{t}\right)^{2/3} \tag{2.27}$$

From how Eq. 2.26 is derived, it follows that the only term on which the mass fallback rate depends on is $\mathrm{d}m/\mathrm{d}\epsilon$. In works by Rees (1988) and Phinney (1989), it is assumed that this energy distribution is uniform, thus the standard $t^{-5/3}$ power law decay is obtained. If we consider that half the stellar mass reaches the MBH for $t \geq t_{\min}$, we can define a peak value $\dot{M}_{\mathrm{pk}}$ (Lodato & Rossi, 2011)

$$\dot{M}_{\mathrm{pk}} = \frac{M_*}{3t_{\min}}, \tag{2.28}$$

and rewrite the fallback mass rate as

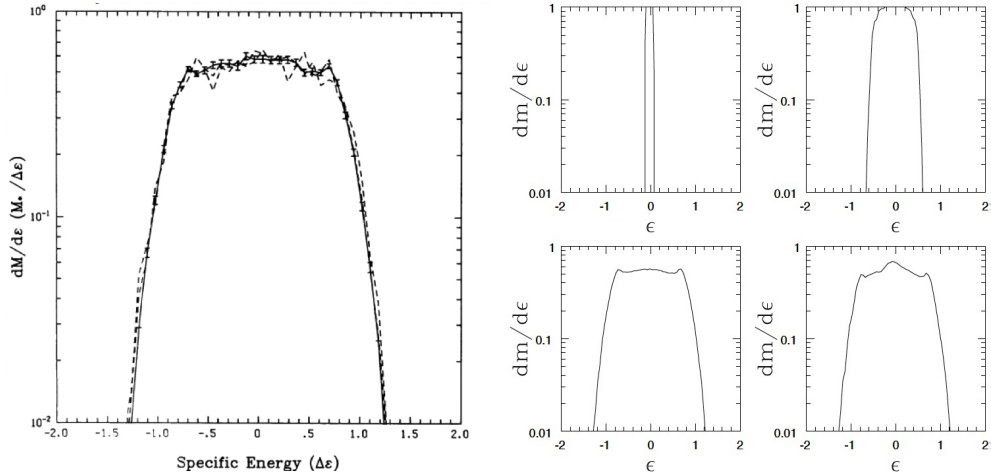$$\frac{\mathrm{d}m}{\mathrm{d}t} = \dot{M}_{\mathrm{pk}}\left(\frac{t}{t_{\min}}\right)^{-5/3}. \tag{2.29}$$

Figure 2.8: Distribution of specific energies. Comparison between Evans & Kochanek (1989) (left panel) and Lodato et al. (2009) (right panel). In the right panel, the four plots show the distribution for the initial condition (top left), when the star is at pericenter (top right), at four times the pericenter distance (bottom left) and at ten times the pericenter distance (bottom right).

Lodato et al. (2009) revisited the assumptions of this theory and found that the fallback mass rate depends on the internal structure of the star, which means that to better determine the fallback mass rate, the energy distribution $\mathrm{d}m/\mathrm{d}\epsilon$ should not be assumed uniform. The standard $t^{-5/3}$ power law is still valid, but only at later stages.

When the stellar structure is taken into account the energy distribution changes: in general there is a peak at the central value ($\epsilon \approx 0$) and decrease towards the limits. Fig. 2.8 shows a comparison between results from Evans & Kochanek (1989) (left panel) and Lodato et al. (2009) (right panel). In both works the star is modelled as a polytrope with $\gamma = 5/3$. The bottom left plot in the right panel accurately replicates the results shown in the left panel. A difference appears as the energy distribution keeps evolving with time as the star gets nearer to the MBH ($\approx 10r_p$; Lodato et al. (2009)) and it finally settles down in the distribution shown in the bottom right plot. Here the distribution is characterized by a central peak at lower energies, followed by two wings at larger energies. While the central peak is expected (Lodato et al., 2009), the wings are related to the stellar material at the surface of the star, which at pericenter is distorted from its initially spherical shape.

Recently, Law-Smith et al. (2019, 2020) performed simulations of TDEs from stars with realistic structures and compositions using MESA models Paxton et al. (2010). The results show that $\dot{M}_{pk}$ decreases with stellar age and that the time of peak of the mass fallback rate increases with stellar age, which means that younger stars can provide faster flares. These effects diminish with increasing penetration factor β. Another study using MESA based stellar density profiles to emphasize their role in affecting the mass fallback rate was done by Golightly et al. (2019b).

As a final note, it is generally assumed in the literature that the accretion rate onto the MBH traces the mass fallback rate given by Eq. 2.26, and that also the resulting flare luminosity traces the fallback rate, that is $L \propto \dot{M} \propto t^{-5/3}$. We

will return to this in the next Section.

2.4 Circularization and disc formation

In this Section we describe the processes that allow the debris stream to circularize and form an accretion disc. The process of circularization involves all the mechanisms that allow the debris stream to dissipate kinetic energy, bringing the stream's trajectories from elliptical to circular, thus forming a disc. The circularization process is not yet fully understood and there are different mechanisms involved, the main ones being pancake shock, self-crossings and shearing (Evans & Kochanek, 1989). A pancake shock occurs at star's disruption, when part of the stellar material is accelerated out of the initial orbital plane, resulting in a range on inclinations. The various orbits of the debris are vertically focused, intersecting the orbital plane close to pericenter, where the stream undergoes strong compression and a shock (Evans & Kochanek, 1989).

Self-crossings occur when the debris stream is already formed and the bound part falls back to orbit the MBH. The leading part of the stream collides with the part which is still falling back. This happens because as the leading part of the stream returns to pericenter, it experiences changes to their apsidal angles due to relativistic apsidal precession. Self-crossings generate shocks in the debris stream (Evans & Kochanek, 1989).

Also shearing occurs when the stream comes back to pericenter. At some point the debris stream orbits will have similar pericenters but different apocenters, causing an effect similar to a nozzle as the whole stream passes through pericenter, inducing shearing of the debris. In addition, this mechanism is enhanced by relativistic apsidal precession because the debris precess by different angles due to the range of pericenters, leading to more shearing (Evans & Kochanek, 1989).

From these mechanisms, two models for stellar debris circularization have been proposed in the literature. In the first model, apsidal precession due to general relativistic effects is responsible in causing tightly bound debris, after the second passage to pericenter, to intersect with less bound debris, which is still returning from the apocenter. As a consequence, shocks will form in the collision of the two gas streams, resulting in energy dissipation and eventual circularisation (Rees, 1988). A possible delay for this mechanism could be the nodal general relativistic precession given by Lense-Thirring torques, in the case of rapidly spinning MBHs (Kochanek, 1994; Dai et al., 2013; Guillochon & Ramirez-Ruiz, 2015; Hayasaki et al., 2016; Liptai et al., 2019).

In particular, Guillochon & Ramirez-Ruiz (2015) show that effects from General Relativity are important when considering the evolution of the debris stream. They find that when General Relativity effects are weak and the precession angles are small, the stream crosses itself far from the pericenter. As a consequence, it can potentially affect the mass accretion rate by reducing it and can increase the time of peak accretion by a factor ~ 100. Thus, these TDEs likely peak on timescales of several years and their bolometric luminosities decays at a rate shallower than $t^{-5/3}$. This effect works mostly for tidal disruptions around MBHs with mass $< 10^6 M_\odot$. For more massive MBHs, Guillochon & Ramirez-Ruiz (2015) find that the General Relativity effects are significantly stronger, resulting in stream

self-crossings that occur at large angles and closer to the stars pericenter. They also find different behaviours depending on the MBHs spin. In particular, if the spin is $a \lesssim 0.2$ the accretion rate onto the MBH follows the fallback rate, with no significant delay between the return of the mostly bound debris and accretion onto the MBH. If the spin is $a \gtrsim 0.2$ the stream self-crossing only occurs after the mostly bound debris orbited has gone through the pericenter many times. In this case, very little energy is dissipated since there are no self-crossings, and the specific energy of the debris is unchanged until circularisation starts. When this happens, the accretion rate will equal the fallback rate but with a fixed time delay, $\dot{M}_{\mathrm{acc}}(t + t_{\mathrm{delay}}) = \dot{M}_{\mathrm{fb}}(t)$, where $\dot{M}_{\mathrm{fb}}$ is the mass fallback rate (Guillochon & Ramirez-Ruiz, 2015). While Guillochon & Ramirez-Ruiz (2015) suggested that the MBH spin would delay circularisation due to Lense-Thirring precession causing the debris stream to change plane and avoid self-crossing, in a more recent work Liptai et al. (2019) find that nodal precession due to the MBH spin does not prevent disc formation, since it causes only a short delay. More discussion is done in Sec. 2.6.

In the second model, circularization is given by the vertical compression of stellar debris during passages at pericenter after the first. At this stage, the thin gas streams are funnelled by tidal acceleration into a vertically compressed nozzle, and the convergent flow leads to shocks. However, direct energy dissipation in the nozzle is not an efficient circularization mechanism, as it can be inferred from the following. Assuming roughly ballistic motion for the debris between first and second passages to pericenter, the specific kinetic energy of vertical collapse at r_p will be $\epsilon_{\mathrm{z}} \sim \beta^2 (GM_*/R_*)$. Even if all this energy was dissipated in shocks, the debris still has to return

$$N_{\mathrm{p}} \sim \frac{1}{2\beta} \left(\frac{M_{\mathrm{BH}}}{M_*} \right)^{2/3} \tag{2.30}$$

times to fully circularize (Stone, 2013). Even so, nozzle shocks change the orbital parameters of the debris, leading to an effective apsidal precession. The debris then circularises through collisions and shocks with itself. This type of circularisation has been seen in simulations of stars on parabolic orbits disrupted by a $10^3 M_\odot$ IMBH by Ramirez-Ruiz & Rosswog (2009); Stone et al. (2013).

Once the accretion disc is formed, its structure and evolution will depend on the efficiency and balance between the timescales of the circularization itself, radiative cooling, viscous accretion and debris infall (Evans & Kochanek, 1989). If we define the timescale of circularization, radiative cooling and viscous accretion as t_{circ}, t_{cool} and t_{visc} respectively, we can find three regimes (e.g. Bonnerot et al., 2016):

- if $t_{\mathrm{visc}} < t_{\mathrm{circ}}$, viscosity may be important during circularization;

- if $t_{\mathrm{visc}} > t_{\mathrm{circ}}$, accretion can begin only once a disc is formed;

  - if $t_{\mathrm{cool}} < t_{\mathrm{circ}}$, the disc cools during formation, resulting geometrically thin;

  - if $t_{\mathrm{cool}} > t_{\mathrm{circ}}$, the disc has an excess of thermal energy while it forms and puffs up.

Even if it is difficult to describe the correct processes of circularization of stellar

debris, it is safe enough to assume that at some point after disruption, a circularized accretion flow will exist around the MBH. Since this stage of a TDE relates directly to observations, the evolution and emission of the transient accretion disc is subject to many theoretical studies.

Bonnerot et al. (2017) developed an analytical model for the circularization process, in particular for the long-term evolution of the stream of debris under the influence of the simultaneous effect of shocks and magnetic stresses. It is demonstrated that a critical efficiency of magnetic stresses ($v_A/v_c \approx 10^{-1}$, where v_A is the Alfvén velocity and v_c is the circular velocity) exists that sets the boundary between circularization and ballistic accretion, and it is found to be largely independent of the BH mass and penetration factor β. The presence of magnetic stresses acting on the stream has the dominant effect of accelerating the stream evolution by strengthening self-crossing shocks. As a consequence, the ballistic accretion occurs very early in the stream evolution. However, the $t^{-5/3}$ decay of the luminosity lightcurve, usually associated to the optical emission (Piran et al., 2015), requires a slow stream evolution, which is favored by low BH masses, $M_{BH} \lesssim 10^6 M_\odot$. Bonnerot et al. (2017) note how this is hard to reconcile with the strong magnetic stresses necessary for the ballistic accretion scenario proposed by Svirski et al. (2017). On the other hand, in absence of magnetic stresses, the predictions of this model are qualitatively consistent with existent numerical simulations of disc formation from TDEs (e.g. Bonnerot et al., 2016). The BH spin was not considered in this model for simplicity.

Since the discs have short viscous timescales, a common assumption is that mass accretion onto the MBH depends on the supply of fallback material into the disc, instead of internal viscous processes. This leads to the generally accepted assumption that the luminosity should evolve as $L \propto \dot{M} \propto t^{-5/3}$ (Rees, 1988). However, recent works are showing that this might not be the case. Until recently, it was believed that the observed TDE emission comes from the dissipation of the debris energy as the stream falls back to the MBH. This process was assumed to occur due to the rapid formation of an accretion disc, but observational data cast doubts on this model, which now needs revision. In practice, the $t^{-5/3}$ power law evolution is valid only at late times, that is several months after the event (see Lodato & Rossi, 2011, for a discussion). In addition, most properties of TDE candidates are difficult to explain in the classical picture. The observed luminosity and temperature are lower than expected, emission radius is larger, and observed energy is significantly lower than the potential supply from accretion of the typical solar mass onto a MBH (e.g. Piran et al., 2015). Different physical process have been proposed to solve the problem, such as photon trapping (e.g. Krolik & Piran, 2012), kinetic outflow that can carry away orbital energy (e.g. Ayal et al., 2000), low-mass outflow that regulates the accretion rate (e.g. Strubbe & Quataert, 2009).

From numerical simulations it is also seen that after disruption of the star, the debris stream shocks during self-crossings when it returns to pericenter. However, this shock is weak (in the general case of star on parabolic orbit grazing the tidal sphere). As a consequence, the debris keeps following a highly eccentric orbit. A model has been suggested by Piran et al. (2015), where shocks rather than accretion onto the MBH could power the optical emission of TDEs. This model is consistent for optical TDEs and the luminosity produces by shocks is expected

to scale as $L \propto t^{-5/3}$, as it is found observationally. A problem arises in explaining the lack of X-ray emission. The model proposes that magnetic stresses can make a consistent fraction of the gas to plunge directly into the MBH (Svirski et al., 2017), however strong self-crossing would occur as the debris passes very close to the gravitational radius, resulting in some X-ray emission (Bonnerot et al., 2017).

2.5   Jets formation

During a TDE, the main electromagnetic emission comes from the flare originating as a consequence of the stellar disruption and disc formation. Another possible source of electromagnetic emission in TDEs is the launching of collimated relativistic jets, most notably the cases of *Swift* J1644+57 (e.g. Bloom et al., 2011) and *Swift* J2058+05 (Cenko et al., 2012). Such jets are seen in a wide range of accreting BH systems, but only recently has arisen the interest in TDE jets (e.g. Farrar & Gruzinov, 2009). These jets have been studied as sources of ultra-high energy cosmic rays and probes of the gaseous circumnuclear medium. In addition, the relatively clean initial conditions of a TDE make such jets ideal laboratories to examine open questions about roles played by the magnetic flux or disc-jet misalignment in jet launching mechanisms.

Observational data indicate that there is a pletora of TDE properties, indeed some TDEs are seen only in the UV/optical, others are seen in X-rays, UV/optical and radio (Tab. 1.1). However, there is a rarity of jetted TDEs, which suggests that there are specific conditions for which a jet will form. Other than the dependence on the viewing angle, it is reasonable to suppose that jet formation depends on the properties of the MBH and the star.

The work by Dai et al. (2018) studies the dependence on the viewing angle with a 3D general relativistic magnetohydrodynamics simulation of a TDE accretion disc. The authors investigated the case of a modestly rotating MBH with spin $a = 0.8$ and mass $5 \times 10^6 M_\odot$, and their models led to a mildly relativistic, wide angle and ultrafast outflow. The viewing angle-dependent spectra from their model suggests that the optical to X-ray flux ratio increases as the observer moves towards the disc plane. Even if this model doesn't apply to TDE that may launch ultra relativistic jets, it does offer a qualitative picture of how the viewing angle of the observer can affect the observed TDE properties.

A further study has been done by Curd & Narayan (2019). In their work the authors investigate the case of a solar mass star disrupted by a MBH with $10^6 M_\odot$ mass and compute the viewing angle-dependent spectra from general relativistic magnetohydrodynamics simulations of the super-Eddington MBH accretion disc resulting from the disruption. They find that an accretion disc with a relatively weak magnetic field around the MBH does not launch a relativistic jet, independently on whether the MBH is rotating or not. The same results occur for a non-rotating MBH with a strong magnetic field. The model that launches a powerful relativistic jet has a rapidly rotating MBH with spin $a = 0.9$ and a strong magnetic field, and reproduces the high-energy emission and jet structure of *Swift* J1644+57.

2.6 The role of general relativity

General relativity modifies the dynamical evolution of the star approaching the MBH on a disruption path, the stellar debris stream and the accretion disc produced by the tidal disruption (see e.g. Stone et al., 2019, for a review). In this Section, we give a brief description of effects of general relativity on TDEs.

In Newtonian gravity, a star nearby a MBH experiences tides due to the spatial gradient in the gravitational force acting on it. As a consequence, two nearby particles of the star with initially same velocity will experience different accelerations and will change their relative positions. In general relativity, gravity affects the motion of particles by determining the metric spacetime, which in turn determines the geodesic on which freely falling particles move.

Considering the TDE general picture, an important effect to consider is how general relativity can modify the orbits of the tidal streams following tidal disruption. A first consideration is that, in general, tidal debris spend most of its time near apocenter, i.e. far from the MBH. In this case, one can still use Newtonian expressions for $\mathrm{d}E/\mathrm{d}t$ even in the relativistic case. In principle, one can compare energy equations in the two cases to predict how the fallback rate differs between Newtonian gravity and general relativity. However, this comparison must be performed carefully as it is not straightforward which Keplerian orbit should be compared to which geodesic (Stone et al., 2019). A gauge-invariant choice is the comparison between a geodesic with angular momentum magnitude

$$L = \sqrt{Q + L_x^2}, \tag{2.31}$$

where Q is the Carter constant, and the Keplerian orbit with the same angular momentum. It follows that, for non-spinning MBHs described by the Schwarzschild metric, stars experience stronger tides at pericenter in general relativity than in Newtonian gravity with the same angular momentum L. An implication is that the penetration factor β for full disruption is lower in general relativity. However, although one can expect that the stronger tides in general relativity would lead to more tightly bound debris, followed by a higher fallback accretion rate, one actually finds that tidal debris is slightly less tightly bound in general relativity. For the most massive MBH capable of fully disrupting a star without capturing it, the most tightly bound debris is $\sim 77\%$ as tightly bound in general relativity as it is in Newtonian gravity (Stone et al., 2019). Assuming that the TDE luminosity traces the fallback accretion rate, i.e. $L \propto \dot{M}$, this would imply slightly fainter TDEs in general relativity compared to the Newtonian case.

Tests have been performed using hydrodynamic simulations. Cheng & Bogdanović (2014) performed TDE simulations of solar-type stars with $M_* = 1M_\odot$ and $R_* = R_\odot$, with Schwarzschild MBH masses equal to $10^5 M_\odot$, $10^6 M_\odot$ and $10^7 M_\odot$. They find that in the case of $10^7 M_\odot$ MBH, general relativity has a modest effect on the fallback rate: the peak fallback rate is reduced with respect to the Newtonian case, but the time it remains super-Eddington by $\sim 15\%$ (Fig. 2.9).

Another test with spinning MBH were performed by Tejeda et al. (2017). The authors performed TDE simulations of solar-type stars with spinning MBHs. Their work shows that the penetration factor β and the MBH spin have little effect both on the debris energy distribution and fallback rates, except for $\beta \gtrsim 8$,
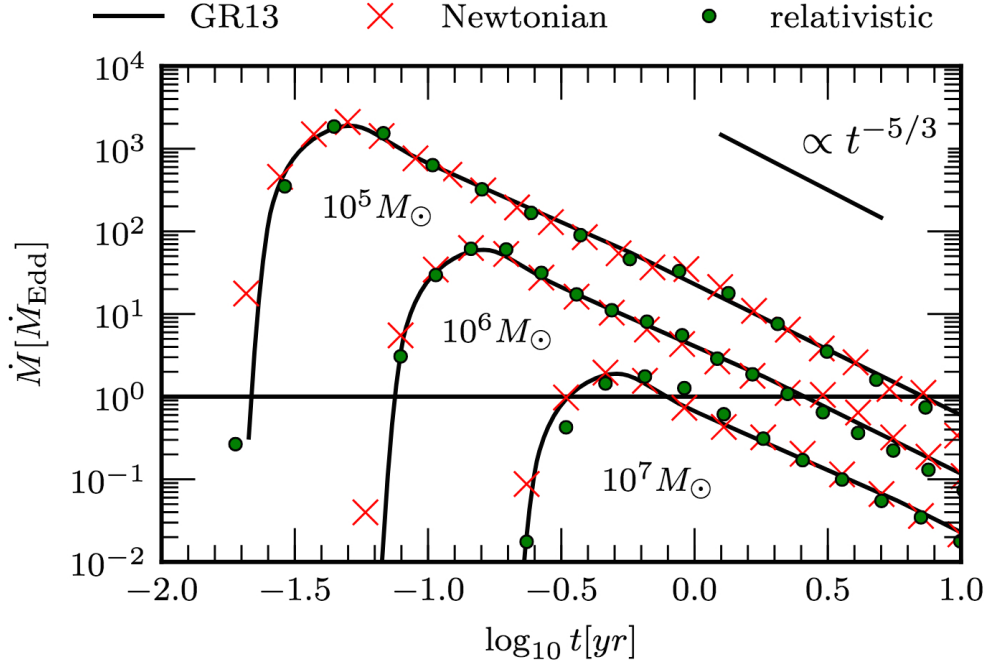
Figure 2.9: Fallback rates of solar-type star TDEs. Comparison between Newtonian (red cross) and Schwarzschild (green dot) cases for different MBH masses. At late times the curves follow $t^{-5/3}$. From Cheng & Bogdanović (2014).

where relativistic precession and tidal compression are relevant.

It is more uncertain how general relativity can affect the outcome of a TDE, i.e. how general relativistic precession controls circularization and disc formation or how the MBH spin can lead to precession of the TDE disc. Nonetheless, understanding these mechanisms is very important in the context of using TDEs as probes of MBH spins.

General relativity plays a central role during circularization processes. Apsidal precession leads to self-intersection of highly eccentric debris streams, which create shocks. As a consequence, there is large dissipation of energy, which drives the circularization process. However, relativistic nodal precession can work against circularization: debris streams are brought on different orbital planes, hindering self-crossings and thus circularization of debris (Guillochon & Ramirez-Ruiz, 2015).

Hayasaki et al. (2016) performed simulations with a post-Newtonian approach to model general relativistic effects, including leading order MBH spin corrections. Their simulations involve solar-type stars and a $10^6 M_\odot$ MBH. The star is on elliptical orbits with eccentricities $e = 0.7$, 0.8 and 0.9, $\beta = 1$ and 2. The orbits are in the equatorial plane and inclined ($\theta = 0°, 45°, 90°$). They showed that nodal precession for highly elliptical orbits out of the MBH spin plane can delay debris circularization. More recently, Liptai et al. (2019) made full general relativistic SPH simulations of TDEs involving solar-type stars and $10^6 M_\odot$ MBHs. The star is on elliptical orbits with eccentricity $e = 0.95$, $\beta = 1$ and 5, both in the equatorial plane and inclined ($\theta = 0°$, $30°$, $60°$, $89°$). They considered MBH with spin $a = 0$ and 0.99. Their work shows that stream-stream collisions caused by relativistic apsidal precession rapidly circularize the debris, whereas

for inclined trajectories nodal precession inhibits stream-stream collisions. However, this happens only for the first orbit, causing just a short delay in the disc formation, which is inclined with respect to the MBH equatorial plane. In addition, they also find that Lense-Thirring precession causes the remnant disc to precess about the MBH spin axis in both cases of radiatively efficient cooling, which produces a narrow ring disc, and no cooling, which produces an extended, thick torus. Finally, TDEs with high penetration factors are significantly more luminous and produce discs faster with respect to a lower β. In particular, Liptai et al. (2019) find that $\beta = 5$ TDEs have ~ 2 orders of magnitude higher energy injection rates than those with $\beta = 1$.

Another interesting work has been done by Gafton & Rosswog (2019), who performed relativistic TDE simulations of solar-type stars by spinning MBHs with spins between -0.99 and 0.99 and penetration factors between 0.5 and 11. They find that relativistic precession always causes thicker debris streams in the bound and unbound parts. They find that general relativity is particularly important in deep encounters, where strong precession modifies the morphology of the debris stream in ways not possible with Newtonian equations. Part of the debris can be launched on plunging orbits, reducing the fallback mass rate and the mass of the resulting accretion disc (up to 80% in deepest encounters with retrograde spin). In addition, Gafton & Rosswog (2019) find that the disruption can occur inside the marginally bound radius, in the case the angular momentum spread launches part of the debris on non-plunging orbits, and that relativistic effects are important also in partial disruptions. There is also a potential distinctive X-ray signature arising from the shock breakout due to multiple squeezings and bounces at pericenter.

CHAPTER 3

Hydrodynamical simulations

There are two fundamental ways for describing the physical governing equations: the Eulerian description and the Lagrangian description. Eulerian methods make use of geometric grids, which can be fixed or adaptive, and derivatives are calculated at fixed points in space, given by the grid. These codes formed the basis of computational fluid dynamics that started in the 1960s-1970s, and they are still nowadays the most widely used approach. Lagrangian methods, instead, calculate derivatives in a coordinate system attached to a moving fluid element. The two methods can be visualized as a boat following the river flow (Lagrangian method), rather than sitting on a river bank and watching the river flow pass by (Eulerian method).

In the Lagrangian method, since each grid node follows the material at the grid point, the relative movement of the connecting nodes can result in a deformation of a mesh cell, and the mass, momentum and energy are transported with the movement of the mesh cells. The mass within each cell is fixed, thus there is no mass flux between cells. However, this method can be difficult in practice whenever there is an extremely distorted mesh, for example, as the accuracy of the formulation and thus the solution will be severely affected (see e.g. Liu et al., 2004, for more details). On the other hand, in the Eulerian method, the grid nodes and cells are fixed in space, without changing when the material flows across the grid. Thus, large deformations do not affect the mesh itself and therefore we do not run in the same numerical problems that can be encountered in the Lagrangian method. This property makes the Eulerian method dominant in computational fluid dynamics, where the flow of the material dominates. Nevertheless, also this method has some disadvantages. For example, the grid should be large enough to cover the entire area to which the material can possibly flow. Due to computational efficiency, this can result in a coarser grid at the expenses of resolution and accuracy (see e.g. Liu et al., 2004, for more details).

Eulerian and Lagrangian methods have complementary features, which led to development of approaches that apply both descriptions, namely the Coupled Eulerian Lagrangian (Noh, 1963) and the Arbitrary Lagrange Eulerian (Hirt et al., 1974). For more details see for example Liu et al. (2004).

3.1 Phantom code

Numerical simulations have an important role in astrophysics, alongside analytic theory and observations, as they allow us to explore physical regimes in place of laboratory experiments.

We use a numerical code developed by Price et al. (2018) called Phantom. It is a fast, parallel, modular and low-memory code developed for astrophysical applications in 3D. Phantom is based on the SPH Lagrangian hydrodynamics modelling technique by Lucy (1977) and Gingold & Monaghan (1977) (see Benz, 1990; Monaghan, 1992, 2005; Rosswog, 2009; Springel, 2010; Price, 2012, for reviews), which is a grid-less technique in which fluid elements are represented by individual particles governed by hydrodynamic flow equations. SPH is a versatile technique and it has been used to model a wide range of astrophysical phenomena. In fact, Phantom is used to solve different astrophysical problems. It has been successfully employed to study TDEs (e.g. Coughlin & Nixon, 2015; Coughlin et al., 2016a,b; Bonnerot et al., 2016; Golightly et al., 2019a; Toscani et al., 2019; Sacchi & Lodato, 2019; Sacchi et al., 2020).

We now describe the equations behind SPH. In SPH the fluid is described by discrete mass elements called particles, whose properties are computed by suitable averages between neighbouring particles that lie within a smoothing region around it. Within this smoothing region, particles gain lower weight as they lie close to the edge. For instance, the density ρ at the position of particle a is given by

$$\rho(\mathbf{r}_a) = \sum_{b=1}^{N} m_b W(\mathbf{r}_a - \mathbf{r}_b, h), \qquad (3.1)$$

where W is the so-called smoothing kernel, typically a bell-shaped function with compact support, h is the smoothing length, which defines the size of the kernel, and N defines the number of neighbouring particles within the kernel.

Each particle has its own smoothing length h. It is defined such that each particle has approximately a constant number of neighbouring particles (Hernquist & Katz, 1989) and it can be given by

$$h(\mathbf{r}_a) = \eta \left(\frac{m_a}{\rho_a} \right)^{1/3}, \qquad (3.2)$$

where η should be chosen in the range between 1.2 and 1.5 (Rosswog, 2009, and references therein). Thus, SPH has the advantage that resolution follows density, that is high density regions have relatively small smoothing length, giving a higher spatial resolution. As a consequence, SPH is naturally an adaptive method (Rosswog, 2009; Lodato et al., 2020).

The equation of motion for each particle is derived from the Euler-Lagrange equations obtained from a variational principle formulation of fluid dynamics (Eckart, 1960). The Lagrangian of a perfect fluid is given by

$$L = \int \rho \left(\frac{v^2}{2} - u(\rho, s) \right) dV, \qquad (3.3)$$

where ρ is the density, v is the fluid velocity, u is the specific energy and s is the

specific entropy (Rosswog, 2009). This can be discretized as

$$L = \sum_b m_b \left(\frac{v_b^2}{2} - u(\rho_b, s_b) \right).$$
(3.4)

The discretized equations for the fluid can then be derived by applying the Euler-Lagrange equations

$$\frac{d}{dt} \left(\frac{\partial L}{\partial \mathbf{v}_a} \right) - \frac{\partial L}{\partial \mathbf{r}_a} = 0.$$
(3.5)

The first term of Eq. 3.5 gives the change of particle momentum $m_a \frac{d\mathbf{v}_a}{dt}$. The second term is like a potential: if self-gravity is considered, the term $-\sum_b m_b u_b$ becomes $-\sum_b m_b (u_b + \Phi_b)$, where Φ_b is the gravitational potential (Price, 2007; Rosswog, 2009). After some algebra and using the first principle of thermodynamics for a dissipationless fluid, we get the Euler-Lagrange equation of motion (see Rosswog, 2009; Price, 2012, for details)

$$\frac{d\mathbf{v}_a}{dt} = -\sum_b m_b \left[\frac{P_a}{\Omega_a \rho_a^2} \frac{\partial W_{ab}(h_a)}{\partial \mathbf{r}_a} + \frac{P_b}{\Omega_b \rho_b^2} \frac{\partial W_{ab}(h_b)}{\partial \mathbf{r}_a} \right],$$
(3.6)

where Ω is a term accounting for the gradient of the smoothing length (Price, 2012)

$$\Omega_a \equiv \left[1 - \frac{\partial h_a}{\partial \rho_a} \sum_b m_b \frac{\partial W_{ab}(h_a)}{\partial h_a} \right].$$
(3.7)

For a constant smoothing length, Eq. 3.6 becomes

$$\frac{d\mathbf{v}_a}{dt} = -\sum_b m_b \left(\frac{P_a}{\rho_a^2} + \frac{P_b}{\rho_b^2} \right) \nabla_a W_{ab},$$
(3.8)

which is the standard SPH expression (Monaghan, 1992; Rosswog, 2009; Price, 2012). It can be noted that total linear angular momentum is conserved exactly since

$$\frac{d}{dt} \sum_a m_a \mathbf{v}_a = \sum_a m_a \frac{d\mathbf{v}_a}{dt} = -\sum_a \sum_b m_a m_b \left(\frac{P_a}{\rho_a^2} + \frac{P_b}{\rho_b^2} \right) \nabla_a W_{ab} = 0$$
(3.9)

because the double summation gives zero due to antisymmetry in the kernel gradient (Price, 2012). Also the total angular momentum is conserved exactly since

$$\frac{d}{dt} \sum_a \mathbf{r}_a \times m_a \mathbf{v}_a = \sum_a m_a \left(\mathbf{r}_a \times \frac{d\mathbf{v}_a}{dt} \right)$$

$$= -\sum_a \sum_b m_a m_b \left(\frac{P_a}{\rho_a^2} + \frac{P_b}{\rho_b^2} \right) \mathbf{r}_a \times (\mathbf{r}_a - \mathbf{r}_b) \nabla_a W_{ab} = 0$$
(3.10)

because the last term gives zero due to antisymmetry in the double summation again (Price, 2012).

After finding the momentum equation, Eq. 3.8, we find the energy equation. The equation for internal energy can be derived by first considering the first law of thermodynamics, $dU = TdS - PdV$, where $\delta Q = TdS$ is the heat added to the system per unit volume and $\delta W = PdV$ is the work done by expansion and compression of the fluid. Using quantities per unit mass instead of per unit volume, so du instead of dU for example, the law can be rewritten as (Price, 2012)

$$du = Tds + \frac{P}{\rho^2}d\rho. \tag{3.11}$$

For constant entropy, the change in thermal energy is given by

$$\left.\frac{\partial u_b}{\partial \rho_b}\right|_s = \frac{P}{\rho^2}. \tag{3.12}$$

Thus, with no dissipation, we get from the last equation

$$\frac{du_a}{dt} = \frac{P_a}{\rho_a^2}\frac{d\rho_a}{dt}, \tag{3.13}$$

from which we can write the evolution of internal energy, by taking the time derivative of Eq. 3.1, as (Rosswog, 2009; Price, 2012)

$$\frac{du_a}{dt} = \frac{P_a}{\Omega_a\rho_a^2}\sum_b m_b(\mathbf{v}_a - \mathbf{v}_b) \cdot \nabla_a W_{ab}(h_a). \tag{3.14}$$

It can be noted that the total energy is also exactly conserved from the Lagrangian via the Hamiltonian (see Price, 2012, for details) as

$$\begin{aligned}
\frac{dE}{dt} &= \sum_a m_a \frac{de_a}{dt} \\
&= -\sum_a\sum_b m_a m_b \left[\frac{P_a}{\Omega_a\rho_a^2}\mathbf{v}_b \cdot \nabla_a W_{ab}(h_a) + \frac{P_b}{\Omega_b\rho_b^2}\mathbf{v}_a \cdot \nabla_a W_{ab}(h_b)\right] = 0
\end{aligned} \tag{3.15}$$

because again the double sum is zero due to the antisymmetry with respect to particle index. Now we have the full system of equations for ρ, $\mathbf{v}$ and u from Eqs. 3.1, 3.8 and 3.14.

The main computational expense common to any SPH code is finding neighbours. The most popular approach are tree methods (e.g. Barnes & Hut, 1986; Hernquist & Katz, 1989; Springel, 2005; Gafton & Rosswog, 2011). The tree search algorithm involves creating ordered trees according to the particle positions. Once the tree structure is created, it can be used efficiently to find the nearest neighbouring particles (Liu et al., 2004). Barnes & Hut (1986) introduced a scheme that involved a systematic division of the physical space and it has become the basis of most hierarchical tree codes. In their original work, the algorithm began with an empty cubical cell that had a size such that it could contain all the particles of the system. Then particles would be introduced one by one into this cell called root cell. The algorithm would then divide the cell into daughter cells whenever two particles fall into the same cell, which would

Figure 3.1: Example of kd-tree build in 2D. it represents the projection of particles in the xy plane from a polytrope test. Each level of the tree recursively splits the particle distribution in half, bisecting the longest axis at the center of mass until the number of particles in a given cell is $< N_{min}$. In this example $N_{min} = 100$ for clarity. Adapted from Price et al. (2018).
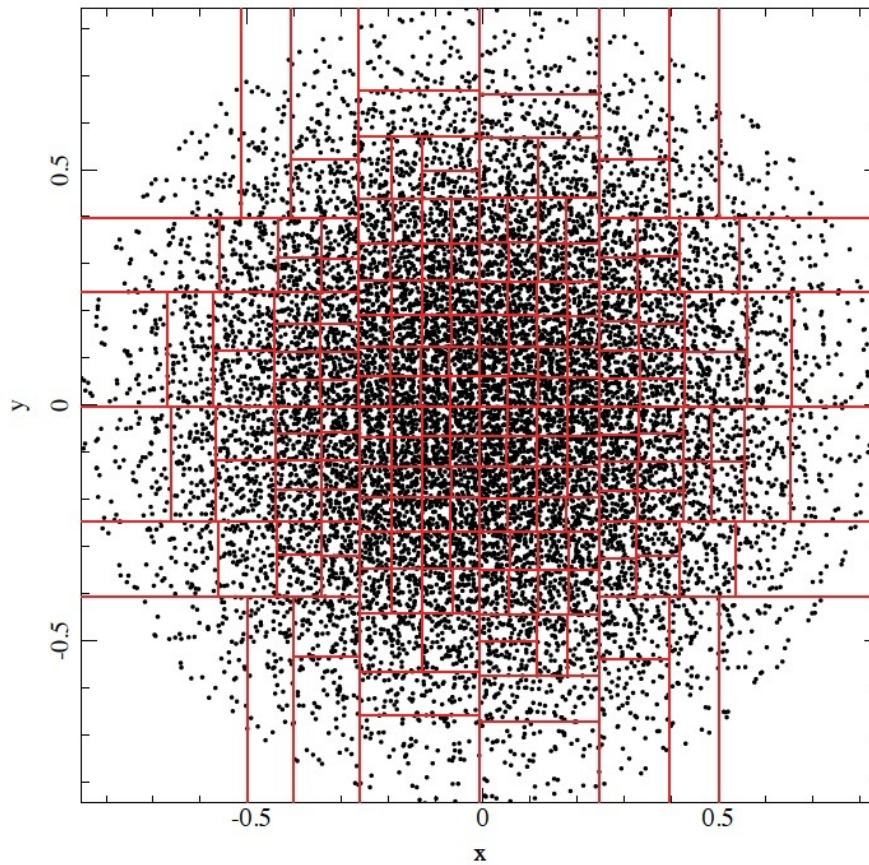
occur as soon as the second particle is introduced in the root cell. The daughter cells would have exactly half the length of the parent cell, in a way that viewed in 3D the cell is split into eight pieces. If two particles happen to be still in the same daughter cell after splitting, the cell is recursively divided in the same way, until particles are in different cells. This space division is not used as a grid but as a bookkeeping structure for the tree (see e.g. Pfalzner & Gibbon, 1996, for more details).

Since in Phantom self-gravity is implemented, the default option is using a kd-tree (Price et al., 2018). Self-gravity is essential in many astrophysical simulations, however, due to its long-range nature, it is generally the major computational burden in N-body simulations. The underlying idea is too collect particles in groups organised in a hierarchical fashion called nodes, as explained above. In this way computationally expensive tasks are performed on aggregate quantities of the groups rather than on individual particles. In addition, Phantom performs neighbour search for groups of particles (Price et al., 2018). The resulting positions of all neighbours are cached and used to check for neighbours for individual particles in the group. The implemented kd-tree algorithm follows Gafton & Rosswog (2011), which splits the particles recursively based on the center of mass and bisecting the longest axis at each level. An example of a kd-tree build is shown in Fig. 3.1. The tree build is refined until a single cell contains less than a minimum number of particles N_{min}. The cell containing $< N_{min}$ is called a leaf node, and by default $N_{min} = 10$. Finally, the neighbour search is performed once for each leaf node.

In Phantom code, linear and angular momentum are both conserved to round-off error (typically $\sim 10^{-16}$ in double precision), but exact conservation is violated when using individual particle timesteps or when using the kd-tree to compute gravitational forces. The magnitude of these quantities, as well as the total energy and its individual components, should be monitored at runtime. Considering individual timesteps, one should typically expect energy conservation to $\Delta E/E \sim 10^{-3}$, and linear and angular momentum conservation to $\Delta E/E \sim 10^{-6}$ with default code settings. Also, by default the code execution is aborted if conservation errors exceed 10% (Price et al., 2018).

The ideal gas equation of state relating the pressure P to the density ρ or internal energy u is

$$P = (\gamma - 1)\rho u, \tag{3.16}$$

where γ is the adiabatic index. The default equation of state in Phantom has the adiabatic index set to $\gamma = 5/3$. The sound speed c_s is given by γ, P and ρ by the following equation

$$c_s = \sqrt{\frac{\gamma P}{\rho}}, \tag{3.17}$$

while the pressure can be related to the gas temperature T by

$$P = \frac{\rho k_B T}{\mu m_H}, \tag{3.18}$$

where k_B is the Boltzmann's constant, μ is the mean molecular weight and m_H is

the mass of a hydrogen atom. Eq. 3.18 can be recast using Eq. 3.16, finding a relation between temperature and internal energy

$$T = \frac{\mu m_{\mathrm{H}}}{k_{\mathrm{B}}}(\gamma - 1)u. \tag{3.19}$$

In our simulations we evolve the gas using an isothermal equation of state instead of the standard adiabatic. In this case, the gas particles keep their initial thermal energies and physically represents an efficient cooling, since the thermal energy in excess is radiated away.

The timestepping algorithm used in Phantom to integrate the equations of motion is based on the Leapfrog method in Kick-Drift-Kick form or Verlet scheme (Verlet, 1967). The particle positions and velocities are evolved from time t^n to t^{n+1} according to

$$\mathbf{v}^{n+\frac{1}{2}} = \mathbf{v}^n + \frac{1}{2}\Delta t \mathbf{a}^n \tag{3.20}$$

$$\mathbf{r}^{n+1} = \mathbf{r}^n + \Delta t \mathbf{v}^{n+\frac{1}{2}} \tag{3.21}$$

$$\mathbf{a}^{n+1} = \mathbf{a}(\mathbf{r}^{n+1}) \tag{3.22}$$

$$\mathbf{v}^{n+1} = \mathbf{v}^{n+\frac{1}{2}} + \frac{1}{2}\Delta t \mathbf{a}^{n+1}. \tag{3.23}$$

In Phantom the approach is slightly different. Considering that in SPH there is the possibility to have velocity-dependent terms in the acceleration, it follows that Eq. 3.23 becomes implicit. Since these terms are not usually dominant over position-dependent terms, Phantom uses a first-order prediction of the velocity as follows (Price et al., 2018)

$$\mathbf{v}^{n+\frac{1}{2}} = \mathbf{v}^n + \frac{1}{2}\Delta t \mathbf{a}^n \tag{3.24}$$

$$\mathbf{r}^{n+1} = \mathbf{r}^n + \Delta t \mathbf{v}^{n+\frac{1}{2}} \tag{3.25}$$

$$\mathbf{v}^* = \mathbf{v}^{n+\frac{1}{2}} + \frac{1}{2}\Delta t \mathbf{a}^n \tag{3.26}$$

$$\mathbf{a}^{n+1} = \mathbf{a}(\mathbf{r}^{n+1}, \mathbf{v}^*) \tag{3.27}$$

$$\mathbf{v}^{n+1} = \mathbf{v}^* + \frac{1}{2}\Delta t[\mathbf{a}^{n+1} + \mathbf{a}^n]. \tag{3.28}$$

An error check is performed at the end of the step against a tolerance set by default to 10^{-2}. If the computed value doesn't satisfy the condition, the accelerations are recomputed by substituting $\mathbf{v}^*$ with $\mathbf{v}^{n+1}$ and iterating the last two passages till the condition is satisfied. In practice this happens rarely.

3.2 Setup and parameters

3.2.1 Simulations setup

It is essential in SPH to start with initial conditions that are as accurate as possible and that the initial particle setup is as close as possible to a configuration which would arise itself in a SPH simulation (e.g. Diehl et al., 2015). In Phantom the simplest method to initialise particles is to set them on a uniform Cartesian distribution. There are different arrangements (Fig. 3.2):

- cubic lattice, where particles are equally spaced in each direction, i.e. $\Delta x = \Delta y = \Delta z$;

- cubic close-packed lattice, where $\Delta y = \sqrt{3/4}\Delta x$ and $\Delta z = \sqrt{6}/3\Delta x$, repeated every 3 layers in z;

- hexagonal close-packed, as for close-packed but repeated every two layers in z;
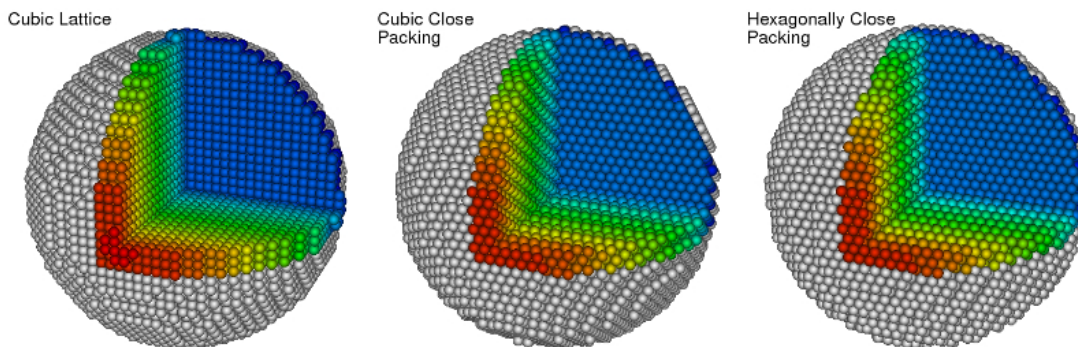
- uniform random.

Figure 3.2: Particle initial configurations. Colors change with z-axis simply to show depth. From Diehl et al. (2015).

While the cubic lattice is the simplest and most widely used particle arrangement, it is an unstable equilibrium configuration and has preferred directions along the xyz axes (Morris, 1996). On the other hand, cubic and hexagonal close-packed lattices are optimal and efficient ways to pack spheres of equal sizes, and they are stable against random perturbations (Monaghan, 1992).

To avoid geometrical effects, initial conditions are perturbed and then relaxed before calculation into a stable configuration by application of a dampening force proportional to and directed against particle velocities as

$$\mathbf{a}^a_{\text{ext,damp}} = -f_\text{d}\mathbf{v}, \tag{3.29}$$

where f_d is the damping parameter. This step is useful to produce low-noise initial conditions, however there is no way to guarantee the exact configuration into which particles will settle eventually.

In the case of setup of non-uniform density profiles, the procedure of stretch mapping is used to achieve a spatially adaptive resolution (Herant, 1994). In

this method a uniform lattice configuration is stretched in the radial direction, where each point of the lattice is multiplied by a radially varying scaling factor $q(r)$ in order to achieve the desired spherical symmetric distribution. Since this method basically distorts the initial lattice, it still includes and expands the bad characteristics of the lattice configuration. Thus, before starting a simulation, it is essential to relax the resulting configuration into a more isotropic equilibrium state.

In Phantom the spherical distribution procedure is the most commonly used (e.g Fryer et al., 2007; Rosswog & Price, 2007), and in addition the method is generalised for any density profile along one coordinate direction. Once the stretch mapping is done, in the case of a star, relaxation of the particle distribution into equilibrium is done with the standard approach of adding an external acceleration (e.g. Gingold & Monaghan, 1977) as in Eq. 3.29 such that a percentage of the kinetic energy is removed at each time step. The damping parameter is defined by the user and the value used in this work is $f_\mathrm{d} = 0.03$, such that a small fraction of the kinetic energy is removed over a Courant timescale (Price et al., 2018). The Courant timescale is defined by the Courant-Friedrichs-Lewy (CFL) condition for stability, which requires that the time interval employed should be no greater than that required for a sound wave to cross a spatial cell.

To resume, in Phantom it is implemented a general method for setting up stellar density profiles, which can be based on analytical functions such as polytropes or tabulated data files, e.g. from stellar evolution codes. A uniform density particle sphere is set up and then the density profile is stretched. It is taken care that the thermal energy of the particles is such that the pressure gradient is in hydrostatic equilibrium with self-gravity of the star, according to the chosen equation of state. The star is then relaxed into equilibrium over several dynamical times (Price et al., 2018).

3.2.2 Stellar model

Here we are going to introduce the Lane-Emden equation, which describes polytropes in hydrostatic equilibrium to be used as simple star models. The polytropic stellar model can be defined as the one in which the equation of state is

$$P = K\rho^\gamma, \tag{3.30}$$

where K is a constant, $\gamma = 1 + 1/n$ and n is the polytropic index. By combining the equation of state Eq. 3.30 with the equation of hydrostatic equilibrium

$$\frac{dP}{dr} = -\frac{GM(r)}{r^2}\rho(r) \tag{3.31}$$

we get

$$\frac{1}{r^2}\frac{d}{dr}\left(\frac{r^2}{\rho}\frac{dP}{dr}\right) = -4\pi G\rho \tag{3.32}$$

and the Lane-Emden equation

$$\frac{(n+1)P_c}{4\pi G\rho_c^2}\frac{1}{r^2}\frac{d}{dr}\left(r^2\frac{d\theta}{dr}\right) = -\theta^n, \tag{3.33}$$

where θ is a dimensionless variable defined as $\rho(r) = \rho_c\theta^n(r)$ ($\rho_c = \rho(r = 0)$), P_c is the central pressure, $P_c = K\rho_c^{1+1/n}$. The power law for pressure is $P(r) = P_c\theta^{1+n}(r)$ (see e.g. Hansen et al., 2004, for details). By introducing a new dimensionless radial coordinate ξ in $r = r_n\xi$, where $r_n = (n+1)P_c/(4\pi G\rho_c^2)$, we get the dimensionless Lane-Emden equation

$$\frac{1}{\xi^2}\frac{d}{d\xi}\left(\xi^2\frac{d\theta}{d\xi}\right) = -\theta^n. \tag{3.34}$$

The solutions found by solving this equation for a chosen n are models called polytropes of index n, and a star which obeys such equation of state is called a polytropic star. In Phantom the creation of a polytropic star is achieved by first placing particles on a close-packed sphere, which is then stretched to achieve the correct polytropic density profile, which is obtained by numerical integration of the Lane-Emden equation.

There are different cases where the equation of state in a star can be approximated by a polytropic equation of state. One case is a star in convective equilibrium. The ascent and descent of the convective cells are typically assumed to be part of an adiabatic process. In such case, the equation of state for an ideal monoatomic gas is $P = K\rho^\gamma$, with $\gamma = 5/3$ (since $\gamma = (n+1)/n$, $n = 1.5$). Other cases where one can apply the polytropic equation of state are stellar regions where the pressure is dominated by a completely degenerate electron gas, that is in the core of evolved stars and in white dwarfs. The equation of state with $n = 3$ is usually used to model main-sequence stars as the Sun (Hansen et al., 2004) and in the case of relativistic degenerate matter. See LeBlanc (2010) for more details. In general, the $n = 3/2$ less concentrated polytropes are used to represent lower main sequence stars, while $n = 3$ models are used to represent highly concentrated stars. In addition, going from a polytrope with $n = 3$ to $n = 3/2$ means going from a radiative star to a convective one.

Main sequence stars like the Sun are usually described by a $n = 3$ polytrope. A comparison between the $n = 3$ polytrope and results from a zero age main sequence model with same mass and radius (Hansen et al., 2004) show that the polytrope works well for the inner regions where density and temperature are high. For outer regions, a $n = 3/2$ polytrope suits more because of convection. However, this constitutes only about 0.6% of the mass of the star, so most of the star has a structure close to that of an $n = 3$ polytrope.

If a star is massive enough ($> 1.5 M_\odot$), it will go into the carbon-nitrogen-oxygen (CNO) regime, instead of the proton-proton chain. In this case, the CNO regime releases energy in a smaller region of the star than the proton-proton chain, so it drives convection in the stellar center. For massive stars, the surface gas is hotter, the hydrogen mostly ionised and it is the radiation that carries the power (see e.g. Hansen et al., 2004, for more details on stellar structure).

In our simulations, we decided to model the stars with a $n = 1.5$ index (or $\gamma = 5/3$). In TDE simulations it is common to set up solar-like stars, that is stars with $1M_\odot$ and $1R_\odot$ as $n = 1.5$ polytropes (e.g. Evans & Kochanek, 1989; Ayal et al., 2000; Hayasaki et al., 2013; Coughlin & Nixon, 2015; Bonnerot et al., 2016), since they are structurally similar to low-mass main sequence stars. In order to be able to compare our results to other studies, our solar-like star was modelled with such polytrope. We decided to apply the same polytrope also for the S-like

star, since they are massive ($\sim 8 - 14 M_{\odot}$; Habibi et al. (2017)) main sequence stars. The polytrope is most probably not the most suitable for this kind of star, as it should have only a small convective core, as discussed above. Thus, the choice was supported mainly for comparison reasons with our solar-like star TDE simulations. A more detailed analysis on more realistic stars (for example with the MESA code; Paxton et al. (2010)) was thought to be more appropriate for a future work, which would expand the work done here.

3.2.3 Gravitational potential

During the simulation, the particles representing the gas evolve according to the gravity of the MBH which is modelled with the generalised Newtonian gravitational potential given by Tejeda & Rosswog (2013)

$$\Phi_{\mathrm{G}}(r, \dot{r}, \dot{\phi}) = -\frac{GM_{\mathrm{BH}}}{r} - \left(\frac{2r_{\mathrm{g}}}{r - 2r_{\mathrm{g}}}\right)\left[\left(\frac{r - r_{\mathrm{g}}}{r - 2r_{\mathrm{g}}}\right)\dot{r}^2 + \frac{r^2(\dot{\theta}^2 + \sin^2\theta\dot{\phi}^2)}{2}\right], \quad (3.35)$$

where $r_{\mathrm{g}} = GM_{\mathrm{BH}}/c^2$ is the gravitational radius, θ the polar angle and ϕ is the azimuthal angle in spherical geometry. This potential is derived from the geodesic motion of test particles in the Schwarzschild spacetime. Pseudo-newtonian potentials (e.g. Paczyńsky & Wiita, 1980; Nowak & Wagoner, 1991) have been proposed to capture more carefully some properties of the relativistic solutions to the accretion disc and they have been widely used in accretion studies onto Schwarzschild BHs to reproduce general relativistic effects within a Newtonian framework (e.g. Chakrabarti & Titarchuk, 1995; Chen et al., 2008; Rosswog et al., 2009b). However, not all specific general relativistic features are well reproduced, thus reducing the range of their applicability. For instance, the Paczyńsky and Wiita pseudo-Newtonian potential

$$\Phi = -\frac{GM_{BH}}{r - 2r_g} \quad (3.36)$$

correctly reproduces the positions of the innermost stable circular orbit, $r_{ISCO} = 6r_g$, and the marginally bound circular orbit, $r_b = 4r_g$. It reasonably reproduces quantities such as angular momentum of circular orbits, i.e. with a percentage error $\leq 6\%$, however other quantities are not accurately reproduced, for example orbital frequency has a percentage error $\leq 50\%$ (Tejeda & Rosswog, 2013). As dsicussed by Tejeda & Rosswog (2013), another common problem when using pseudo-Newtonian potentials is that they accurately reproduce circular orbits, but not necessarily more general trajectories. Regarding this issue, the generalized Newtonian potential by Tejeda & Rosswog (2013) has the feature of accurately describing the motion of test particles in Schwarzschild spacetime. From Eq. 3.35, we can see that the potential includes the typical Newtonian term which scales as $1/r$. In addition, it includes in the second term a dependence on the velocity of the test particle, which can be interpreted as an additional contribution due to the kinetic energy being also gravitationally attracted by the central mass. This potential accurately models several relativistic features of the Schwarzschild spacetime, reproducing in particular the exact location of the marginally stable, marginally bound and photon circular orbits, as well as the ex-

act radial dependence of the binding energy and angular momentum. Moreover, this potential exactly reproduces the time evolution of parabolic-like trajectories and the pericenter advance of elliptical trajectories.

An example of a tidal disruption of a solar-type star with $M_* = 1\ M_\odot$, $R_* = 1\ R_\odot$ on a parabolic trajectory by a $M_{\mathrm{BH}} = 10^6\ M_\odot$ MBH is shown in Fig. 3.3. The figure shows the comparison of the SPH simulation by Tejeda & Rosswog (2013) run for four different potentials, including the generalised Newtonian potential, to the exact trajectory in Schwarzschild spacetime.

The generalized Newtonian potential has been used also by Bonnerot et al. (2016) in a similar setup, with the difference that they explored tidal disruption of stars on eccentric orbits with penetration factor $\beta = 1$ and 5 and eccentricities $e = 0.8$ and 0.95.
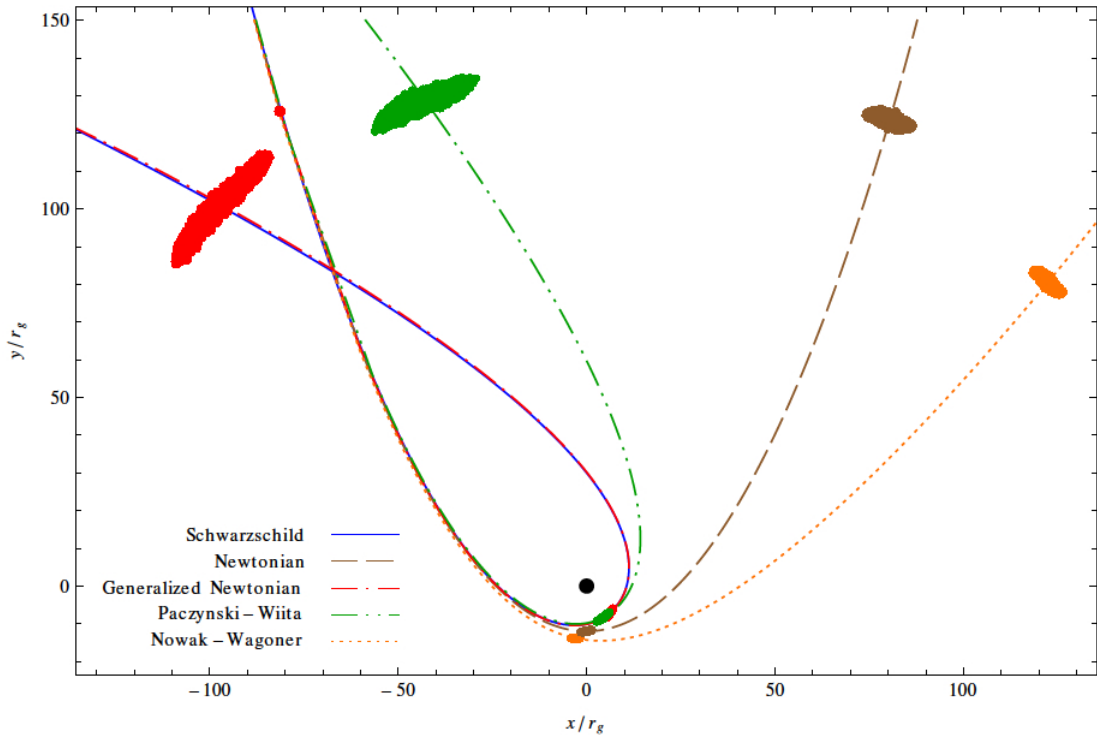
Figure 3.3: Comparison of the same TDE simulation with four different potentials. The figure shows the trajectory followed by the center of mass of the star in each case, projected onto the orbital plane. The solid blue line is the reference exact geodesic trajectory of a test particle in Schwarzschild spacetime. Adapted from Tejeda & Rosswog (2013).

A test particle evolving under this generalized Newtonian potential conserves the specific orbital energy and angular momentum, which are given by

$$\epsilon = \frac{1}{2}\left[\frac{r^2\dot{r}^2}{(r-2r_{\mathrm{g}})^2} + \frac{r^3(\dot{\theta}^2 + \sin^2\theta\,\dot{\phi}^2)}{r-2r_{\mathrm{g}}}\right] - \frac{GM_{\mathrm{BH}}}{r}, \tag{3.37}$$

$$l = \frac{r^3\sqrt{\dot{\theta}^2 + \sin^2\theta\,\dot{\phi}^2}}{r - 2r_{\mathrm{g}}}. \tag{3.38}$$

The generalised Newtonian potential is implemented in Phantom and the acceleration components are given by

$$\ddot{x}^i = -\frac{GMx^i}{r^3}\left(1 - \frac{2r_{\mathrm{g}}}{r}\right)^2 + \frac{2r_{\mathrm{g}}\dot{x}^i}{r^2(r - 2r_{\mathrm{g}})}\sum_j x^j\dot{x}^j - \frac{3r_{\mathrm{g}}x^i}{r^5}\sum_j\left(\sum_{kl}\epsilon_{kjl}x^k\dot{x}^l\right)^2.$$

$$(3.39)$$

3.2.4 Stellar and orbital parameters

Since we want to study the dynamics of TDEs occurring in a nuclear environment like our GC, we choose a MBH and stars which are representative for such environment. The mass of the MBH is set to the mass of Sgr A*, $M_{\mathrm{BH}} = 4.3 \cdot 10^6 M_\odot$ (Gillessen et al., 2009). We define an accretion radius, i.e. a distance within which we remove any particle from the simulation due to accretion to the MBH, and we set this distance to be at the innermost stable circular orbit for a non-spinning BH, $r_{\mathrm{ISCO}} = 6r_g$.

Most TDE simulations found in the literature study the disruption of solar type stars, i.e. stars with $M_* = 1M_\odot$ and $R_* = 1R_\odot$ (e.g. Laguna et al., 1993; Ayal et al., 2000; Coughlin & Nixon, 2015). For comparison purposes, we choose this kind of star for our simulations and, in addition, we choose a star with $M_* = 10M_\odot$ and $R_* = 5R_\odot$: this choice comes from the observation that the group of stars orbiting around Sgr A* within a distance of < 0.04 pc are S stars, which are main sequence massive stars. According to the recent study made by Habibi et al. (2017), high resolution spectroscopy infers that the spectral type of these stars is B0-B3V, masses range between 8 and 14 $M_\odot$, radii range between 4 and 6 $R_\odot$, and ages are < 15 Myrs.

In order to explore the stellar disruption evolution of the two chosen types of stars, we ran simulations over a range of orbital parameters. Considering that it is observed that S stars have eccentricities in the range from ~ 0.4 to 0.95 (Eisenhauer et al., 2005; Parsa et al., 2017), we performed simulations for such orbits. We noticed that below $e = 0.5$ our simulations do not show dynamically interesting TDEs for this study, therefore we opted for $0.5 \leq e \leq 0.99$. We added the high eccentricity $e = 0.99$ orbit to include stars scattered from large distances (on nearly parabolic orbits).

To study the effects of the strength of a tidal disruption we chose different penetration factors β (Eq. 2.2), in particular we chose orbits with β between 1 and 5. In order for a complete disruption to occur outside the MBH, r_{p} of the star's orbit must be $\leq r_{\mathrm{t}}$, and r_{t} must be greater than the MBH event horizon, $2r_{\mathrm{g}}$. Fig. 3.4, panel a) shows how orbits with fixed β change with eccentricities, and panel b) shows how orbits with fixes e change with different β. Each orbit represents the trajectory in one period of the center of mass of a star in the generalised Newtonian potential described by Eq. 3.35. The MBH r_{ISCO} is represented by the filled black circle, and r_{t} distance is given by the dashed line.

The list of the 37 performed simulations is given in Table 3.1. Each simulation is labelled with the letter S or s, denoting a $M_* = 10$ $M_\odot$, $R_* = 5$ $R_\odot$ star (S star-like) and a $M_* = 1$ $M_\odot$, $R_* = 1$ $R_\odot$ star (solar-like), respectively, a number denoting the β value, and a number after the dot denoting the eccentricity. So, for example, S1.6 is the simulation corresponding to the model of a S star on an

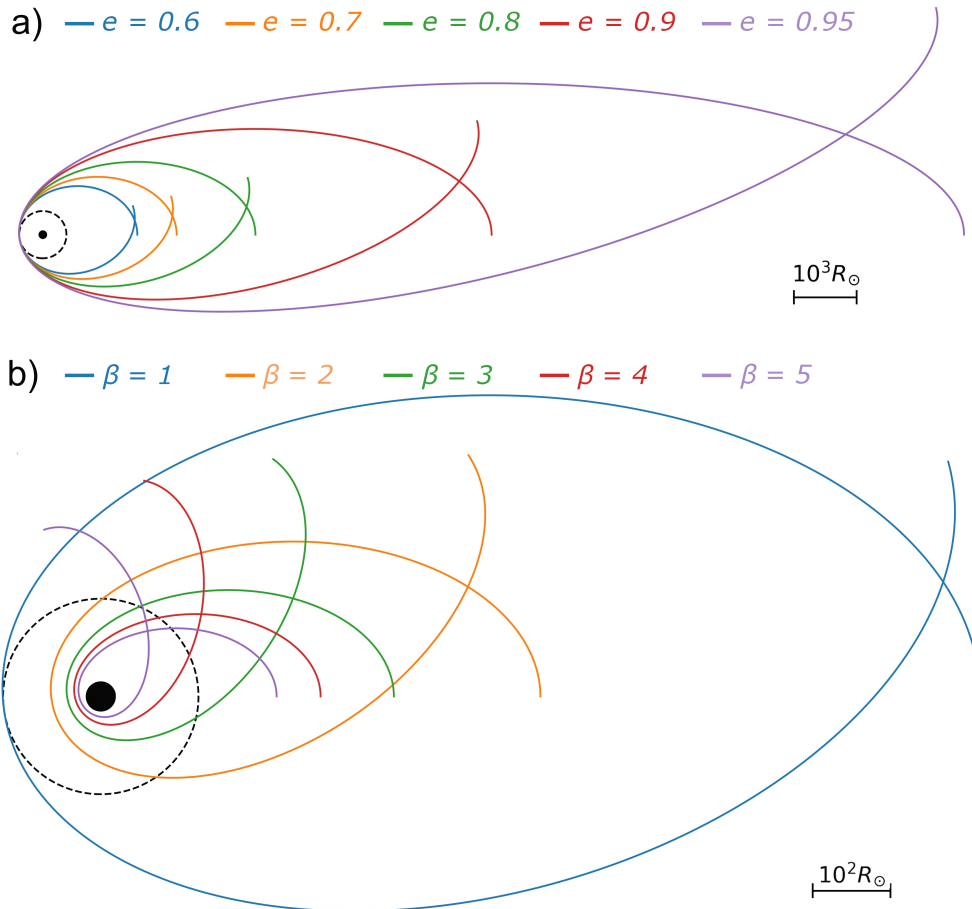Figure 3.4: Orbits with eccentricities ranging from $e = 0.6$ to 0.95 with fixed $\beta = 1$ (a), and orbit with penetration factor ranging from $\beta = 1$ to 5 with fixed $e = 0.8$ (b). Each orbit is the trajectory of the center of mass of a star in the generalised Newtonian potential (Eq. 3.35) in one period. The filled circle represents the r_{ISCO}, while the dashed circle represents r_{t}.

initial orbit with penetration factor $\beta = 1$ and eccentricity $e = 0.6$.

The simulations performed for this work were run on the HPC cluster offered by Arctur d.o.o.. The cluster consists in different nodes, each with 28 cores @ 2.6 GHz, which allowed us to run simulations within a reasonable time.

Simulation data in this work are visualised using the SPLASH tool (Price, 2007). Fig. 3.5 shows a sequence of snapshots of model S1.8.
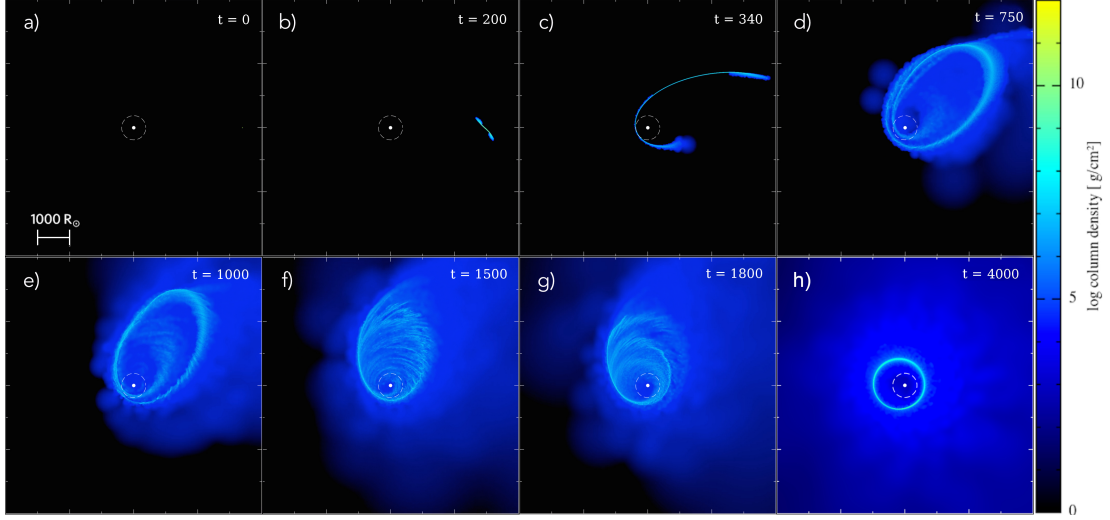
Figure 3.5: Sequence of snapshots of model S1.8. The MBH is represented by the full white circle, which has radius equal to r_{ISCO}, while the dashed white line represents the tidal radius r_t. In panel a) the star is in its initial position r_a and orbits the MBH on an anticlockwise trajectory. In panel b) the star has been disrupted and the debris formed two tails, which will stretch and fallback (panel c)). In panels d)-g) the debris is going through circularisation processes, which result in the formation of a disc (panel h).

Table 3.1: List of simulations. For each model the respective penetration factor β, eccentricity e, the pericenter distance r_p, the apocenter distance r_a and the velocity at apocenter v_a are reported. The model name includes the type of star, the penetration factor and a number related to the eccentricity. A star with 10 $M_\odot$, 5 $R_\odot$ is dubbed as S (S star like), while a star with 1 $M_\odot$, 1 $R_\odot$ is dubbed as s (solar like). For instance, S1.6 is a model with an S star, $\beta = 1$ and $e = 0.6$.

Model	Star	β	e	e_crit	r_p	r_a	v_a
Units					$R_\odot(r_g)$	$R_\odot(r_g)$	m/s
S1.6	S	1	0.60	0.974	377.4 (41.4)	1509.6 (165.4)	$1.5 \cdot 10^7$
S1.7	S	1	0.70	0.974	377.4 (41.4)	2138.6 (234.4)	$1.1 \cdot 10^7$
S1.8	S	1	0.80	0.974	377.4 (41.4)	3396.5 (372.3)	$7.1 \cdot 10^6$
S1.9	S	1	0.90	0.974	377.4 (41.4)	7170.5 (785.9)	$3.5 \cdot 10^6$
S1.95	S	1	0.95	0.974	377.4 (41.4)	14718.3 (1613.1)	$1.7 \cdot 10^6$
S1.99	S	1	0.99	0.974	377.4 (41.4)	75101.0 (8231.1)	$3.4 \cdot 10^5$
S2.5	S	2	0.50	0.987	188.7 (20.7)	566.1 (62.0)	$2.8 \cdot 10^7$
S2.6	S	2	0.60	0.987	188.7 (20.7)	754.8 (82.7)	$2.1 \cdot 10^7$
S2.7	S	2	0.70	0.987	188.7 (20.7)	1069.3 (11.7)	$1.6 \cdot 10^7$
S2.8	S	2	0.80	0.987	188.7 (20.7)	1698.3 (18.6)	$1.0 \cdot 10^7$
S2.9	S	2	0.90	0.987	188.7 (20.7)	3585.2 (39.3)	$5.0 \cdot 10^6$
S2.95	S	2	0.95	0.987	188.7 (20.7)	7359.1 (80.7)	$2.5 \cdot 10^6$
S3.6	S	3	0.60	0.991	125.8 (13.8)	503.2 (55.2)	$2.7 \cdot 10^7$
S3.7	S	3	0.70	0.991	125.8 (13.8)	712.9 (78.1)	$2.0 \cdot 10^7$
S3.8	S	3	0.80	0.991	125.8 (13.8)	1132.2 (124.1)	$1.3 \cdot 10^7$
S3.9	S	3	0.90	0.991	125.8 (13.8)	2390.2 (262.0)	$6.3 \cdot 10^6$
S3.95	S	3	0.95	0.991	125.8 (13.8)	4906.1 (537.7)	$3.1 \cdot 10^6$
S4.7	S	4	0.70	0.993	94.3 (10.3)	534.6 (58.6)	$2.3 \cdot 10^7$
S4.8	S	4	0.80	0.993	94.3 (10.3)	849.1 (93.1)	$1.5 \cdot 10^7$
S4.9	S	4	0.90	0.993	94.3 (10.3)	1792.6 (196.5)	$7.5 \cdot 10^6$
S4.95	S	4	0.95	0.993	94.3 (10.3)	3679.6 (403.3)	$3.7 \cdot 10^6$
S5.7	S	5	0.70	0.995	75.5 (8.3)	427.7 (46.9)	$2.6 \cdot 10^7$
S5.8	S	5	0.80	0.995	75.5 (8.3)	679.3 (74.5)	$1.7 \cdot 10^7$
S5.9	S	5	0.90	0.995	75.5 (8.3)	1434.1 (157.2)	$8.6 \cdot 10^6$
S5.95	S	5	0.95	0.995	75.5 (8.3)	2943.7 (322.6)	$4.3 \cdot 10^6$
s1.6	s	1	0.60	0.988	162.6 (17.8)	650.5 (71.3)	$2.3 \cdot 10^7$
s1.7	s	1	0.70	0.988	162.6 (17.8)	921.5 (101.0)	$1.7 \cdot 10^7$
s1.8	s	1	0.80	0.988	162.6 (17.8)	1463.5 (160.4)	$1.1 \cdot 10^7$
s1.9	s	1	0.90	0.988	162.6 (17.8)	3089.7 (338.6)	$5.4 \cdot 10^6$
s1.95	s	1	0.95	0.988	162.6 (17.8)	6341.9 (695.1)	$2.7 \cdot 10^6$
s1.99	s	1	0.99	0.988	162.6 (17.8)	32360.1 (35446.7)	$5.3 \cdot 10^5$
s2.5	s	2	0.5	0.994	81.3 (8.9)	243.9 (26.7)	$4.3 \cdot 10^7$
s2.6	s	2	0.60	0.994	81.3 (8.9)	325.2 (35.7)	$3.4 \cdot 10^7$
s2.7	s	2	0.70	0.994	81.3 (8.9)	460.7 (50.5)	$2.5 \cdot 10^7$
s2.8	s	2	0.80	0.994	81.3 (8.9)	731.8 (80.2)	$1.7 \cdot 10^7$
s2.9	s	2	0.90	0.994	81.3 (8.9)	1544.8 (169.3)	$8.2 \cdot 10^6$
s2.95	s	2	0.95	0.994	81.3 (8.9)	3171.0 (347.5)	$4.1 \cdot 10^6$

CHAPTER 4

Results and discussion

4.1 Debris at pericenter and falling back

4.1.1 Specific energy distribution

Let us assume as initial condition that the star at a large distance from the MBH is in hydrostatic equilibrium. We consider each fluid element of the star to initially move in a Keplerian orbit, each one with its own energy, and thus each with an eccentricity close to that of the center of mass of the star. As the star approaches the MBH the orbits get squeezed, resulting in a perturbed hydrostatic equilibrium. The energy inside the star is redistributed and the specific energy distribution will be wider, with a spread on energy (Stone et al., 2013)

$$\Delta\epsilon \sim \frac{GM_{\mathrm{BH}}R_*}{r_{\mathrm{t}}^2}. \tag{4.1}$$

After the close approach to the MBH, the fluid elements move on orbits according to their new specific energy with a distribution ranging over

$$-\Delta\epsilon + \epsilon_{\mathrm{orb}} \leq \epsilon \leq \Delta + \epsilon_{\mathrm{orb}}, \tag{4.2}$$

where ϵ_{orb} is the specific orbital energy of the stellar center of mass approaching the MBH. For eccentric orbits, ϵ_{orb} is given by

$$\epsilon_{\mathrm{orb}} = \frac{GM_{\mathrm{BH}}}{2r_{\mathrm{t}}}\beta(1-e). \tag{4.3}$$

Since we are interested in fluid elements which will form an accretion disc, we consider those with negative energy. These will return close to r_{p} after a Keplerian period

$$T = \frac{2\pi GM_{\mathrm{BH}}}{(-2\epsilon)^{2/3}}. \tag{4.4}$$

The most tightly bound debris and the most loosely bound debris have periods $t_{\min}$ and $t_{\max}$, respectively, which can be calculated as (Hayasaki et al., 2013)

$$t_{\min} = \frac{\pi}{\sqrt{2}}\frac{t_{\mathrm{dyn}}}{\beta^{3/2}(1-e)^{3/2}} \tag{4.5}$$

$$t_{\mathrm{max}} = \frac{\pi}{\sqrt{2}} \left[\frac{\beta(1-e)}{2} \left(\frac{M_*}{M_{\mathrm{BH}}} \right)^{1/3} \right]^{-3/2} \qquad (4.6)$$

where t_{dyn} is the dynamical time given by $\sqrt{R_*^3/(GM_*)}$, and t_{max} is valid for $e < e_{\mathrm{crit}}$, where e_{crit} is given by Eq. 2.17 and is the eccentricity below which all the debris remains bound after disruption (among our models only S1.99 and s1.99 have $e > e_{\mathrm{crit}}$; see Tab. 3.1). Thus, the duration time of mass fallback of eccentric TDEs with $e < e_{\mathrm{crit}}$ can be predicted to be finite and it is given by $\Delta t = t_{\mathrm{max}} - t_{\mathrm{min}}$. We calculate t_{min} and t_{max} analytically using Eq. 4.5 and Eq. 4.6, and we find discrepancies with values obtained from our simulations. For example, Eq. 4.5 and Eq. 4.6 give for S1.6 $t_{\mathrm{min}} = 0.002$ yr and $t_{\mathrm{max}} = 0.005$ yr, and for S3.8 $t_{\mathrm{min}} = 0.001$ yr and $t_{\mathrm{max}} = 0.003$ yr. The t_{min} values do not agree with values found from simulations (see Fig. 4.6, right panels), where we find for S1.6 $t_{\mathrm{min}} \approx 0.004$ yr and $t_{\mathrm{max}} \approx 0.005$ yr, and for S3.8 $t_{\mathrm{min}} \approx 0.002$ yr and $t_{\mathrm{max}} \approx 0.003$ yr. This is due to the fact that they are evaluated taking into account the energy spread $\Delta\epsilon$, which is fixed by Eq. 4.1. This discrepancy has been noted previously by Hayasaki et al. (2013). The discrepancy is due to the fact that they are estimated based on Newtonian potential, which has smaller spread in energy than in the simulations.

We calculate $\mathrm{d}m/\mathrm{d}\epsilon$ directly from our simulations, where the specific energy is given by Eq. 3.37. Fig. 4.3, Fig. 4.4 and Fig. 4.5 show the specific energy distributions (left panels), calculated from the stellar debris at the second passage to pericenter, before self-crossings and circularisation mechanisms begin to act. In general, the specific energy distribution can show two features: a peak around the central value and two lateral peaks called wings. The wings are related to the formation of the tails after the first passage at r_{p} (see panel b) in Fig. 3.5). From Fig. 4.3, Fig. 4.4 and Fig. 4.5, it is evident that the tails tend to disappear for high β and high e. In particular, in models S5.7, S5.8, S5.9 and S5.95, the wings in the specific energy distribution are not visible at all and instead there is a single peak distribution (Fig. 4.4, bottom row). It can also be noticed that with increasing β the energy spread $\Delta\epsilon$ weakly depends on β (Fig. 4.1), in agreement with Stone et al. (2013), Hayasaki et al. (2013) and Guillochon & Ramirez-Ruiz (2013). This is related to the fact that for higher β, the star is subject to stronger tidal force as it resides in a deeper potential well ($r_{\mathrm{p}} < r_{\mathrm{t}}$) than models with $\beta = 1$. Hence, after the first passage at r_{p}, the stellar debris cannot extend the two tails, resulting in a more compact clump and the tails fall back almost together and with similar energies (Fig. 4.2). For $\beta = 1$, in particular in models S1.9, S1.95, S1.99, s1.9, s1.95 and s1.99, there is a small peak around the central value of the distribution, which flattens as e decreases (top panel in Fig. 4.3). The peak is formed by mass congregation due to self-gravity. After seconds passage to pericenter, the distributions show high variability due to circularisation processes and disc formation during fallback.

In order to see how the time evolution of the energy distribution changes with β, in Fig. 4.6 we compare, as example, S1.6 (top panel) to S3.8 (bottom panel). We plot distributions at different times of the debris evolution: the star's initial position at r_a (blue), the first passage at r_{p} (orange), the formation of two debris
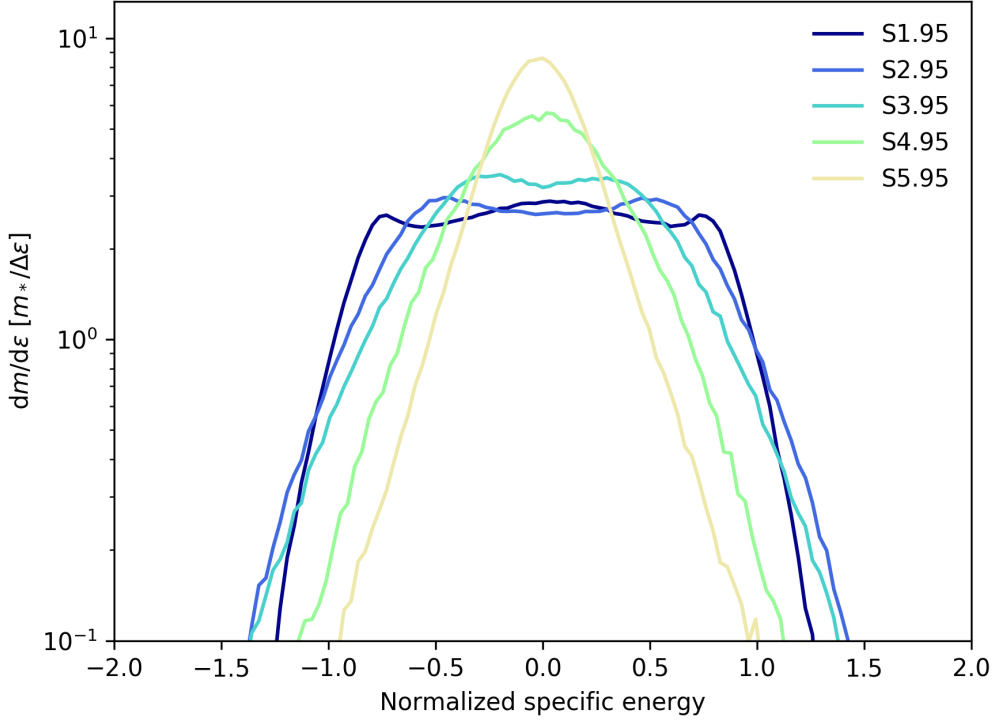
Figure 4.1: Plot of specific energy distribution of models S1.95, S2.95, S3.95, S4.95 and S5.95. The distributions are normalised with respect to the energy, in order to compare the energy spread. The colours correspond to different penetration factors β.

tails (green), the stretching and falling back of the most bound debris tail (red), and the second passage to r_{p} (purple). At higher β we can observe a shift of the specific energy distribution at later times with respect to the distribution at r_a and first passage to r_{p}: while at $\beta = 1$ all the distributions are symmetric with respect to the central value over time, as β is increased there is a shift towards higher energies of the distribution at later times. The shift may be due to a stronger torque felt by the star with higher β.

4.1.2 Mass return rate distribution

In order to estimate the mass return rate $\mathrm{d}m/\mathrm{d}t$, we follow the method used in e.g. Hayasaki et al. (2013). We assume that fluid elements with negative energies returning to pericenter, lose energy and angular momentum on a viscous timescale $<< T$. The mass return rate is then evaluated from the specific energy distribution $\mathrm{d}m/\mathrm{d}\epsilon$ and the specific energy derivative with respect to time $\mathrm{d}\epsilon/\mathrm{d}t$, which is calculated from Kepler's third law. Thus, the mass return rate is given by Eq. 2.26.

Fig. 4.3, Fig. 4.4 and Fig. 4.5 (right panels) show the mass return rates. After the star is disrupted at first passage at r_{p}, the debris forms two tails, which stretch when falling back (Fig. 3.5, panel b) and c)). The tail which falls back first, with lower energy, translates to the rising part of the mass return rate distribution. The stretched debris which follows the leading tail translates to the $t^{-5/3}$ power law curve of the mass return rate distribution, and it becomes longer as eccentricity increases with fixed β, the most noticeable examples being models
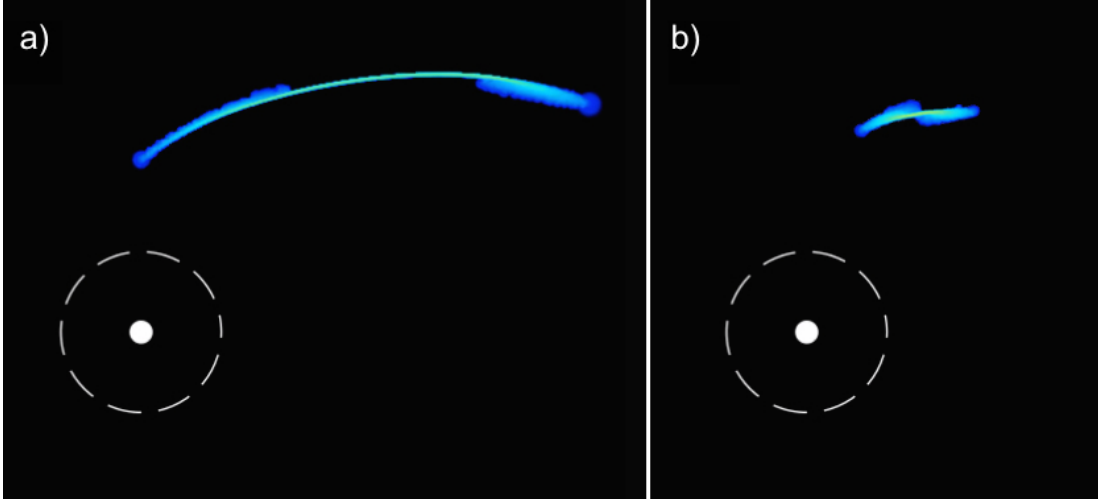
Figure 4.2: Fallback phase of the debris after first passage to r_p from two TDEs. In panel a) is shown the typical stretching and fallback at low β of the leading tail, which is in deeper potential with respect to the second tail. The situation is different for higher β (panel b)), where the tails both sit in deep potential and cannot stretch, resulting in a more compact clump.

with $\beta = 1$ (first row of Fig. 4.3 and Fig. 4.5). Finally, the second debris tail at higher energy, which is the last to fall back, translates into the decrease in the fallback rate. For low eccentricity, the fallback timescale of both debris tails is similar, while for longer eccentricities the timescale for the second tail fallback is longer. We note that it is not evident how the canonical assumption

$$L \propto \dot{M} \propto t^{-5/3} \tag{4.7}$$

should hold at late stages of the TDE (Lodato & Rossi, 2011), when the circular disc forms due to circularisation processes.

The central peak present in the specific energy distribution in models S1.95 and S1.99 is slightly visible also in the mass return rate distribution. This is not the case for s1.95 and s1.99.

Regarding the duration of TDEs, we find that for TDEs with $e = 0.99$, i.e. S1.99 and s1.99, the mass return rate distribution behaves as what expected from the parabolic one, lasting for order months to years. For $\beta = 1$, for s1.6, s1.7 and s1.8 the duration is few hours and for the other models it is $\sim$ days to few months, but the rate is higher. If translated to a lightcurve assuming that $L \propto \dot{M}c^2$ is valid (Lodato & Rossi, 2011), these TDEs would be hard to catch observationally because they would appear as short peaks. If they were to occur in active galaxies, then they could be hidden as AGN variability, making them even more difficult to observe; however, this assertion needs considerations on the duration with respect to the variability, and on the relative luminosity. The detectability situation becomes even worse for $\beta \geq 2$, as the duration is of the order $\lesssim$ day.

Finally, a comparison between S like stars and solar like stars shows that TDEs produced by a MBH like Sgr A* are similar in duration, as it can be expected
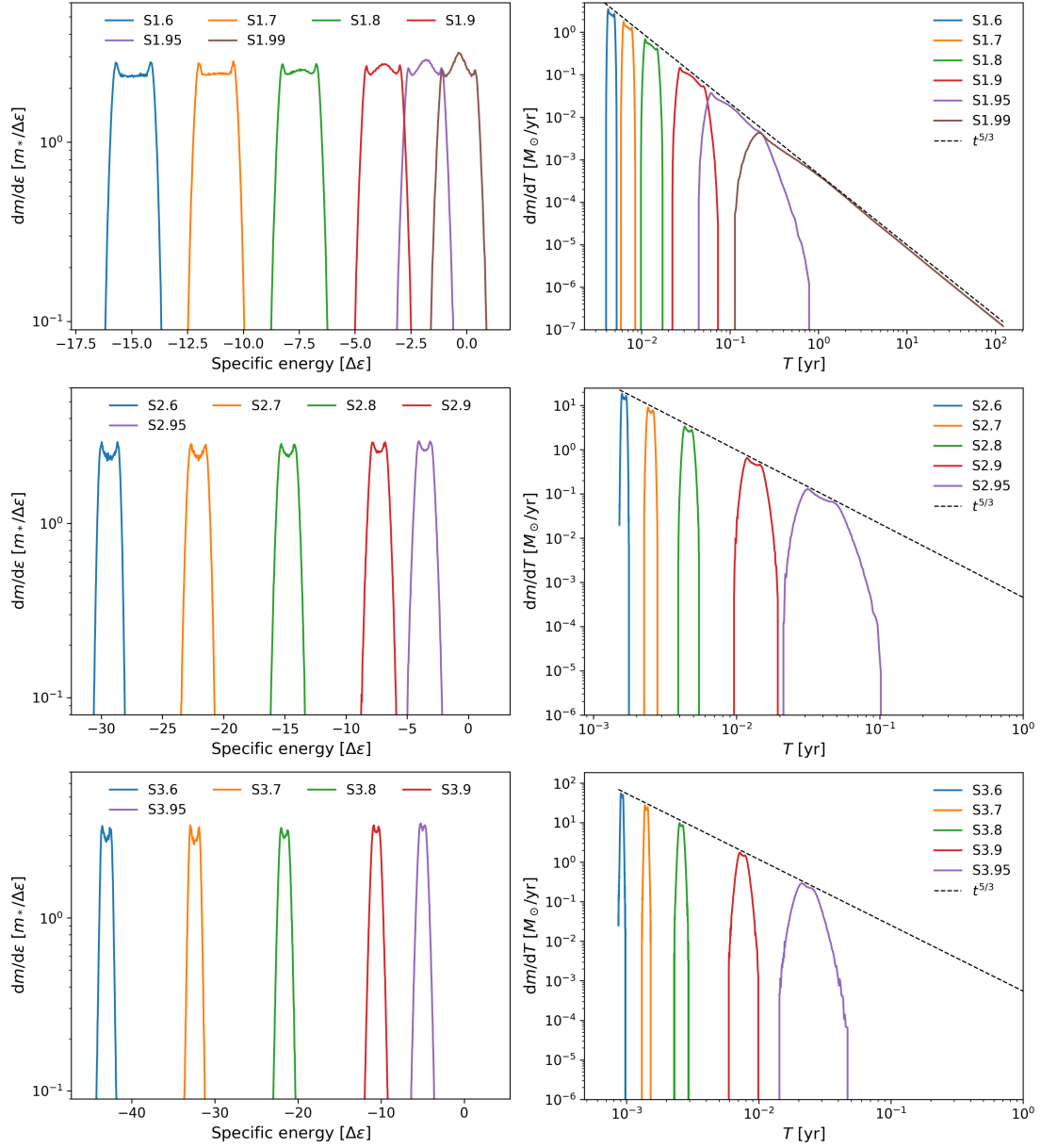
Figure 4.3: Plots of specific energy distributions (left) and corresponding mass return rate distribution (right) of TDEs with $M = 10\ M_\odot$, $R = 5\ R_\odot$ for $\beta = 1$ to 3, from top to bottom. The colours correspond to different eccentricities of the simulation as shown in the legend. Each plot corresponds to the debris after disruption at first passage and before second passage through r_p.
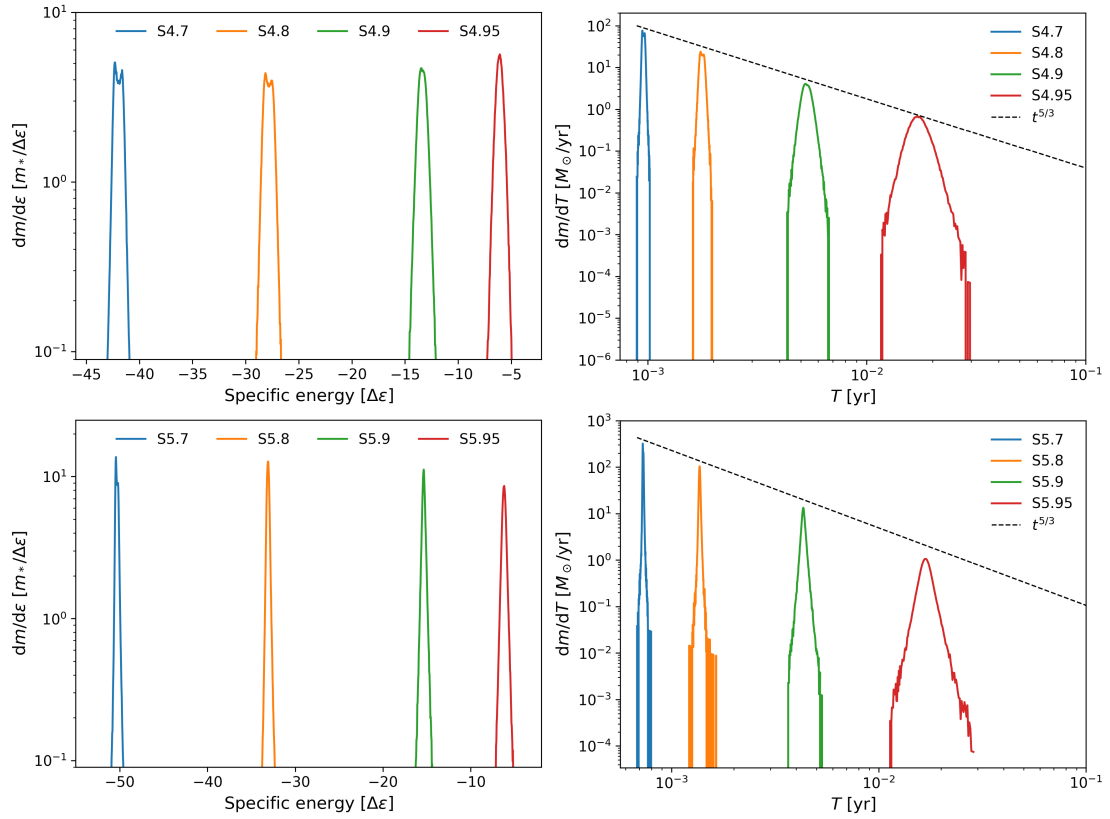
Figure 4.4: Plots of specific energy distributions (left) and corresponding mass return rate distribution (right) of TDEs with $M = 10\ M_\odot$, $R = 5\ R_\odot$ for $\beta = 4$ to 5, from top to bottom. The colours correspond to different eccentricities of the simulation as shown in the legend. Each plot corresponds to the debris after disruption at first passage and before second passage through r_p.
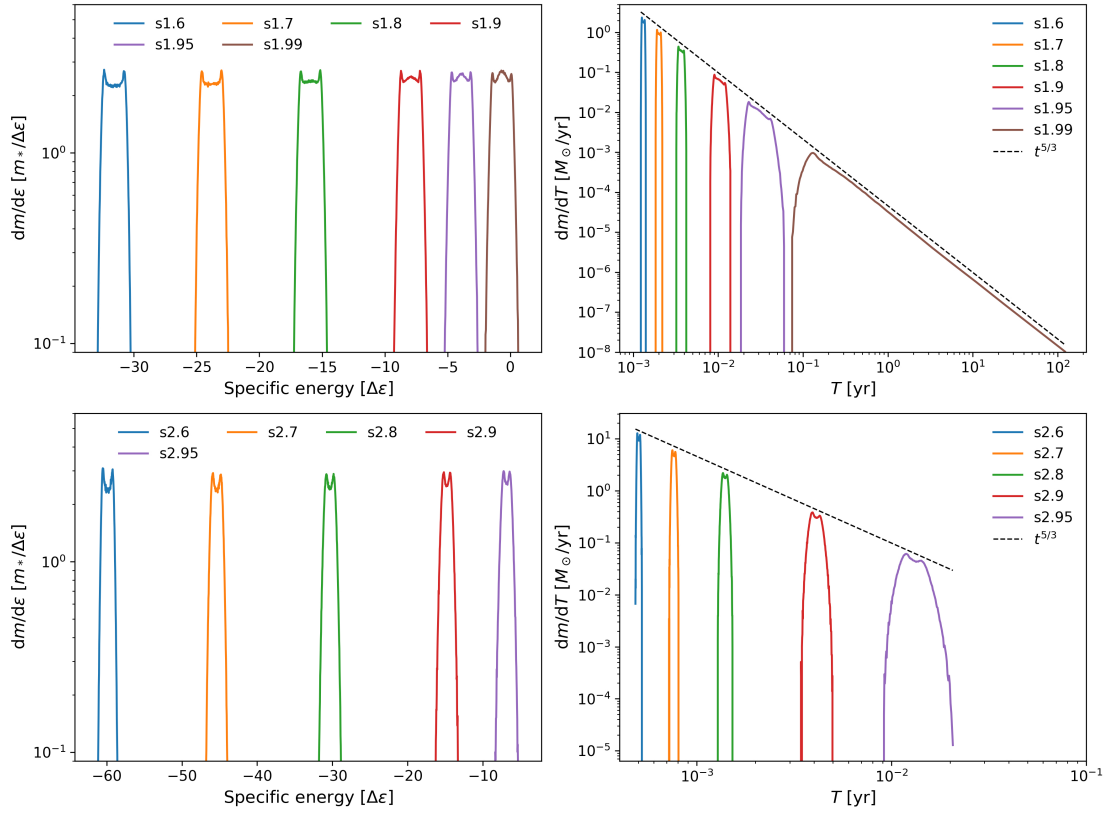
Figure 4.5: Plots of specific energy distributions (left) and corresponding mass return rate distribution (right) of TDEs with $M = 1\ M_\odot$, $R = 1\ R_\odot$ for $\beta = 1$ to 2, from top to bottom. The colours correspond to different eccentricities of the simulation as shown in the legend. Each plot corresponds to the debris after disruption at first passage and before second passage through r_p.
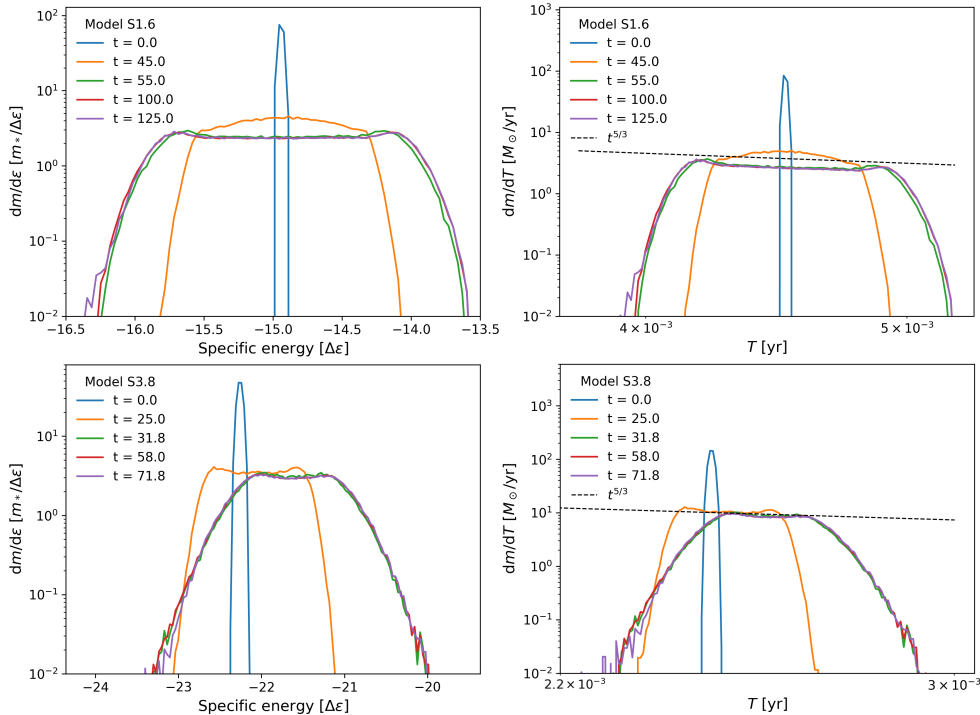
Figure 4.6: Plot of specific energy distribution (left) and corresponding fallback mass rate (right) of models S1.6 (top) and S3.8 (bottom). The colours correspond to different times of the simulation: blue is at star's initial position at r_{a}, orange is at the first passage to r_{p}, green is during the formation of two debris tails, red is during stretching and falling back of the most bound debris tail, and purple is at the second passage to r_{p}.

since the main timescale behind a TDE depends on the mass of the MBH. We note that TDEs produced by S stars are likely to have a higher peak since more stellar mass contributes to the mass return rate.

4.2 Circularization of debris

There are different mechanisms which allow the debris to dissipate kinetic energy and to circularize (Evans & Kochanek, 1989; Kochanek, 1994). When the star is disrupted, the debris obtains a range of inclinations and their orbits will be vertically focused, intersecting close to pericenter. As a result of the strong compression at this point, a so-called pancake shock is generated. Upon returning to pericenter, relativistic apsidal precession contributes to debris self-crossing, generating shocks due to the head of the debris colliding with its tail, which is still falling back.

Another effect that occurs is shearing due to the radial focusing of the debris: their orbits have a small range of r_{p} and a wide range of r_{a}, resulting in the debris going through the nozzle. In addition, the debris also have a range of apsidal angles and eccentricities, which shear the stellar material.

In general, we observe two behaviours of the circularisation of the stellar debris, depending on the initial orbital parameters e and β: a) shocks and higher precessing angles allow the debris to form a circular disc quickly, b) the shocks
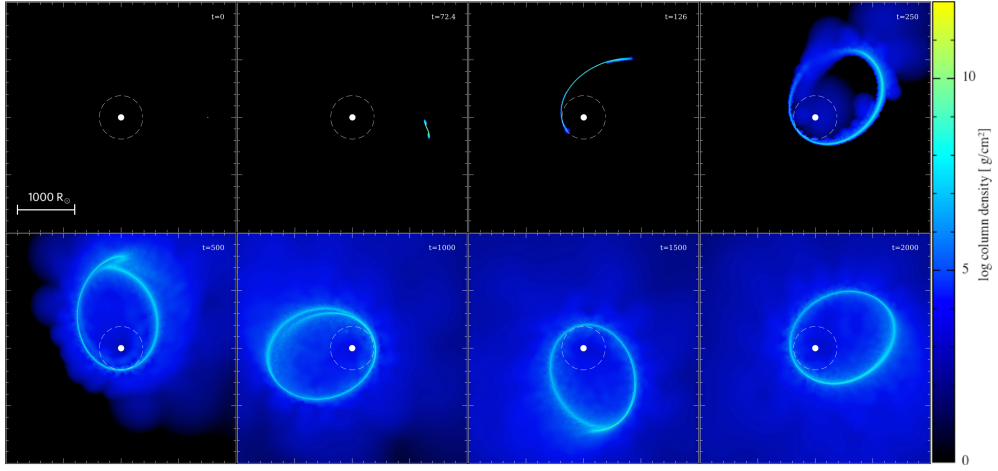
Figure 4.7: Sequence of snapshots of model S1.6. The dashed circle defines the tidal radius $r_t = 377.4 R_\odot = 41.4 r_{\mathrm{g}}$, the white full circle defines the MBH $r_{\mathrm{ISCO}} = 54.7 R_\odot = 6 r_{\mathrm{g}}$. The reference distance scale is shown for $1000 R_\odot = 109.6 r_{\mathrm{g}}$. Time is in code units ($\Delta t = 1594$ s $= 5 \cdot 10^{-5}$ yr).
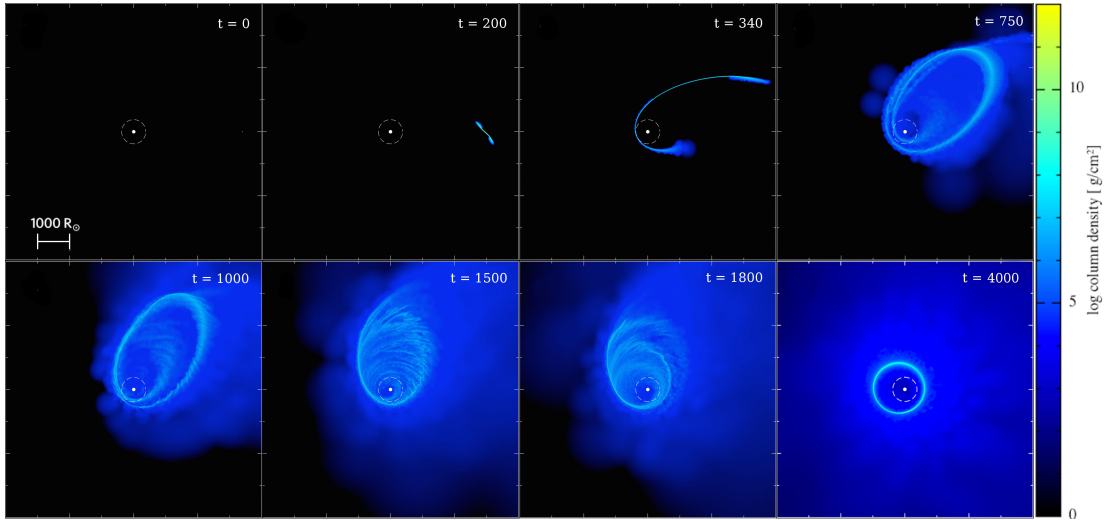

Figure 4.8: Sequence of snapshots of model S1.8. The dashed circle defines the tidal radius $r_t = 377.4 R_\odot = 41.4 r_{\mathrm{g}}$, the white full circle defines the MBH $r_{\mathrm{ISCO}} = 54.7 R_\odot = 6 r_{\mathrm{g}}$. The reference distance scale is shown for $1000 R_\odot = 109.6 r_{\mathrm{g}}$. Time is in code units ($\Delta t = 1594$ s $= 5 \cdot 10^{-5}$ yr).

are not impactful enough to allow fast circularisation and, as a consequence, the debris follows elliptical orbits. From our simulations, we find that we can distinguish four different types of debris behaviour:

- type 1: the debris does not circularise efficiently and a disc is not formed or is formed after relatively long time (e.g. S1.6, Fig. 4.7);

- type 2: the debris slowly circularises and eventually forms a disc with no debris falling back (e.g. S1.8, Fig. 4.8);

- type 3: the debris relatively quickly circularises and forms a disc while there is still debris falling back (e.g. S1.95, Fig. 4.10);

- type 4: the debris quickly and efficiently circularises, mainly through self-crossings and shocks, and forms a disc with no debris falling back (e.g. S3.8, Fig. 4.11).

Type 1 occurs in TDE models with $\beta = 1$ and low eccentricity ($e = 0.6$ and 0.7). In this case self-crossings are basically non existent since the leading debris does not reach the still in falling tail, thus not allowing the typical circularization processes to occur. The debris settles on an elliptical disc as shown in the bottom row of Fig. 4.7 and precesses around the MBH, gradually and eventually becoming a circular disc (it can be deduced, for example, from the shift to lower eccentricities values of the distribution of eccentricity in Fig. 4.12, first panel in the top row).

In types 2, 3 and 4 self-crossing occurs and leads to circularization. From visual inspection of simulation snapshots we can estimate the time at which the circularization and disc formation happen (relative to the start of the simulation). We find that, for example, model S3.8, which is of type 4, forms a disc at $t \sim 500$ in code units (Fig. 4.11), while model S1.95, which is type 3, forms it at $t \sim 4000$ (Fig. 4.10) while there is still debris falling back. Also for model S1.8 we find that the disc forms at $t \sim 4000$ (Fig. 4.8), however in this case there is no debris falling back and is therefore classified as type 2.

For S-like stars and $\beta = 1$, we can identify a dividing value of the initial stellar eccentricity $e = 0.8$: models S1.6, S1.7 and S1.8 show a transition from type 1 to type 2, while models S1.9 and S1.95 are of type 3 (we could not identify the type for S1.99 since circularisation starts at very late times and would require very long computational time). Models with $\beta = 2$ are also divided at $e = 0.8$, but with the difference that models with low eccentricity S2.6, S2.7, S2.8 show a transition from type 2 to type 4, while models S2.9 and S2.95 are of type 2. For $\beta = 3$, 4 and 5 the S star models show a behaviour of type 4.

For solar-like stars and $\beta = 1$, we find that models with low eccentricities, that is s1.6, s1.7, are of type 1, while models s1.8, s1.9 and s1.95 are of type 2, and model s1.99 of type 3. Lastly, for $\beta = 2$ models s2.6, s2.7 show transition from type 2 to type 4, while s2.8, s2.9 and s2.95 are of type 4.

We estimated from visual inspection of simulation snapshots the approximate distance r_{sc} at which the first self-crossing occurs. We then calculate the ratio between r_{sc} and the tidal radius r_t, the apocenter distance r_a and the pericenter distance r_p (Tab. 4.2) to check if there are any particular relations between them and circularization types to help further into the classification. In Fig. 4.9 we
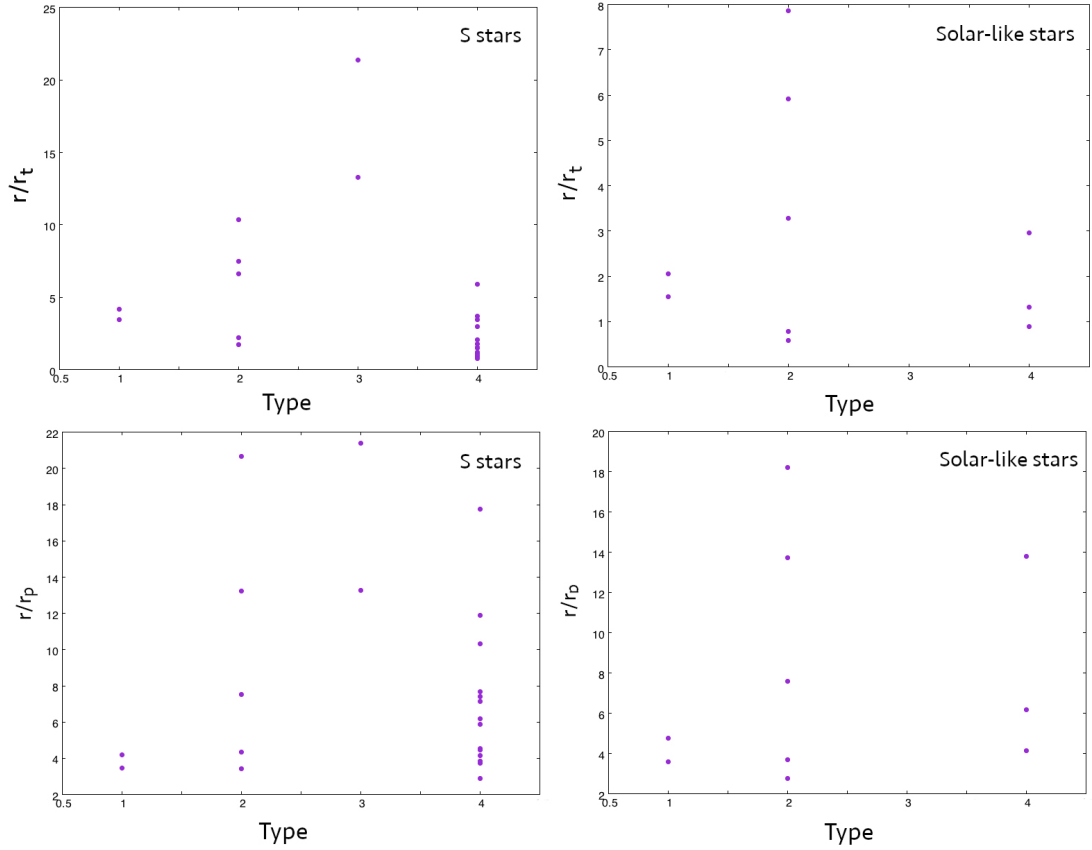
Figure 4.9: Plots of the ratio between the distance of first self-crossing and the tidal radius, r_{sc}/r_t against the types (upper plots), and between the distance of first self-crossing and the pericenter distance, r_{sc}/r_p against the types (bottom plots). S stars data are plotted on the left side and solar-like stars on the right side. Types for each model and the ratios are in Tab. 4.2. For models where the type could not be defined exactly (for example, model S1.8 is defined as type 1/2), it was taken the lower type (S1.8 is shown as type 1 in the plots).

Figure 4.10: Sequence of snapshots of model S1.95. The dashed circle defines the tidal radius $r_t = 377.4R_\odot = 41.4r_g$, the white full circle defines the MBH $r_{ISCO} = 54.7R_\odot = 6r_g$. The reference distance scale is shown for $1000R_\odot = 109.6r_g$. Time is in code units ($\Delta t = 1594$ s $= 5 \cdot 10^{-5}$ yr).
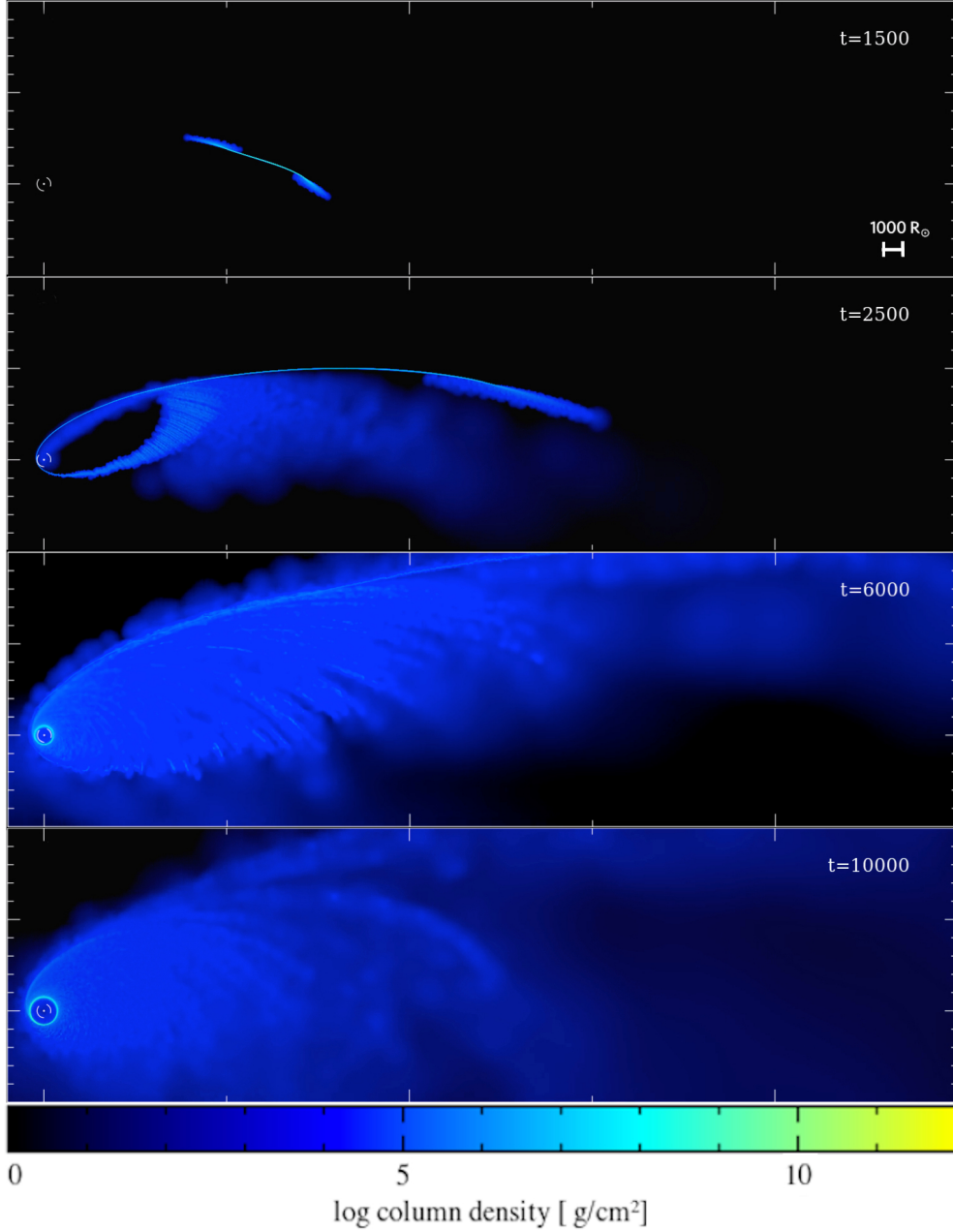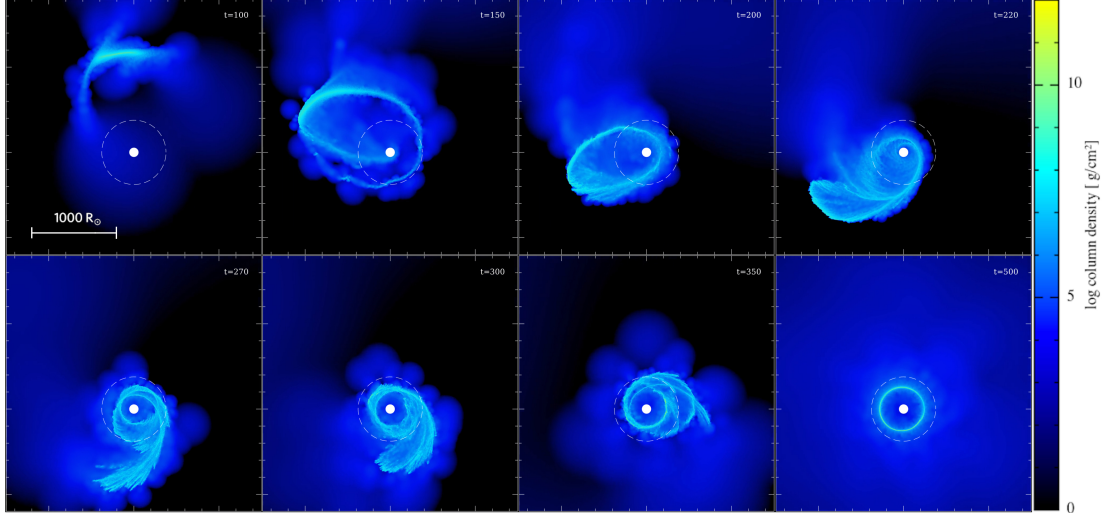
Figure 4.11: Sequence of snapshots of model S3.8. The dashed circle defines the tidal radius $r_t = 377.4 R_\odot = 41.4 r_g$, the white full circle defines the MBH $r_{\mathrm{ISCO}} = 54.7 R_\odot = 6 r_g$. The reference distance scale is shown for $1000 R_\odot = 109.6 r_g$. Time is in code units ($\Delta t = 1594$ s $= 5 \cdot 10^{-5}$ yr).

show the most relevant plots, that is between types and r_{sc}/r_t and r_{sc}/r_p. We do not find any relation.

In the following we describe our analyses and support for this type classification.

4.2.1 Eccentricity and angular momentum distribution

We analysed the identified circularisation types by using angular momentum and eccentricity distribution of debris. We calculated angular momentum l from Eq. 3.38 and eccentricity e by using the specific energy of each fluid element (Eq. 3.37) and its angular momentum:

$$e = \sqrt{1 + \frac{2\epsilon l^2}{(GM_{BH})^2}} \qquad \text{for r} >> r_g. \tag{4.8}$$

In Fig. 4.12, the debris eccentricity distributions (first column) and the angular momentum distribution (second column) are shown at different times, for models S1.6, S1.7 and S1.8, which we find to show a transition from type 1 to type 2. In particular, for model S1.6 little to no shock contributes and hence the debris follows the initial distribution of eccentricities (type 1). This is reflected in the angular momentum distribution, which changes very little over time. In model S1.7 (second row of Fig. 4.12) the situation is similar to S1.6, however in the angular momentum distribution there is a larger shift towards angular momentum $l/l_* = 1$ at $t = 2000$, which we associate to the transition from type 1 to type 2. The eccentricity distribution remains wide and shifts slightly to lower values. Finally, in model S1.8 (third row of Fig. 4.12), the effect given by shocks during the circularization process is more evident by the more significant shift towards lower eccentricities of the debris. At time $t = 4000$ the disc settles and

85

the eccentricity distribution is narrow and centred around $e \sim 0.16$. This is seen also in the angular momentum distributions, where the distributions at $t = 1000$ and 1500 show a secondary peak at lower angular momenta that represents matter which is going to be accreted and thus rising the angular momenta of the rest of the debris, and at $t = 4000$ the distribution is narrow centred around a value slightly larger than $l/l_* = 1$.

In Fig. 4.13, we show examples with models s1.95, S1.95 and S3.8 to show the difference between type 2, 3 and 4. The left panel of Fig. 4.13 shows the angular momentum distribution of model s1.95 (type 2). Here the debris is spread over a wider range of angular momenta with respect to S1.8 and the behaviour is similar; the distribution gets narrower as the debris is circularizing at $t = 10000$ (yellow line). A different case is shown in the middle panel of Fig. 4.13, where we show the angular momentum distribution of S1.95 (type 3, Fig. 4.10). At $t = 6000$ there is a circular disc already formed (peak centred around 0.85 l/l_*), while there is still most of the debris falling back, which has similar angular momenta ranging between ~ 1.2 and 1.4 l/l_*. The debris configuration at $t = 8000$, 12000 and 14000 is similar, and the angular momentum of the disc is increasing. Finally, the angular momentum distribution of S3.8 (type 4, Fig. 4.11) in the right panel of Fig. 4.13, shows the angular momenta span over a similar range through all the circularisation process because the debris undergoes stronger self-crossings and shocks. We see that the disc forms in a short time and that there is not a lot of debris left over.

We note that in type 3 TDEs, we observe disc formation while there is still debris falling back, as also seen from the angular momentum distribution. In model S1.95, the bound debris falling back on elliptical trajectories, with r_a of the order of the initial stellar orbit, has a range of angular momenta and form an "elliptical shaped disc", as seen in Fig. 4.10. In order to form this accretion flow, the bound debris need to lose a significant amount of energy. As suggested by Piran et al. (2015), the energy thus liberated during disc formation may power the optical TDE candidates, rather than the energy coming from the accretion disc itself. Furthermore, it is a common idea to consider circular accretion as an efficient radiation source to power TDEs, since it was successfully applied as the Shakura & Sunyaev (1973) model to power AGN. However, the recent TDE observational data do not show such high energetic efficiencies, and simulations show that in some case most of the debris stay on eccentric orbits for long times. As demonstrated by Svirski et al. (2017), high accretion flows may radiate little enough to explain the relative small radiation fluence observed from TDE candidates. It is not clear, however, how this would affect the resulting lightcurve.

4.2.2 Temporal evolution of energy

To get some additional insight in the circularization process, we calculate the temporal evolution of the average specific orbital energy relative to circularization energy ϵ_{circ} (later defined in Eq. 4.10) and how it is affected by the orbital parameters e and β. The circularization energy is the energy corresponding to the disc formed by circularization. To analyze how the evolution of specific energy changes with e and β, we refer to two example cases, which we show in Fig. 4.14.
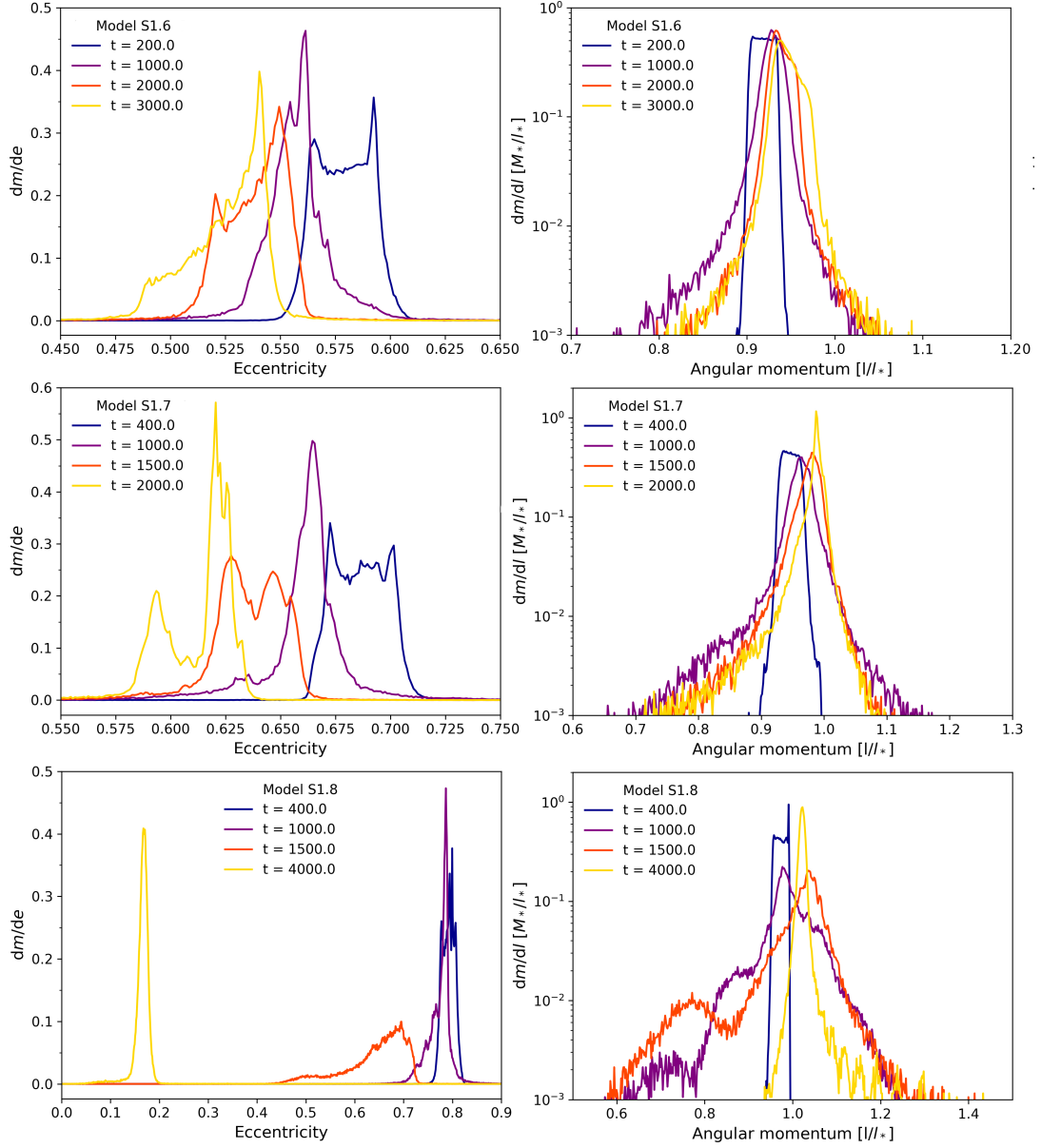
Figure 4.12: Eccentricity distributions (first column) and angular momentum distribution (second column) for models S1.6, S1.7 and S1.8. For each plot the evolution of the corresponding distribution is shown for different times t (at $t = 0$ the star is at the apocenter r_{a}). Time is in code units ($\Delta t = 1594$ s $= 5 \cdot 10^{-5}$ yr).
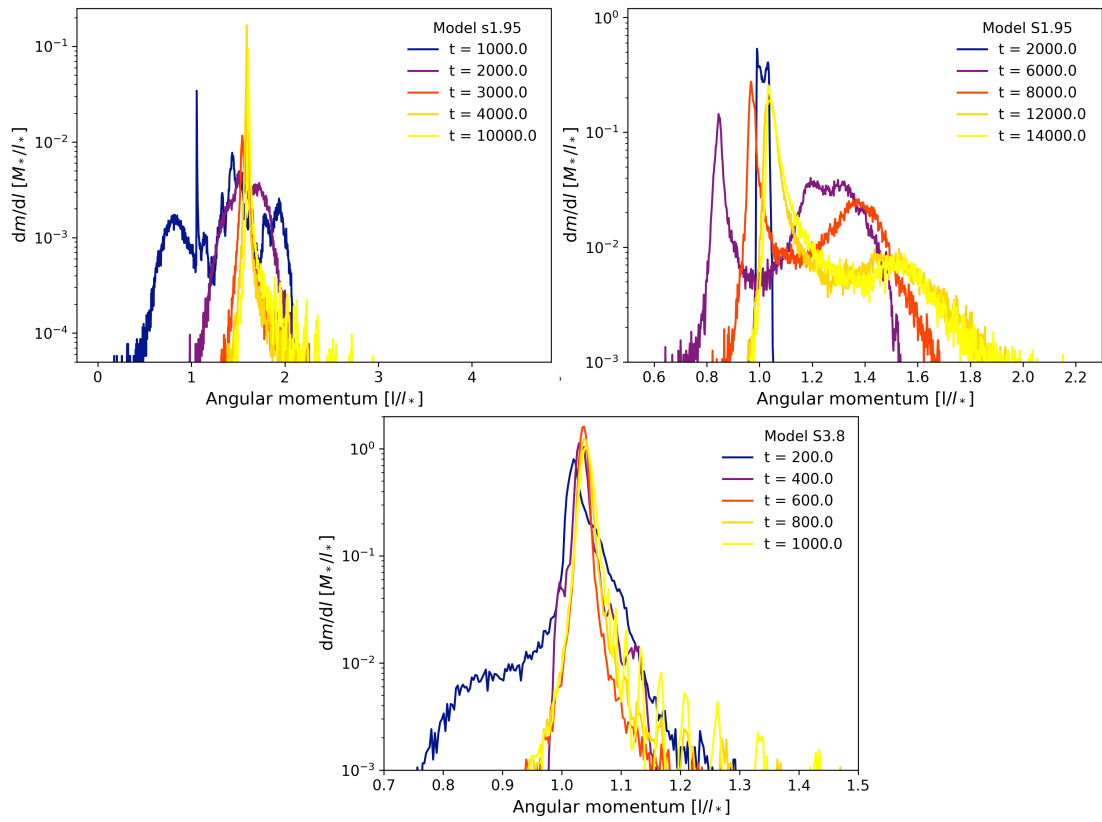
Figure 4.13: Angular momentum distribution for models s1.95, S1.95 and S3.8. For each plot, the evolution of the distribution is shown for different times t (at $t = 0$ the star is at the apocenter r_a). Time is in code units ($\Delta t = 1594$ s).
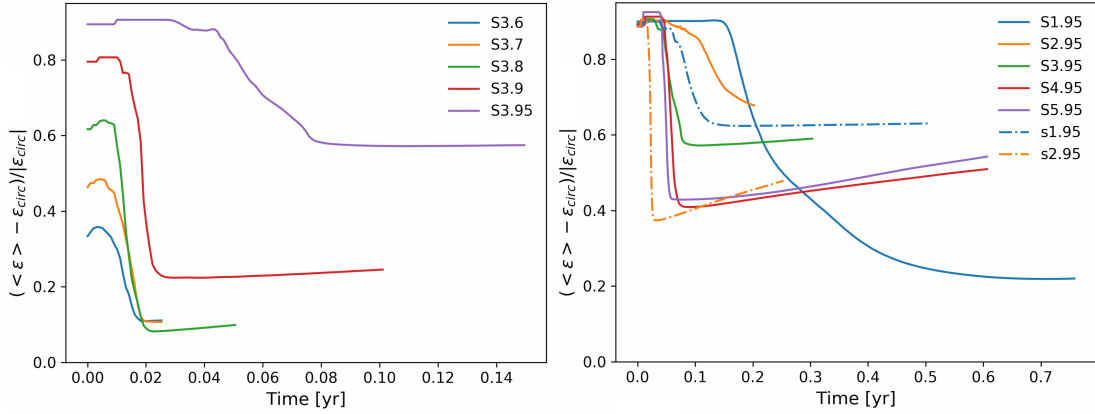
Figure 4.14: Plot of average specific energy relative to circularisation energy of S-star models with $\beta = 3$ (left) and for solar-like and S star models with initial orbital eccentricity $e = 0.95$ (right).

In the left-hand panel of Fig. 4.14 , we plot all S star models with $\beta = 3$ and we observe a drop in average specific energy that becomes steeper for increasing eccentricity from $e = 0.6$ to 0.9 and then becomes slightly shallower for $e = 0.95$. The drop comes from the orbital energy dissipated during debris self-crossings and the generated shocks. This behaviour is consistent with results observed in previous simulations (e.g. Hayasaki et al., 2013). The increase in drop steepness with eccentricity is related to the relativistic precession acting more effectively for more eccentric orbits, thus allowing self-crossing to be more efficient. This mechanism becomes more effective with increasing β, as shown in the right-hand panel of Fig. 4.14. In addition, we observe a shallower drop instead of an increase of steepness for $e = 0.95$ for $\beta = 1$, 2 and 3 for S stars, while for solar-like stars only for $\beta = 1$ and also $e = 0.99$. At $\beta = 4$ and 5 for S stars and 2 for solar-like stars, this behaviour is not observed.

All results are shown in Fig. 4.15, where we give the evolution of average specific energy for S star and solar-like star models and each plot includes models with same β for the same type of star, while in Fig. 4.16 each plot includes models with same eccentricity.

The specific energy curves are characterised by a constant temporal evolution after the drop to lower energies. This reflects the fact that the debris is circularising, but it does not tell us when the disc might or might not have settled. From visual inspection of the simulation snapshots, we find that the disc can be formed at different times during the constant temporal evolution for different models.

4.2.3 Temporal evolution of accreted matter

Since the circularization process affects the dynamics of the debris, it can also affect how much debris is accreted before the disc is formed affecting the mass of the final disc. We carried out an analysis on the temporal evolution of the accreted matter, which we now start to describe by referring to two example cases shown in Fig. 4.17. All results are shown in Fig. 4.18, where we give the evolution of the accreted mass of S star and solar-like models and each plot includes models with same β for the same type of star, while in Fig. 4.19 each
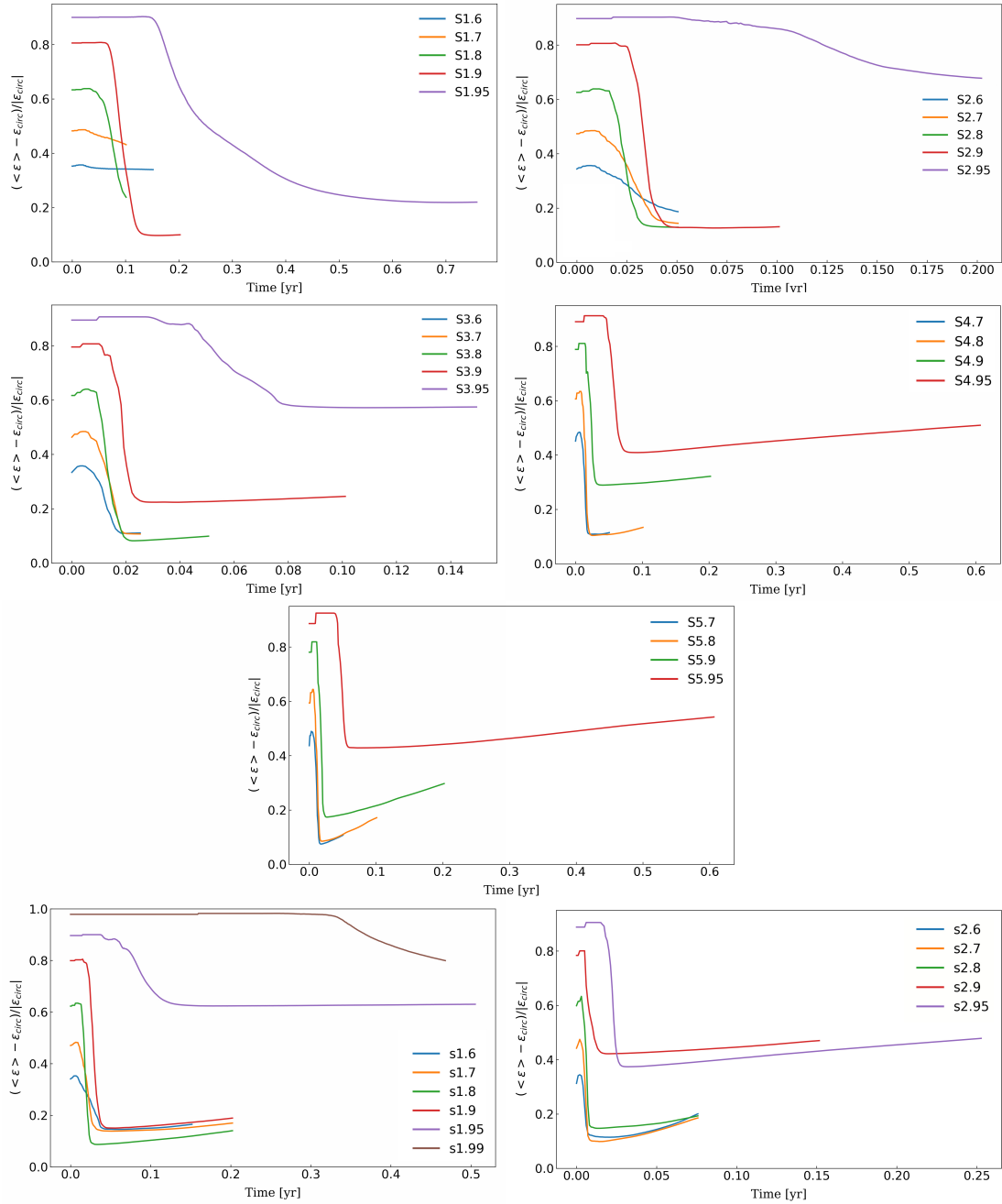
Figure 4.15: Plots of average specific energy relative to circularisation energy of all models. In each plot the value of the penetration factor β is fixed.
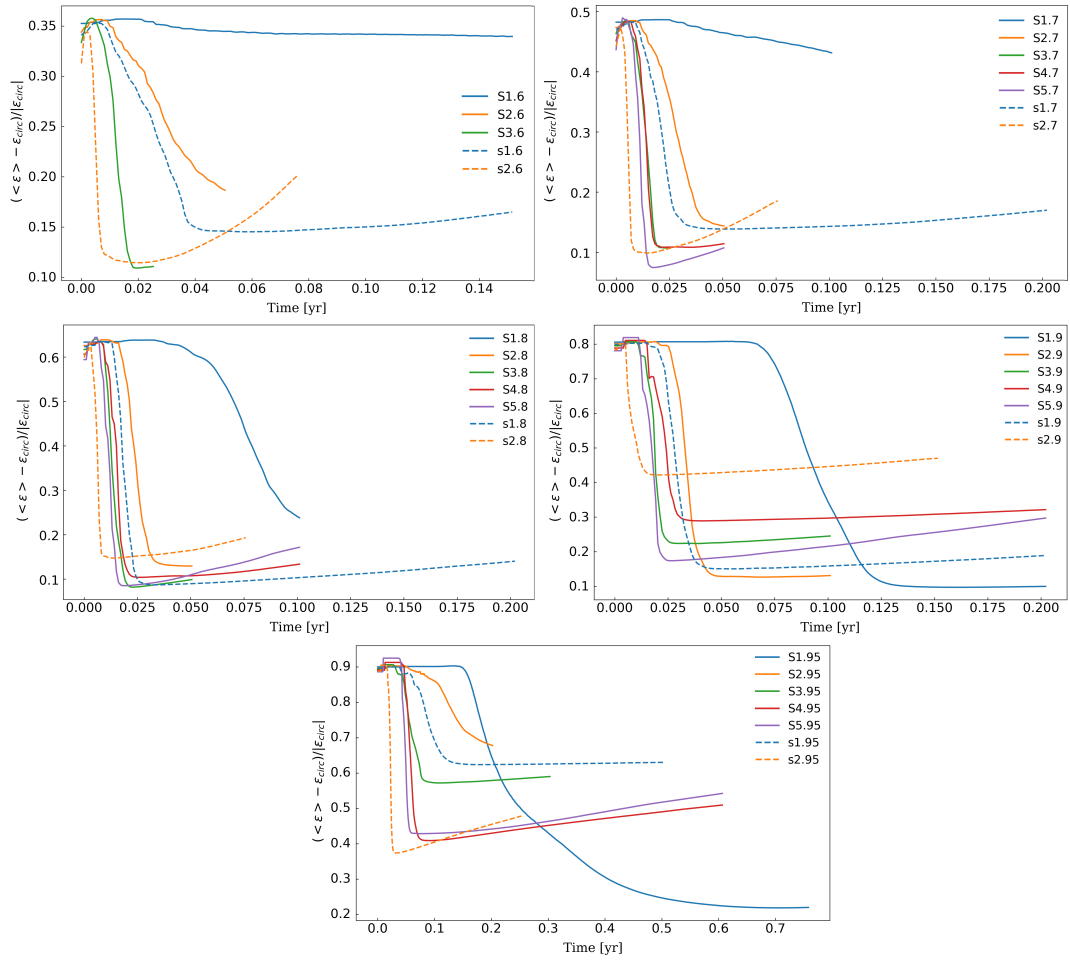
Figure 4.16: Plots of average specific energy relative to circularisation energy of all models. In each plot the value of the eccentricity e is fixed. Solid lines define S stars, while dashed lines define solar-like stars.

plot includes models with same eccentricity.

In Fig. 4.17 we show the mass of accreted debris for S-stars models with fixed eccentricity $e = 0.7$ (left panel) and $e = 0.95$ (right panel) for β from 1 to 5. The curves are characterised by a rise followed by a knee and a somewhat constant increase over time. The initial rise corresponds to the phase in which self-crossings occur. We evaluate the rise time between the start of the rise and the knee from the plot in Fig. 4.17 and report the values in Tab. 4.1. From the rise time we observe that for $e = 0.7$ (left panel of Fig. 4.17) debris is accreted faster when β is increased from 1 to 2. Increasing the value of β further affects very little the rise time of accreted matter in this phase. In general, the mass of accreted matter is increasing with increasing values of β. These models show a transition in type going from type 1/2 for model S1.7 to type 4 for the other models. In type 4 models the self-crossings and the shocks play a more important role. In this case they modify the trajectory of the debris such that more of it is accreted by the MBH.

The situation is different if the eccentricity is increased. For $e = 0.95$ (right panel of Fig. 4.17) the matter is accreted faster for each increase of β (see values in Tab. 4.1). From a visual inspection of the simulation snapshots we see that in models S2.95, S3.95, S4.95 and S5.95 the debris falls in an almost radial trajectory into the MBH to which we attribute the larger accreted mass. The models in this plot are type 3 for S1.95, type 2 for S2.95 and type 4 for the others. For S1.95 the disc forms while there is still debris falling back and circularising, which we interpret from the lower amount of accreted mass with respect to the other models.

We now comment what happens after the knee in the curves. When the disc is starting to form, the mass of accreted matter increases linearly with time. We note a global increase of accreted matter between left panel and right panel of Fig. 4.17: at the moment of the simulations' end, the accreted matter is in the range $\sim 0.5 - 1.2 M_\odot$ in the left panel ($e = 0.7$), while in the right panel ($e = 0.95$) the range is $\sim 1.5 - 5 M_\odot$. As mentioned, we attribute the increase of accreted matter to the debris falling back in an almost radial trajectory, thus being directly accreted by the MBH.

As discussed, the increase of accreted matter depends both on eccentricity e and on penetration factor β. High eccentricity (more evident the case of $e = 0.95$; see Fig. 4.18 and compare models with $e = 0.95$ to lower eccentricities) leads to a bigger initial fraction of accreted debris because it is already on highly eccentric orbits, and a higher penetration factor β (see Fig. 4.19) also leads to higher amount of accreted matter because the debris is affected by stronger precession, thus stronger self-crossing and shocks, which bring part of the debris on plunging orbits. We can also see how e and β affect together the evolution of the accreted mass by comparing model S1.95, S2.95, S3.95 and S4.95 in Fig. 4.17. We can see that between $\beta = 1$ and 2 there is an increase of accreted matter (the knee for S1.95 is at $\sim 1.25 M_\odot$, while for S2.95 is at $\sim 4 M_\odot$), leading to think that higher penetration factor is responsible. However, if we compare S2.95 with S3.95 there is little difference, regarding the accreted matter, and if we go to $\beta = 4$, the knee is at $\sim 3 M_\odot$, even though it shows a steeper increase after that. We interpret this difference due to interplay between e and β, which both play a role during this phase.

As a final note, in Fig. 4.18 we can notice the dividing line in behaviour at $e = 0.8$, which is more evident in the top right panel: models from $e = 0.6$ to 0.8 (type 4) show a similar accreted matter curve, different from the larger eccentricities which show a more pronounced knee followed by a linear curve (type 2).

Table 4.1: Rise time of accreted matter. The reported values are relative to the models in Fig. 4.17.

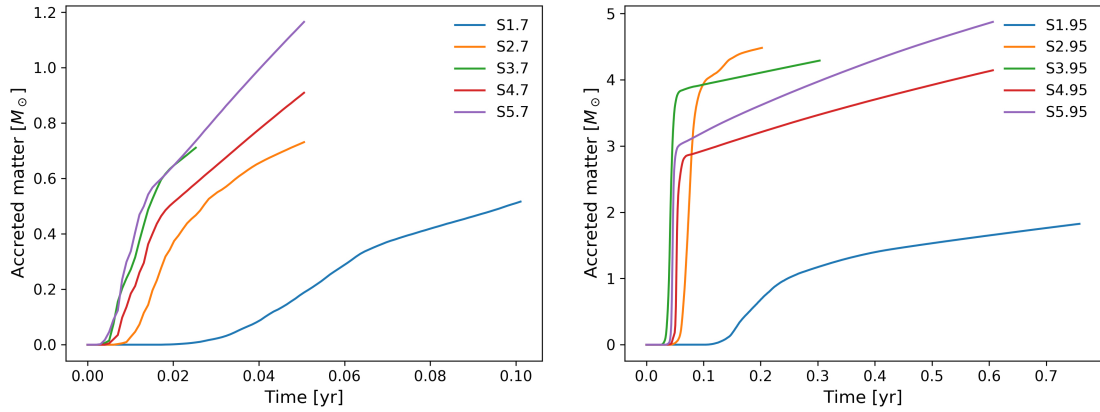| Model	S1.7	S2.7	S3.7	S4.7	S5.7	S1.95	S2.95	S3.95	S4.95	S5.95
Rise time [yr]	0.037	0.014	0.013	0.011	0.011	0.132	0.046	0.026	0.024	0.016

Figure 4.17: Plots of accreted debris mass over time. The eccentricity is fixed to $e = 0.7$ (left panel) and $e = 0.95$ (right panel), while the penetration factor β changes.

4.2.4 Circularization radius

Once the debris goes through the circularisation mechanism as described above, it will eventually form a disc, which is generally thought to be responsible for the emission we observe. In order to analyse the disk formed by circularization, a characteristic radius and specific energy, r_{circ} and ϵ_{circ} respectively, can be derived (Bonnerot et al., 2016) as

$$r_{\mathrm{circ}} = \frac{r_a^4 v_a^2 + \sqrt{r_a^4 v_a^2 [-12GM_{\mathrm{BH}}(r_a - 2r_g)^2 r_g + r_a^4 v_a^2]}}{2GM_{\mathrm{BH}}(r_a - 2r_g)^2} \tag{4.9}$$

$$\epsilon_{\mathrm{circ}} = -\frac{GM_{\mathrm{BH}}}{2r_{\mathrm{circ}}}\left(\frac{r_{\mathrm{circ}} - 4r_g}{r_{\mathrm{circ}} - 3r_g}\right). \tag{4.10}$$

In the literature, it is typically found that if all the fluid elements were able to circularize while conserving a common angular momentum equal to that of the star, $l_* = \sqrt{2GM_{\mathrm{BH}}r_t}$, then the final disk would be a ring with $r_{\mathrm{circ}} = l_*^2/(GM_{\mathrm{BH}}) = 2r_t$. We calculated r_{circ} using Eq. 4.9 and compared it to the tidal radius r_t (see Tab. 3.1, last two columns). We find that when the disk forms, the radius is approximately equal to the estimated one for $\beta = 1$ and eccentricity close to parabolic
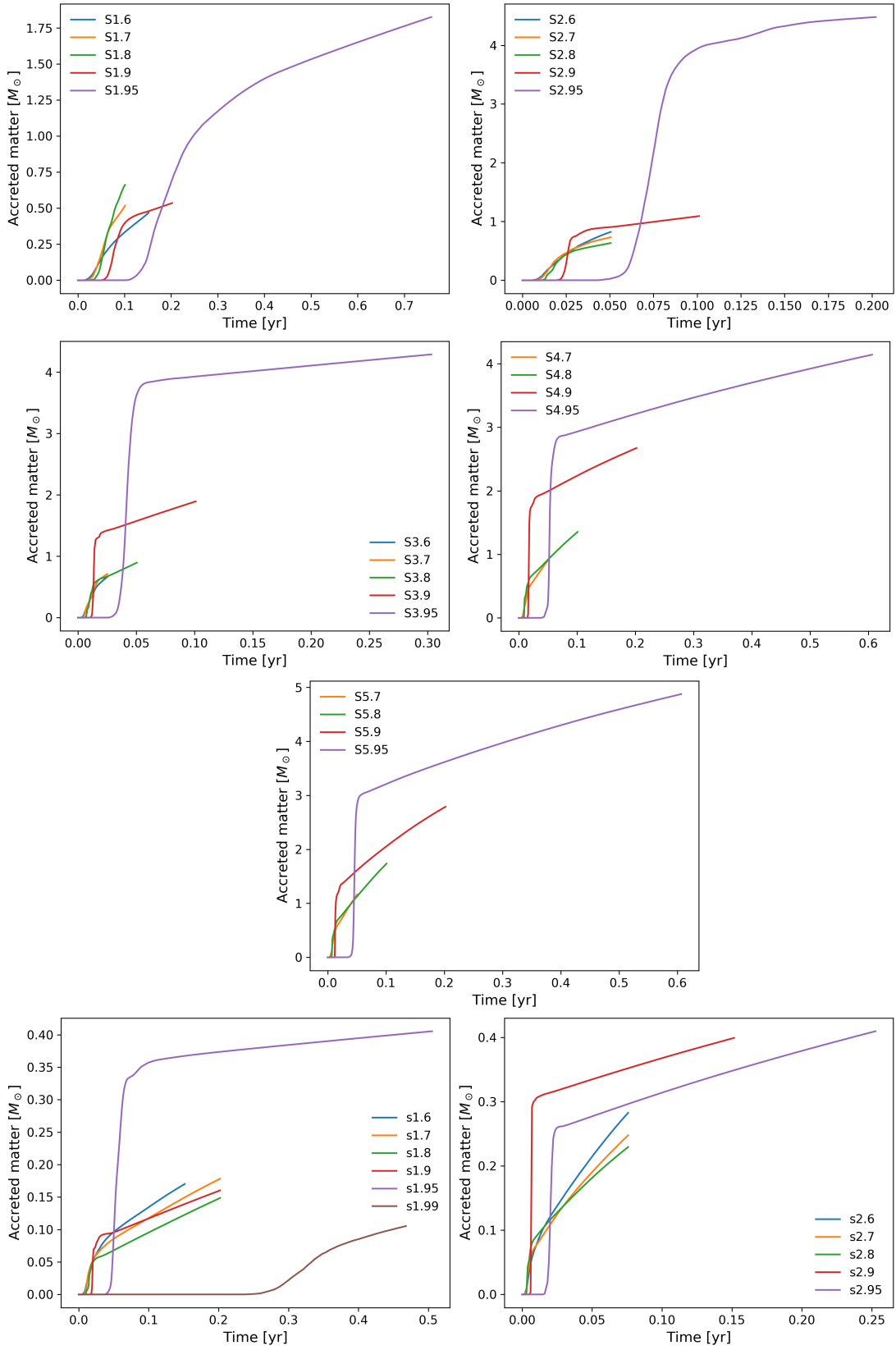
Figure 4.18: Plots of accreted debris mass over time. The penetration factor β is fixed for each plot, while the eccentricity changes. The first five plots are for the S star models, while the last two are for the solar-like models.
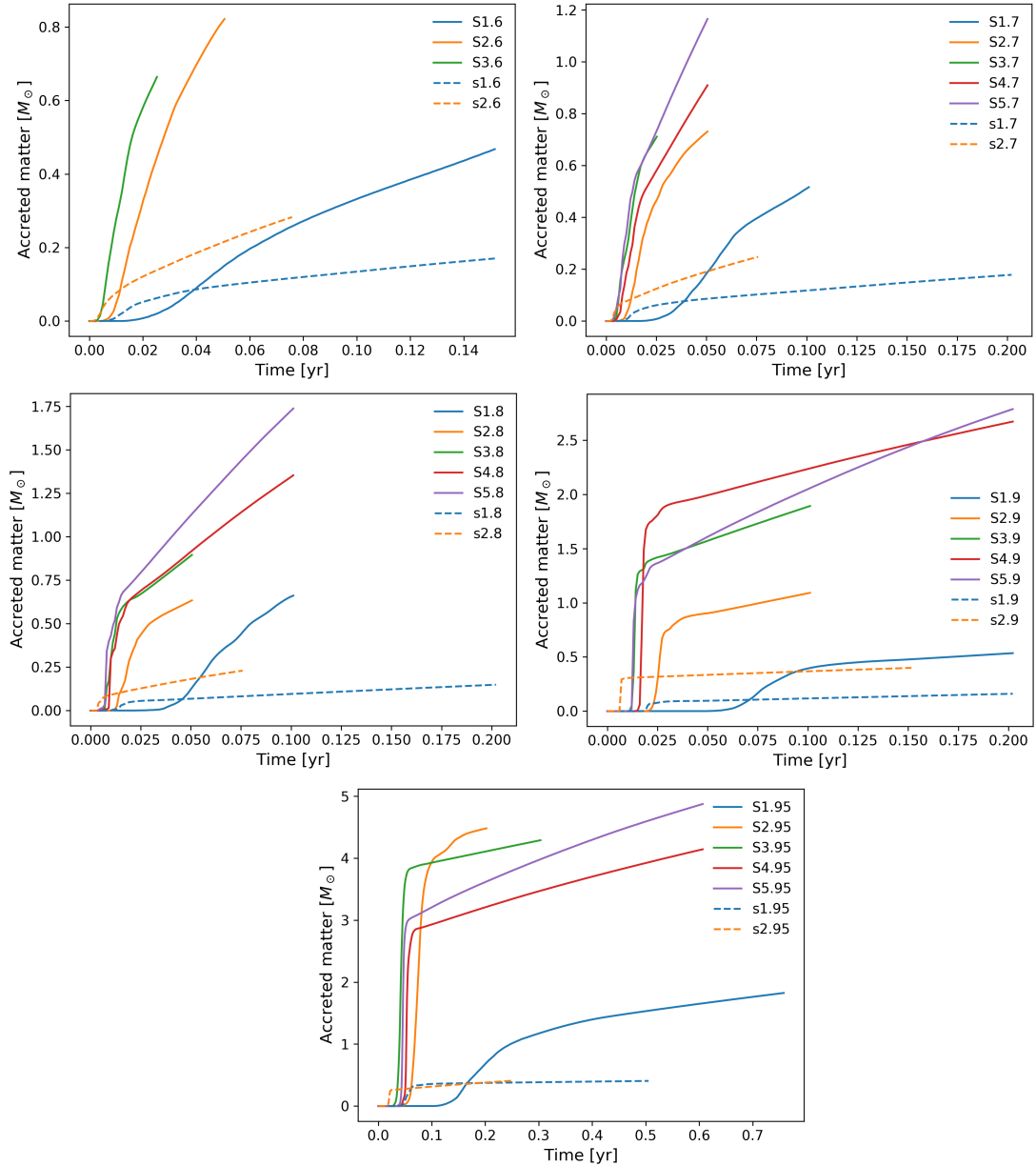
Figure 4.19: Plots of accreted debris mass over time. The eccentricity e is fixed for each plot, while the penetration factor changes. Solid lines define S stars, while dashed lines define solar-like stars.

Table 4.2: List of TDE models and their correspondent type, circularisation radius r_{circ}, the ratio between r_{circ} and tidal radius r_{t}, the rise time of the accreted mass, the approximate time of disc formation t_{disc} and the ratio between the distance of first self-crossing, r_{sc} and tidal radius r_t, apocenter distance r_a and pericenter distance r_p, respectively.

Model	Type	r_{circ}	$r_{\mathrm{circ}}/r_{\mathrm{t}}$	Rise time	t_{disc}	r_{sc}/r_t	r_{sc}/r_a	r_{sc}/r_p
Units		$R_\odot\,(r_g)$		yr	yr			
S1.6	1	607.5 (66.6)	1.6	0.220	-	3.4	0.9	3.5
S1.7	1/2	646.5 (70.9)	1.7	0.037	-	4.2	0.7	4.2
S1.8	2	685.7 (75.2)	1.8	-	0.20	7.5	0.8	7.5
S1.9	3	725.1 (79.5)	1.9	0.048	0.14	13.3	0.7	13.3
S1.95	3	744.9 (81.6)	2.0	0.132	0.20	21.4	0.6	21.4
S1.99	-	760.8 (83.4)	2.0	-	-	-	-	-
S2.6	2	306.0 (33.5)	0.8	-	-	1.7	0.9	3.4
S2.7	2/4	326.3 (35.8)	0.9	0.014	0.05	2.2	0.8	4.4
S2.8	4	346.7 (38.0)	0.9	0.016	0.04	3.7	0.8	7.4
S2.9	2	367.4 (40.3)	1.0	0.015	0.03	6.6	0.7	13.2
S2.95	2	377.9 (41.4)	1.0	0.046	-	10.4	0.5	20.7
S3.6	4	205.9 (22.6)	0.6	-	0.02	1.0	0.7	2.9
S3.7	4	220.0 (24.1)	0.6	0.013	0.02	1.5	0.8	4.4
S3.8	4	234.4 (25.7)	0.6	0.008	0.02	2.0	0.7	6.2
S3.9	4	248.9 (27.3)	0.7	0.007	0.02	3.4	0.5	10.3
S3.95	4	256.3 (28.1)	0.7	0.026	0.06	5.9	0.5	17.8
S4.7	4	167.4 (18.3)	0.4	0.011	0.01	1.0	0.7	3.8
S4.8	4	178.8 (19.6)	0.5	0.009	0.02	1.1	0.5	4.5
S4.9	4	190.4 (20.9)	0.5	0.014	0.02	1.8	0.4	7.1
S4.95	4	196.3 (21.5)	0.5	0.024	0.03	3.0	0.3	11.9
S5.7	4	136.4 (15.0)	0.4	0.011	0.01	0.8	0.7	3.7
S5.8	4	146.1 (16.0)	0.4	0.009	0.01	0.8	0.5	4.2
S5.9	4	156.1 (17.1)	0.4	0.010	0.01	1.2	0.3	5.9
S5.95	4	161.2 (17.7)	0.4	0.016	0.03	1.6	0.2	7.7
s1.6	1	264.4 (29.0)	1.6	0.031	0.05	1.6	0.9	3.6
s1.7	1	282.1 (30.9)	1.7	0.024	0.03	2.1	0.8	4.8
s1.8	2	300.0 (32.9)	1.9	0.015	0.03	3.3	0.8	7.6
s1.9	2	318.2 (34.9)	2.0	0.016	0.04	5.9	0.7	13.7
s1.95	2	327.3 (35.9)	2.0	0.052	-	7.9	0.5	18.2
s1.99	3	334.7 (36.7)	2.0	0.10	0.34	-	-	-
s2.6	2	135.9 (14.9)	0.8	0.013	0.04	0.6	0.7	2.8
s2.7	2/4	145.9 (16.0)	0.9	0.005	0.02	0.8	0.7	3.7
s2.8	4	156.1 (17.1)	1.0	0.004	0.01	0.9	0.5	4.4
s2.9	4	166.6 (18.3)	1.0	0.005	0.02	1.3	0.3	6.2
s2.95	4	171.9 (18.8)	1.0	0.009	0.03	3.0	0.4	13.8

(S1.95, S1.99, s1.9, s1.95 and s1.99). The estimate does not hold for lower eccentricities and $\beta > 1$. In addition, over time the disc radius in our simulations can increase (Fig. 4.10, panels c and d) differing from the estimated one. More detailed simulations by Bonnerot & Lu (2019) find that the trajectories of the gas within the disk span a large range of radii because angular momentum gets efficiently redistributed among the debris through multiple shocks. Thus the commonly made assumption that $r_{\mathrm{circ}} = 2r_{\mathrm{t}}$ is only expected if angular momentum exchange is negligible from the stellar disruption onwards, which, for instance, Bonnerot & Lu (2019) find is not the case, and also our results show.

4.3   Convergence of the results

Our simulations were performed with $\sim 10^5$ particles. To test how our results converge, we performed a higher resolution simulation, that is with $\sim 5 \cdot 10^5$ particles for model S1.8. We limited the test to this model due to limited computational resources.

We describe the differences we found in the following. We note some small differences from visual inspection of the simulation snapshots, the most notable being during circularization of the debris (Fig. 4.21). We see this also from left panel of Fig. 4.20, where we show the average orbital specific energy relative to circularization energy for all matter (blue lines), accreted matter (orange lines) and non-accreted matter (green lines) for the simulation with 10^5 particles (solid line) and with $5 \cdot 10^5$ particles (dashed lines). We interpret the decrease of the average specific orbital energy of all the matter due to shocks occuring from apsidal precession that converts orbital energy into thermal energy (since the simulations were performed evolving the gas with an isothermal equation of state, the extra thermal energy is removed, so that the result is shocks reducing the energy). For the same reason, the accreted matter shows the lowest energies due to shocks. Here there seem to be a somewhat less impactful effect of the shocks due to self-crossings in the higher resolution simulation in the time between ~ 0.02 and 0.04 yrs, while afterwards, as the debris starts to circularize, there are relatively minor differences.

In the right panel of Fig. 4.20 we show the evolution of accreted matter for the simulation with 10^5 particles (solid line) and with $5 \cdot 10^5$ particles (dashed line). We find that the increase of number of particles decreases the amount of accreted matter: at the end of the simulations, the accreted matter is slightly less than 2% at higher resolution, instead of $> 6\%$.

Overall, from these results we conclude that the resolution at which we ran our simulations does not affect the discussion relative to the types of circularization.
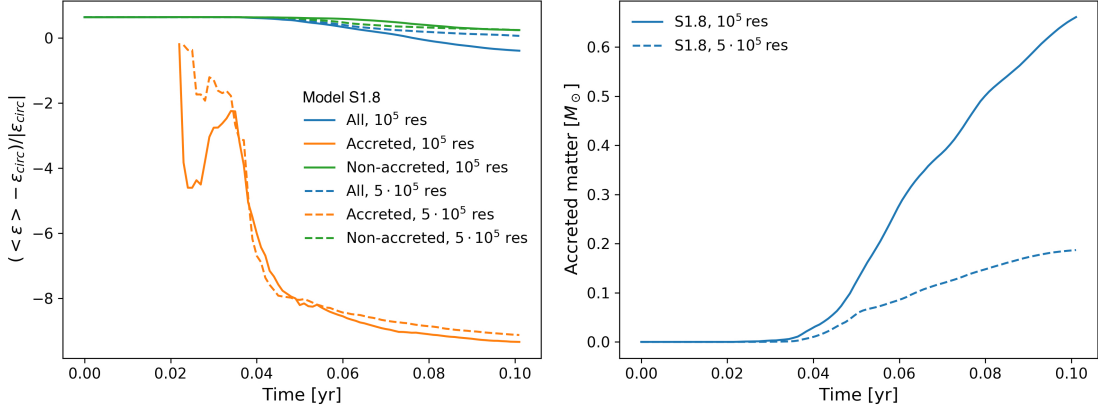
Figure 4.20: Left plot shows the evolution of average specific orbital energy relative to circularisation energy of all matter (blue line), accreted matter (orange line) and non-accreted matter (green), while right plot shows the evolution of accreted matter for model S1.8. Solid lines denote resolution at 10^5 particles, while dashed lines denote resolution at $5 \cdot 10^5$ particles.
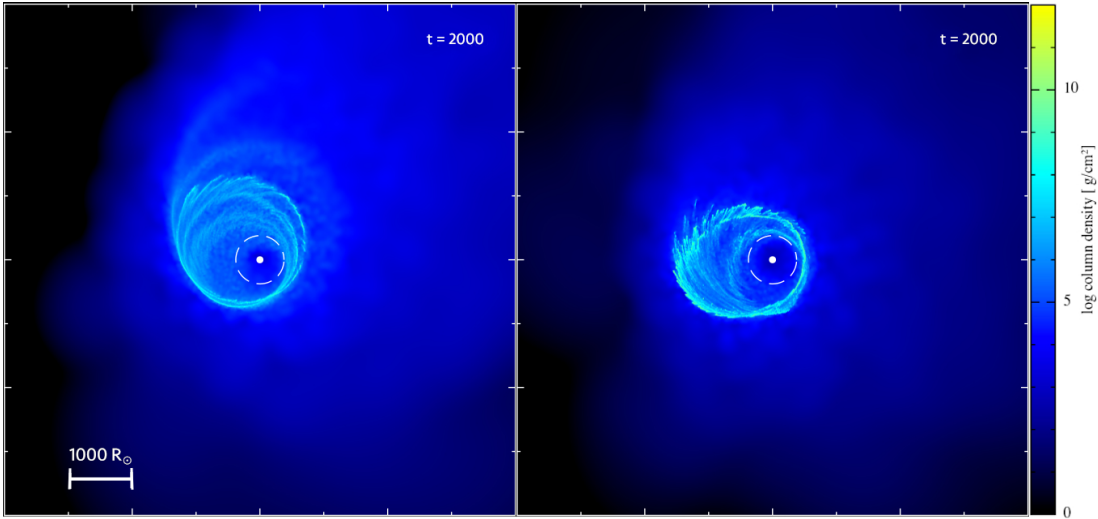
Figure 4.21: Comparison of snapshots of simulation for model S1.8 at different resolutions. The left snapshot from the simulation with 10^5 particles, while the right one has $5 \cdot 10^5$ particles. Both snapshots are shown at the same time of the simulation. The dashed circle defines the tidal radius $r_t = 377.4 R_\odot = 41.4 r_g$, the white full circle defines the MBH $r_{\mathrm{ISCO}} = 54.7 R_\odot = 6 r_g$. The reference distance scale is shown for $1000 R_\odot = 109.6 r_g$. Time $t = 2000$ is in code units and corresponds to $t = 0.1$ yr.

Conclusions

In order to fully exploit TDEs as a tool to investigate otherwise quiescent MBHs, their dynamics should be better understood. Here we study TDEs that may be produced in an environment similar to the inner parsecs of our GC. We used the SPH Phantom code (Price et al., 2018) to simulate TDEs of S-like stars ($10M_\odot$ and $5R_\odot$) and solar-like stars ($1M_\odot$ and $1R_\odot$) disrupted by a Sgr A*-like MBH ($4.3 \cdot 10^6 M_\odot$). The stellar profiles are modelled with a polytrope with $\gamma = 5/3$ and the MBH is modelled with the generalised Newtonian gravitational potential (Tejeda & Rosswog, 2013). The gas is evolved with an isothermal equation of state. We simulated TDEs with a wide range of orbital parameters, eccentricities e and penetration factors β. The chosen parameters for each TDE are given in Tab. 3.1.

Our main findings are the following:

- $dm/d\epsilon$ distributions show two features: a peak around the central value, which flattens as eccentricity decreases, and two lateral peaks called wings, related to debris tails formation;

- dm/dt distributions show similar fallback timescale of the debris tails at low eccentricities, while for higher eccentricities the tail following the head has substantially longer fallback periods. This directly affects the duration of a TDE, making those with higher eccentricities longer and more likely to be observed. Comparing TDEs produced by solar-like stars and S-like stars with same eccentricity, we find that they have similar durations, however S-like stars have higher dm/dt distributions than solar-like stars, as expected since their masses are larger;

- we identify four types of circularisation evolution: (i) the debris does not circularize efficiently and a disc is not formed or is formed after relatively long time (type 1), (ii) the debris slowly circularize and eventually forms a disc with no debris falling back (type 2), (iii) the debris relatively quickly circularises and forms a disc while there is still debris falling back (type 3), (iv) the debris quickly and efficiently circularises, mainly through self-crossings and shocks, and forms a disc with no debris falling back (type 4).

  The debris evolution and disc formation is dependent on the mechanisms and processes involved during circularisation. We find that for $\beta = 1$, if we increase the initial orbital eccentricity, there is a transition from a situation where the circularization mechanisms are not efficient (type 1) (the disc is not likely to form in short times) to a situation where relativistic apsidal precession and debris shocks begin to play a role, leading to disc

formation (type 2 and 3). An increase in the penetration factor β leads to more impactful self-crossings and shocks, which allow a quick and efficient circularisation of the debris (type 4). The behaviour of S-stars and solar-like stars is almost similar for $\beta = 1$, while for $\beta = 2$ TDEs of solar-like stars evolve as type 4 instead of type 2, meaning that for these stars the debris is all circularised when the disc is formed.

In type 4 TDEs, stellar debris is in general accreted in a more efficient way into the MBH, mostly through the self-crossings and shocks process, whereas for type 3 the accretion is more moderate. In these respects, less debris is available for the disc in type 4 than type 3.

- in general, we find $r_{\mathrm{circ}} \neq 2r_{\mathrm{t}}$, as shown also by Bonnerot & Lu (2019). We find that the relation holds only for $\beta = 1$ and eccentricities close to parabolic.

The classification of circularization types that we discussed in this work is based on rough estimations. Quantifications of the circularization processes are needed, for example on the strength of the shocks, which can be estimated from the change of kinetic energy into thermal energy in the debris, to better characterise the transition in behaviour between types. For example, we attribute to S1.8 type 1/2 (Tab. 4.2) because we could not exactly discern the type of circularization. More generally such quantification would help in understanding the difference in behaviour between type 3 and 4, which differ in the fact that in one case debris is still falling back while the disc formed and in the other case there is almost no debris falling back. This could also help in identifying timescales and magnitudes of the circularization processes.

Our models assume stars with polytropic index $\gamma = 5/3$: while polytropes might be a good first order approximation, they do not describe well the detailed structure of density profiles of different stellar types. A more detailed analysis would require more realistic stellar models. Indeed, Golightly et al. (2019b), find that there are significant deviations regarding the fallback mass rate when using realistic stellar profiles instead of polytropes, with the exception of a 0.3 zero-age main sequence star, which is well modelled by a $\gamma = 5/3$ polytrope, and the 1 $M_\odot$ zero-age main sequence star, which is well modelled by a $\gamma = 4/3$ polytrope. In particular, they find that their 3 $M_\odot$ stars all present significant differences to the fallback mass rate from both polytropes. So, we expect differences in the fallback rates for our 10 $M_\odot$ star if modelled with a realistic stellar structure, in particular a higher peak by few magnitudes (see Fig. 4 in their paper). Another notable difference when using realistic stellar models found by Golightly et al. (2019b) is that highly evolved stars are not fully disrupted even at $\beta = 3$. This does not have direct consequences on the results presented in this work because S stars are young stars (< 15 Myrs).

Also stellar spin can affect the TDE (Stone et al., 2013; Golightly et al., 2019a), and considering that young stars rotate faster, we expect possible differences. The star can be spinning retrograde or prograde with respect to its orbit. A retrograde spinning star can cause a delay or partial disruption, while a prograde spinning star can cause the debris to fallback sooner and with higher peak rate.

How much this will possibly affect our simulations depends on the magnitude of stellar rotation of the S stars.

We note that the debris is subject to viscous effect that can affect the accretion onto the MBH. We do not consider viscosity effects in our simulations and we do not expect this to significantly affect our results, following the estimation by Bonnerot et al. (2016) for an efficiently cooling gas, which is our case.

Due to computational costs, we chose to model a non-spinning MBH. However, there are observational evidences that in many cases MBHs are spinning. Based on the studies by other authors (Dai et al., 2013; Guillochon & Ramirez-Ruiz, 2015; Hayasaki et al., 2016; Liptai et al., 2019) we expect that in our study case a circularization delay may be introduced, depending on whether the stellar orbit is prograde or retrograde (considering also that a fraction of young stars found in the GC are orbiting clockwise and others counter-clockwise, and that there is a warped disk). In addition, depending on the inclination, Liptai et al. (2019) find that simulations show the peak mass fallback rates are higher by ~ 1 order of magnitude in early stages and discs are formed ~ 1 orbital period earlier.

The next step in characterising TDEs which could occur in similar galactic environments as our GC is to study TDEs with different orbital parameters β and e (as found in the GC) including realistic stellar models of different types of stars found in such environments and relativistic effects due to a spinning MBH. Such study could provide better insight not only on the MBH responsible for the disruption, but also on the type of disrupted star, thus allowing us to learn more about the innermost stellar populations of far galaxies, otherwise difficult to observe directly.

Bibliography

Abbott, B. P., Abbott, R., Abbott, T. D., et al. 2016, , 116, 241102

Abbott, B. P., Abbott, R., Abbott, T. D., et al. 2017, , 118, 221101

Abbott, D. C. & Conti, P. S. 1987, , 25, 113

Alexander, K. D., Berger, E., Guillochon, J., Zauderer, B. A., & Williams, P. K. G. 2016, , 819, L25

Alexander, T. 2005, , 419, 65

Antonini, F., Lombardi, James C., J., & Merritt, D. 2011, , 731, 128

Arcavi, I., Gal-Yam, A., Sullivan, M., et al. 2014, , 793, 38

Auchettl, K., Guillochon, J., & Ramirez-Ruiz, E. 2017, , 838, 149

Ayal, S., Livio, M., & Piran, T. 2000, , 545, 772

Bade, N., Komossa, S., & Dahlem, M. 1996, , 309, L35

Baganoff, F. K., Maeda, Y., Morris, M., et al. 2003, , 591, 891

Balick, B. & Brown, R. L. 1974, , 194, 265

Bardeen, J. M. 1970, , 226, 64

Barnes, J. & Hut, P. 1986, , 324, 446

Barth, A. J., Ho, L. C., Rutledge, R. E., & Sargent, W. L. W. 2004, , 607, 90

Bartko, H., Martins, F., Trippe, S., et al. 2010, , 708, 834

Baumgardt, H., Hopman, C., Portegies Zwart, S., & Makino, J. 2006, , 372, 467

Becklin, E. E. & Neugebauer, G. 1968, , 151, 145

Begelman, M. C., Blandford, R. D., & Rees, M. J. 1980, , 287, 307

Benz, W. 1990, in Numerical Modelling of Nonlinear Stellar Pulsations Problems and Prospects, ed. J. R. Buchler, 269

Berti, E. & Volonteri, M. 2008, , 684, 822

Blagorodnova, N., Cenko, S. B., Kulkarni, S. R., et al. 2019, , 873, 92

Blagorodnova, N., Gezari, S., Hung, T., et al. 2017, , 844, 46

Bloom, J. S., Giannios, D., Metzger, B. D., et al. 2011, Science, 333, 203

Bogdanović, T., Cheng, R. M., & Amaro-Seoane, P. 2014, , 788, 99

Bolton, C. T. 1972, , 235, 271

Bonnerot, C. & Lu, W. 2019, arXiv e-prints, arXiv:1906.05865

Bonnerot, C., Rossi, E. M., & Lodato, G. 2017, , 464, 2816

Bonnerot, C., Rossi, E. M., Lodato, G., & Price, D. J. 2016, , 455, 2253

Bowyer, S., Byram, E. T., Chubb, T. A., & Friedman, H. 1965, Science, 147, 394

Brandt, W. N., Pounds, K. A., & Fink, H. 1995, , 273, L47

Brassart, M. & Luminet, J. P. 2008, , 481, 259

Broderick, A. E., Loeb, A., & Narayan, R. 2009, , 701, 1357

Broderick, J. W. & Fender, R. P. 2011, , 417, 184

Brown, G. C., Levan, A. J., Stanway, E. R., et al. 2015a, , 452, 4297

Brown, G. C., Levan, A. J., Stanway, E. R., et al. 2015b, , 452, 4297

Brown, R. L. 1982, , 262, 110

Brown, W. R. 2015, , 53, 15

Burrows, D. N., Kennea, J. A., Ghisellini, G., et al. 2011, , 476, 421

Camenzind, M. 2007, Compact objects in astrophysics : white dwarfs, neutron stars, and black holes

Cannizzo, J. K., Lee, H. M., & Goodman, J. 1990, , 351, 38

Carter, B. & Luminet, J. P. 1982, , 296, 211

Carter, B. & Luminet, J. P. 1983, , 121, 97

Carter, B. & Luminet, J. P. 1985, , 212, 23

Cenko, S. B., Cucchiara, A., Roth, N., et al. 2016, , 818, L32

Cenko, S. B., Krimm, H. A., Horesh, A., et al. 2012, , 753, 77

Chakrabarti, S. & Titarchuk, L. G. 1995, , 455, 623

Chandrasekhar, S. 1931, , 74, 81

Chang, P., Murray-Clay, R., Chiang, E., & Quataert, E. 2007, , 668, 236

Chen, J.-H. & Shen, R.-F. 2018, , 867, 20

Chen, X., Liu, F. K., & Magorrian, J. 2008, , 676, 54

Chen, X., Madau, P., Sesana, A., & Liu, F. K. 2009, , 697, L149

Cheng, R. M. & Bogdanović, T. 2014, , 90, 064020

Chornock, R., Berger, E., Gezari, S., et al. 2014, , 780, 44

Christopher, M. H., Scoville, N. Z., Stolovy, S. R., & Yun, M. S. 2005, , 622, 346

Coughlin, E. R., Armitage, P. J., Nixon, C., & Begelman, M. C. 2017, , 465, 3840

Coughlin, E. R. & Nixon, C. 2015, , 808, L11

Coughlin, E. R., Nixon, C., Begelman, M. C., & Armitage, P. J. 2016a, , 459, 3089

Coughlin, E. R., Nixon, C., Begelman, M. C., Armitage, P. J., & Price, D. J. 2016b, , 455, 3612

Curd, B. & Narayan, R. 2019, , 483, 565

Dai, L., Escala, A., & Coppi, P. 2013, , 775, L9

Dai, L., McKinney, J. C., Roth, N., Ramirez-Ruiz, E., & Miller, M. C. 2018, , 859, L20

Darbha, S., Coughlin, E. R., Kasen, D., & Nixon, C. 2019, , 488, 5267

Diehl, S., Rockefeller, G., Fryer, C. L., Riethmiller, D., & Statler, T. S. 2015, , 32, e048

Doeleman, S., Agol, E., Backer, D., et al. 2009, in astro2010: The Astronomy and Astrophysics Decadal Survey, Vol. 2010, 68

Donato, D., Cenko, S. B., Covino, S., et al. 2014, , 781, 59

Donley, J. L., Brandt, W. N., Eracleous, M., & Boller, T. 2002, , 124, 1308

Eckart, A. & Genzel, R. 1996, , 383, 415

Eckart, A. & Genzel, R. 1997, , 284, 576

Eckart, C. 1960, Physics of Fluids, 3, 421

Einstein, A. 1915a, Sitzungsberichte der Königlich Preußischen Akademie der Wissenschaften (Berlin, 831

Einstein, A. 1915b, Sitzungsberichte der Königlich Preußischen Akademie der Wissenschaften (Berlin, 844

Einstein, A. 1915c, Sitzungsberichte der Königlich Preußischen Akademie der Wissenschaften (Berlin, 315

Einstein, A. 1915d, Sitzungsberichte der Königlich Preußischen Akademie der Wissenschaften (Berlin, 778

Einstein, A. 1915e, Sitzungsberichte der Königlich Preußischen Akademie der Wissenschaften (Berlin, 799

Einstein, A. 1916, Annalen der Physik, 354, 769

Eisenhauer, F., Genzel, R., Alexander, T., et al. 2005, , 628, 246

Ekers, R. D., van Gorkom, J. H., Schwarz, U. J., & Goss, W. M. 1983, , 122, 143

Englmaier, P. & Shlosman, I. 2004, , 617, L115

Esquej, P., Saxton, R. D., Freyberg, M. J., et al. 2007, , 462, L49

Esquej, P., Saxton, R. D., Komossa, S., et al. 2008, , 489, 543

Evans, C. R. & Kochanek, C. S. 1989, , 346, L13

Event Horizon Telescope Collaboration, Akiyama, K., Alberdi, A., et al. 2019, , 875, L1

Farrar, G. R. & Gruzinov, A. 2009, , 693, 329

Ferrarese, L. & Ford, H. 2005, , 116, 523

Ferrarese, L. & Merritt, D. 2000, , 539, L9

Finkelstein, D. 1958, Physical Review, 110, 965

Fragione, G., Leigh, N. W. C., Ginsburg, I., & Kocsis, B. 2018, , 867, 119

Franchini, A., Lodato, G., & Facchini, S. 2016, , 455, 1946

Frank, J. 1978, , 184, 87

Frank, J. 1979, , 187, 883

French, K. D., Arcavi, I., & Zabludoff, A. 2016, , 818, L21

Fryer, C. L., Hungerford, A. L., & Rockefeller, G. 2007, International Journal of Modern Physics D, 16, 941

Gafton, E. & Rosswog, S. 2011, , 418, 770

Gafton, E. & Rosswog, S. 2019, , 487, 4790

Gebhardt, K., Bender, R., Bower, G., et al. 2000a, , 539, L13

Gebhardt, K., Kormendy, J., Ho, L. C., et al. 2000b, , 543, L5

Genzel, R., Eckart, A., Ott, T., & Eisenhauer, F. 1997, , 291, 219

Genzel, R., Eisenhauer, F., & Gillessen, S. 2010, Reviews of Modern Physics, 82, 3121

Genzel, R., Schödel, R., Ott, T., et al. 2003, , 594, 812

Gezari, S. 2014, Physics Today, 67, 37

Gezari, S., Basa, S., Martin, D. C., et al. 2008, , 676, 944

Gezari, S., Chornock, R., Lawrence, A., et al. 2015, , 815, L5

Gezari, S., Chornock, R., Rest, A., et al. 2012, , 485, 217

Gezari, S., Heckman, T., Cenko, S. B., et al. 2009, , 698, 1367

Gezari, S., Martin, D. C., Milliard, B., et al. 2006, , 653, L25

Ghez, A. M., Duchêne, G., Matthews, K., et al. 2003, , 586, L127

Ghez, A. M., Klein, B. L., Morris, M., & Becklin, E. E. 1998, , 509, 678

Giddings, S. B. 2017, Nature Astronomy, 1, 0067

Gillessen, S., Eisenhauer, F., Trippe, S., et al. 2009, , 692, 1075

Gingold, R. A. & Monaghan, J. J. 1977, , 181, 375

Golightly, E. C. A., Coughlin, E. R., & Nixon, C. J. 2019a, , 872, 163

Golightly, E. C. A., Nixon, C. J., & Coughlin, E. R. 2019b, , 882, L26

Gomboc, A. & Čadež, A. 2005, , 625, 278

Gomez, S., Nicholl, M., Short, P., et al. 2020, , 497, 1925

Gopal-Krishna, Mangalam, A., & Wiita, P. J. 2008, , 680, L13

Graham, A. W. 2008, , 680, 143

Graham, A. W. & Driver, S. P. 2005, , 22, 118

Graham, A. W. & Driver, S. P. 2007, , 655, 77

Graham, A. W., Erwin, P., Caon, N., & Trujillo, I. 2001, , 563, L11

Graur, O., French, K. D., Zahid, H. J., et al. 2018, , 853, 39

Greene, J. E., Strader, J., & Ho, L. C. 2019, arXiv e-prints, arXiv:1911.09678

Grupe, D., Beuermann, K., Mannheim, K., et al. 1995, , 299, L5

Guillochon, J., Manukian, H., & Ramirez-Ruiz, E. 2014, , 783, 23

Guillochon, J. & Ramirez-Ruiz, E. 2013, , 767, 25

Guillochon, J. & Ramirez-Ruiz, E. 2015, , 809, 166

Guillochon, J., Ramirez-Ruiz, E., Rosswog, S., & Kasen, D. 2009, , 705, 844

Gullieuszik, M., Greggio, L., Falomo, R., Schreiber, L., & Uslenghi, M. 2014, ,
    568, A89

Gültekin, K., Richstone, D. O., Gebhardt, K., et al. 2009, , 698, 198

Habibi, M., Gillessen, S., Martins, F., et al. 2017, , 847, 120

Halpern, J. P., Gezari, S., & Komossa, S. 2004, , 604, 572

Hamers, A. S. & Perets, H. B. 2017, , 846, 123

Hansen, C. J., Kawaler, S. D., & Trimble, V. 2004, Stellar interiors : physical principles, structure, and evolution

Hawking, S. W. 1976, , 14, 2460

Hayasaki, K., Stone, N., & Loeb, A. 2013, , 434, 909

Hayasaki, K., Stone, N., & Loeb, A. 2016, , 461, 3760

Herant, M. 1994, , 65, 1013

Hernquist, L. & Katz, N. 1989, , 70, 419

Hills, J. G. 1975, , 254, 295

Hills, J. G. 1988, , 331, 687

Hirt, C. W., Amsden, A. A., & Cook, J. L. 1974, Journal of Computational Physics, 14, 227

Holoien, T. W. S., Huber, M. E., Shappee, B. J., et al. 2019, , 880, 120

Holoien, T. W. S., Kochanek, C. S., Prieto, J. L., et al. 2016a, , 463, 3813

Holoien, T. W. S., Kochanek, C. S., Prieto, J. L., et al. 2016b, , 455, 2918

Holoien, T. W. S., Prieto, J. L., Bersier, D., et al. 2014, , 445, 3263

Hopkins, P. F., Hernquist, L., Cox, T. J., et al. 2006, , 163, 1

Hu, J. 2008, , 386, 2242

Ivanov, P. B. & Chernyakova, M. A. 2006, , 448, 843

Ivanov, P. B. & Novikov, I. D. 2001, , 549, 467

Ivanov, P. B., Polnarev, A. G., & Saha, P. 2005, , 358, 1361

Jansky, K. G. 1933, , 132, 66

Karas, V. & Šubr, L. 2007, , 470, 11

Kauffmann, G. & Haehnelt, M. 2000, , 311, 576

Kerr, R. P. 1963, , 11, 237

Kesden, M. 2012a, , 86, 064026

Kesden, M. 2012b, , 85, 024037

Khabibullin, I. & Sazonov, S. 2014, , 444, 1041

Kobayashi, S., Laguna, P., Phinney, E. S., & Mészáros, P. 2004, , 615, 855

Kochanek, C. S. 1994, , 422, 508

Kocsis, B. & Tremaine, S. 2011, , 412, 187

Komossa, S. 2015, Journal of High Energy Astrophysics, 7, 148

Komossa, S. & Bade, N. 1999, Astronomical Society of the Pacific Conference Series, Vol. 161, The Giant X-ray Outburst in NGC 5905 - a Tidal Disruption Event?, ed. J. Poutanen & R. Svensson, 234

Komossa, S. & Greiner, J. 1999, , 349, L45

Komossa, S., Zhou, H., Rau, A., et al. 2009, , 701, 105

Komossa, S., Zhou, H., Wang, T., et al. 2008, , 678, L13

Kormendy, J. & Ho, L. C. 2013, , 51, 511

Kormendy, J. & Richstone, D. 1995, , 33, 581

Kosovichev, A. G. & Novikov, I. D. 1992, , 258, 715

Kozai, Y. 1962, , 67, 591

Krabbe, A., Genzel, R., Drapatz, S., & Rotaciuc, V. 1991, , 382, L19

Krabbe, A., Genzel, R., Eckart, A., et al. 1995, , 447, L95

Krolik, J., Piran, T., Svirski, G., & Cheng, R. M. 2016, , 827, 127

Krolik, J. H. & Piran, T. 2011, , 743, 134

Krolik, J. H. & Piran, T. 2012, , 749, 92

Lacy, J. H. 1980, Highlights of Astronomy, 5, 163

Lacy, J. H., Townes, C. H., & Hollenbach, D. J. 1982, , 262, 120

Laguna, P., Miller, W. A., Zurek, W. H., & Davies, M. B. 1993, , 410, L83

Laine, S., Knapen, J. H., Perez-Ramirez, D., Doyon, R., & Nadeau, D. 1999, , 302, L33

Latif, M. A. & Ferrara, A. 2016, , 33, e051

Law-Smith, J., Guillochon, J., & Ramirez-Ruiz, E. 2019, , 882, L25

Law-Smith, J. A. P., Coulter, D. A., Guillochon, J., Mockler, B., & Ramirez-Ruiz, E. 2020, arXiv e-prints, arXiv:2007.10996

LeBlanc, F. 2010, An Introduction to Stellar Astrophysics

Leloudas, G., Fraser, M., Stone, N. C., et al. 2016, Nature Astronomy, 1, 0002

Levan, A. J., Tanvir, N. R., Cenko, S. B., et al. 2011, Science, 333, 199

Lidov, M. L. 1962, , 9, 719

Liptai, D., Price, D. J., Mandel, I., & Lodato, G. 2019, arXiv e-prints, arXiv:1910.10154

Liu, G. R., Liu, M. B., & Li, S. 2004, Computational Mechanics, 33, 491

Lockhart, K. E., Lu, J. R., Peiris, H. V., et al. 2018, , 854, 121

Lodato, G., Cheng, R. M., Bonnerot, C., & Dai, J. L. 2020, , 216, 63

Lodato, G., Franchini, A., Bonnerot, C., & Rossi, E. M. 2015, Journal of High Energy Astrophysics, 7, 158

Lodato, G., King, A. R., & Pringle, J. E. 2009, , 392, 332

Lodato, G. & Natarajan, P. 2006, , 371, 1813

Lodato, G. & Natarajan, P. 2007, , 377, L64

Lodato, G. & Rossi, E. M. 2011, , 410, 359

Loeb, A. & Ulmer, A. 1997, , 489, 573

Lu, J. R., Ghez, A. M., Hornstein, S. D., et al. 2009, , 690, 1463

Lu, W., Kumar, P., & Narayan, R. 2017, , 468, 910

Lucy, L. B. 1977, , 82, 1013

Luminet, J. P. & Barbuy, B. 1990, , 99, 838

Luminet, J. P. & Carter, B. 1986, , 61, 219

Luminet, J. P. & Marck, J. A. 1985, , 212, 57

Lynden-Bell, D. 1969, , 223, 690

Lynden-Bell, D. & Rees, M. J. 1971, , 152, 461

Mageshwaran, T. & Bhattacharyya, S. 2020, , 496, 1784

Magorrian, J. & Tremaine, S. 1999, , 309, 447

Magorrian, J., Tremaine, S., Richstone, D., et al. 1998, , 115, 2285

McConnell, N. J., Ma, C.-P., Gebhardt, K., et al. 2011, , 480, 215

Mehrgan, K., Thomas, J., Saglia, R., et al. 2019, , 887, 195

Merloni, A., Heinz, S., & di Matteo, T. 2003, , 345, 1057

Merritt, D. 2013, Classical and Quantum Gravity, 30, 244005

Merritt, D., Alexander, T., Mikkola, S., & Will, C. M. 2011, , 84, 044024

Merritt, D. & Ferrarese, L. 2001, , 547, 140

Merritt, D. & Poon, M. Y. 2004, , 606, 788

Metzger, B. D., Giannios, D., & Mimica, P. 2012, , 420, 3528

Mezcua, M., Hlavacek-Larrondo, J., Lucey, J. R., et al. 2018, , 474, 1342

Miller, J. M., Kaastra, J. S., Miller, M. C., et al. 2015, , 526, 542

Misner, C. W., Thorne, K. S., & Wheeler, J. A. 1973, Gravitation

Miyoshi, M., Moran, J., Herrnstein, J., et al. 1995, , 373, 127

Monaghan, J. J. 1992, , 30, 543

Monaghan, J. J. 2005, Reports on Progress in Physics, 68, 1703

Montgomery, C., Orchiston, W., & Whittingham, I. 2009, Journal of Astronomical History and Heritage, 12, 90

Morris, J. P. 1996, , 13, 97

Mummery, A. & Balbus, S. A. 2020, , 497, L13

Murchikova, E. M., Phinney, E. S., Pancoast, A., & Blandford, R. D. 2019, , 570, 83

Najarro, F., Krabbe, A., Genzel, R., et al. 1997, , 325, 700

Nayakshin, S., Cuadra, J., & Springel, V. 2007, , 379, 21

Noh, W. F. 1963

Nolthenius, R. A. & Katz, J. I. 1982, , 263, 377

Norman, C. & Silk, J. 1983, , 266, 502

Nowak, M. A. & Wagoner, R. V. 1991, , 378, 656

Oh, S., Kim, S. S., & Figer, D. F. 2009, Journal of Korean Astronomical Society, 42, 17

Oppenheimer, J. R. & Volkoff, G. M. 1939, Physical Review, 55, 374

Paczyński, B. & Wiita, P. J. 1980, , 500, 203

Palaversa, L., Gezari, S., Sesar, B., et al. 2016, , 819, 151

Parsa, M., Eckart, A., Shahzamanian, B., et al. 2017, , 845, 22

Paumard, T., Genzel, R., Martins, F., et al. 2006, , 643, 1011

Paxton, B., Bildsten, L., Dotter, A., et al. 2010, MESA: Modules for Experiments in Stellar Astrophysics

Perets, H. B., Hopman, C., & Alexander, T. 2007, , 656, 709

Pfalzner, S. & Gibbon, P. 1996, Many-Body Tree Methods in Physics

Phinney, E. S. 1989, in IAU Symposium, Vol. 136, The Center of the Galaxy, ed. M. Morris, 543

Piran, T., Svirski, G., Krolik, J., Cheng, R. M., & Shiokawa, H. 2015, , 806, 164

Plotkin, R. M., Markoff, S., Kelly, B. C., Körding, E., & Anderson, S. F. 2012, , 419, 267

Pogge, R. W. & Martini, P. 2002, , 569, 624

Polnarev, A. G. & Rees, M. J. 1994, , 283, 301

Poon, M. Y. & Merritt, D. 2004, , 606, 774

Price, D. J. 2007, , 24, 159

Price, D. J. 2012, Journal of Computational Physics, 231, 759

Price, D. J., Wurster, J., Tricco, T. S., et al. 2018, , 35, e031

Quataert, E. 2004, , 613, 322

Ramirez-Ruiz, E. & Rosswog, S. 2009, , 697, L77

Rauch, K. P. & Ingalls, B. 1998, , 299, 1231

Rauch, K. P. & Tremaine, S. 1996, , 1, 149

Rees, M. J. 1988, , 333, 523

Regan, M. W. & Mulchaey, J. S. 1999, , 117, 2676

Reis, R. C., Miller, J. M., Reynolds, M. T., et al. 2012, Science, 337, 949

Remillard, R. A. & McClintock, J. E. 2006, , 44, 49

Rieke, G. H., Rieke, M. J., & Paul, A. E. 1989, , 336, 752

Rossi, E. M., Stone, N. C., Law-Smith, J. A. P., et al. 2020, arXiv e-prints, arXiv:2005.12528

Rosswog, S. 2009, , 53, 78

Rosswog, S. & Price, D. 2007, , 379, 915

Rosswog, S., Ramirez-Ruiz, E., & Hix, W. R. 2009a, , 695, 404

Rosswog, S., Ramirez-Ruiz, E., & Hix, W. R. 2009b, in Journal of Physics Conference Series, Vol. 172, Journal of Physics Conference Series, 012036

Sacchi, A. & Lodato, G. 2019, , 486, 1833

Sacchi, A., Lodato, G., Toci, C., & Motta, V. 2020, , 495, 1227

Sakurai, Y., Yoshida, N., & Fujii, M. S. 2019, , 484, 4665

Salpeter, E. E. 1964, , 140, 796

Sargent, W. L. W., Young, P. J., Boksenberg, A., et al. 1978, , 221, 731

Sari, R., Kobayashi, S., & Rossi, E. M. 2010, , 708, 605

Saxton, R. D., Read, A. M., Esquej, P., et al. 2012, , 541, A106

Saxton, R. D., Read, A. M., Komossa, S., et al. 2014, , 572, A1

Schmidt, M. 1963, , 197, 1040

Schnittman, J. D. 2010, , 724, 39

Schödel, R., Eckart, A., Mužić, K., et al. 2007, , 462, L1

Schwarzschild, K. 1916, Sitzungsberichte der Königlich Preußischen Akademie der Wissenschaften (Berlin, 189

Schwarzschild, K. 1999, arXiv e-prints, physics/9905030

Seigar, M. S., Kennefick, D., Kennefick, J., & Lacy, C. H. S. 2008, , 678, L93

Sérsic, J. L. 1963, Boletin de la Asociacion Argentina de Astronomia La Plata Argentina, 6, 41

Sesana, A. 2012, Advances in Astronomy, 2012, 805402

Seth, A. C., Dalcanton, J. J., Hodge, P. W., & Debattista, V. P. 2006, , 132, 2539

Shakura, N. I. & Sunyaev, R. A. 1973, , 500, 33

Shao, L., Zhang, F.-W., Fan, Y.-Z., & Wei, D.-M. 2011, , 734, L33

Shapiro, S. L., Teukolsky, S. A., Smorodinskij, Y. A., Dolgov, A. D., & Rodionov, S. N. 1985, Black holes, white dwarfs and neutron stars. The physics of compact objects.

Shen, R.-F. & Matzner, C. D. 2014, , 784, 87

Shiokawa, H., Krolik, J. H., Cheng, R. M., Piran, T., & Noble, S. C. 2015, , 804, 85

Shlosman, I., Frank, J., & Begelman, M. C. 1989, , 338, 45

Sponholz, H. 1994, , 65, 1135

Springel, V. 2005, , 364, 1105

Springel, V. 2010, , 48, 391

Stone, N. 2013, PhD thesis, Harvard University

Stone, N. & Loeb, A. 2011, in American Astronomical Society Meeting Abstracts, Vol. 218, American Astronomical Society Meeting Abstracts #218, 235.04

Stone, N., Sari, R., & Loeb, A. 2013, , 435, 1809

Stone, N. C., Kesden, M., Cheng, R. M., & van Velzen, S. 2019, General Relativity and Gravitation, 51, 30

Stone, N. C. & Metzger, B. D. 2016, , 455, 859

Stone, N. C. & van Velzen, S. 2016, , 825, L14

Strubbe, L. E. & Murray, N. 2015, , 454, 2321

Strubbe, L. E. & Quataert, E. 2009, , 400, 2070

Svirski, G., Piran, T., & Krolik, J. 2017, , 467, 1426

Tananbaum, H., Gursky, H., Kellogg, E., Giacconi, R., & Jones, C. 1972, , 177, L5

Tanikawa, A. 2018, , 475, L67

Tanikawa, A., Sato, Y., Nomoto, K., et al. 2017, , 839, 81

Tejeda, E., Gafton, E., Rosswog, S., & Miller, J. C. 2017, , 469, 4483

Tejeda, E. & Rosswog, S. 2013, , 433, 1930

Thorne, K. S. 1974, , 191, 507

Tolman, R. C. 1939, Physical Review, 55, 364

Toscani, M., Lodato, G., & Nealon, R. 2019, , 489, 699

Trani, A. A., Mapelli, M., & Ballone, A. 2018, , 864, 17

Tremaine, S., Gebhardt, K., Bender, R., et al. 2002, , 574, 740

van Velzen, S., Anderson, G. E., Stone, N. C., et al. 2016, Science, 351, 62

van Velzen, S., Farrar, G. R., Gezari, S., et al. 2011, , 741, 73

van Velzen, S., Gezari, S., Hammerstein, E., et al. 2020, arXiv e-prints, arXiv:2001.01409

Vasiliev, E. 2014, Classical and Quantum Gravity, 31, 244002

Vasiliev, E. & Merritt, D. 2013, , 774, 87

Verlet, L. 1967, Phys. Rev., 159, 98

Volonteri, M. 2010a, , 466, 1049

Volonteri, M. 2010b, , 18, 279

Volonteri, M. & Bellovary, J. 2012, Reports on Progress in Physics, 75, 124901

Volonteri, M., Haardt, F., & Madau, P. 2003, , 582, 559

Volonteri, M., Lodato, G., & Natarajan, P. 2008, , 383, 1079

Volonteri, M. & Natarajan, P. 2009, , 400, 1911

Volonteri, M. & Rees, M. J. 2005, , 633, 624

Štolc, M. & Karas, V. 2019, Astronomische Nachrichten, 340, 570

Wang, J. & Merritt, D. 2004, , 600, 149

Wang, T.-G., Zhou, H.-Y., Komossa, S., et al. 2012, , 749, 115

Wang, T.-G., Zhou, H.-Y., Wang, L.-F., Lu, H.-L., & Xu, D. 2011, , 740, 85

Wardle, M. & Yusef-Zadeh, F. 2008, , 683, L37

Webster, B. L. & Murdin, P. 1972, , 235, 37

Wolfe, A. M. & Burbidge, G. R. 1970, , 161, 419

Woo, J.-H., Cho, H., Gallo, E., et al. 2019, Nature Astronomy, 3, 755

Yang, J., Wang, F., Fan, X., et al. 2020, , 897, L14

Young, P. J., Westphal, J. A., Kristian, J., Wilson, C. P., & Landauer, F. P. 1978, , 221, 721

Yu, Q. & Tremaine, S. 2003, , 599, 1129

Yusef-Zadeh, F., Braatz, J., Wardle, M., & Roberts, D. 2008, , 683, L147

Yusef-Zadeh, F., Melia, F., & Wardle, M. 2000, Science, 287, 85

Yusef-Zadeh, F., Roberts, D. A., & Biretta, J. 1998, , 499, L159

Yusef-Zadeh, F. & Wardle, M. 2012, in Journal of Physics Conference Series, Vol. 372, Journal of Physics Conference Series, 012024

Zajacek, M. & Tursunov, A. 2019, The Observatory, 139, 231

Zauderer, B. A., Berger, E., Margutti, R., et al. 2013, , 767, 152

Zauderer, B. A., Berger, E., Soderberg, A. M., et al. 2011, , 476, 425

Zel'dovich, Y. B. 1964, Soviet Physics Doklady, 9, 195